

# The Microstrip Gas Counter and its application in the ATLAS inner tracker

Thesis (WWW version)

Jurriaan Schmitz

August 31, 1994

Promotores: Prof. Dr. J. J. Engelen  
                  Prof. Dr. C. Daum  
Co-promotor: Dr. K. Bos

Faculteit der Natuur- en Sterrenkunde

The work described in this thesis is part of the research programme of 'het Nationaal Instituut voor Kernfysica en Hoge-Energie Fysica (NIKHEF-H)' in Amsterdam, the Netherlands. The author was financially supported by 'de Stichting voor Fundamenteel Onderzoek der Materie (FOM)'.

# Contents

<b>1</b>	<b>The Large Hadron Collider</b>	<b>1</b>
1.1	Particle accelerators and detectors	1
1.2	The Standard Model	2
1.2.1	Particles and interactions	2
1.2.2	The standard theory of interactions	4
1.2.3	Higgs searches	4
1.3	The Large Hadron Collider	5
1.3.1	The choice of beam particles	5
1.3.2	The physics potential of the LHC	7
1.3.3	The experiments	10
1.3.4	Research	11
<b>2</b>	<b>Description of the Microstrip Gas Counter</b>	<b>15</b>
2.1	Introduction: the multiwire proportional chamber	15
2.2	The invention of the MSGC	16
2.3	Charged particle detection with the MSGC	18
2.3.1	Introduction	18
2.3.2	Ionisation of a gas	18
2.3.3	Drift and diffusion of electrons and ions	20
2.3.4	Gas amplification	22
2.3.5	Signal development	24
2.4	Photon detection with the MSGC	25
2.5	Aspects of the electric field	26
<b>3</b>	<b>R&amp;D of the Microstrip Gas Counter</b>	<b>27</b>
3.1	Introduction	27
3.2	Radiation hardness	28
3.3	High flux performance and switch-on behaviour	29
3.4	Micro-discharges	30
3.5	Energy and position resolution and efficiency	30
3.6	Second coordinate readout	30
3.7	Variations of the geometry	31
3.8	Readout	32
3.9	Detector optimisation for high-flux experiments	33
3.9.1	Geometry limitations	33
3.9.2	Gas mixtures for the MSGC	34

3.9.3	Reprint: tests of the performance of different gas mixtures in microstrip gas counters . . . . .	35
<b>4</b>	<b>Monte Carlo simulations of the MSGC performance</b>	<b>45</b>
4.1	Monte Carlo simulations . . . . .	45
4.2	Simulation of the MSGC . . . . .	46
4.2.1	Introduction . . . . .	46
4.2.2	Description of the MSGC model . . . . .	46
4.2.3	Tuning the Monte Carlo to experimental data . . . . .	48
4.3	The position resolution of the MSGC . . . . .	51
4.3.1	Determination of the position of a track . . . . .	51
4.3.2	Contributions to the measurement error of the position . . . . .	52
4.3.3	Optimisation of the MSGC resolution . . . . .	55
4.4	Reprint: study of inclined particle tracks in micro strip gas counters . . . . .	56
4.5	Reprint: simulation of front end preamplifiers for the MSGC . . . . .	66
<b>5</b>	<b>The ATLAS inner detector</b>	<b>75</b>
5.1	Introduction . . . . .	75
5.2	The ATLAS experiment . . . . .	76
5.3	Layout of the ATLAS inner detector . . . . .	78
5.3.1	Aims . . . . .	78
5.3.2	Design considerations . . . . .	79
5.3.3	Electron identification . . . . .	81
5.3.4	Available detector technologies . . . . .	83
5.3.5	The Cosener's House layout . . . . .	85
5.4	Performance estimates . . . . .	88
<b>6</b>	<b>Higgs decay into 4 leptons in the ATLAS detector</b>	<b>91</b>
6.1	Introduction . . . . .	91
6.2	Higgs physics . . . . .	92
6.2.1	Creation and decay of a Higgs boson . . . . .	92
6.2.2	Event rate and topology of the $H \rightarrow ZZ^* \rightarrow \ell^+ \ell^- \ell^+ \ell^-$ decay . . . . .	94
6.2.3	Background to the $H \rightarrow \ell^+ \ell^- \ell^+ \ell^-$ decay . . . . .	96
6.3	The observability of $H \rightarrow \ell^+ \ell^- \ell^+ \ell^-$ . . . . .	97
6.3.1	Introduction . . . . .	97
6.3.2	Tracking efficiency . . . . .	97
6.3.3	Lepton isolation . . . . .	99
6.3.4	Direction and momentum measurement . . . . .	99
6.4	The role of the MSGC tracker for $H \rightarrow ZZ^* \rightarrow \ell^+ \ell^- \ell^+ \ell^-$ . . . . .	102
	<b>Acknowledgements</b>	<b>103</b>
	<b>Summary</b>	<b>105</b>
	<b>Samenvatting</b>	<b>107</b>
	<b>References</b>	<b>109</b>

*Our task is not to penetrate into the essence of things, the meaning of which we don't know anyway, but rather to develop concepts which allow us to talk in a productive way about phenomena in nature.*

Niels Bohr

# Chapter 1

## The Large Hadron Collider

### 1.1 Particle accelerators and detectors

High energy physics is the scientific discipline that covers the study of the tiniest building blocks of matter. In the nineteenth century, it was discovered that matter is built up from atoms, the smallest constituents that carry the chemical properties of an element. In the beginning of this century several experiments indicated that these atoms are compositions of charged sub-particles, the positive nuclei and negative electrons. Later experiments showed that nuclei could again be taken apart. High energy physicists study subatomic particles, focusing on the measurement of their fundamental properties (mass, charge, etc.), the interaction between these particles and their classification.

To look into a nucleus of an atom, we need a microscope: an object should be irradiated with some particles (light, for instance) and the pattern of the outcoming particles tells us what is inside the object of study. The level of detail that we can observe in this way is determined by the wavelength of the incoming particles: with blue light, one can see smaller details in a sample than with red light because blue light has a shorter wavelength. The energy of a probe particle is inversely proportional to its wavelength, so the more detail we want to see, the higher the energy of the probes should be: hence the designation 'high energy physics'. It is found that light is a very good probe in the visible light range, but if we want to look into more detail different probes can be more useful, e.g. electrons in an electron microscope. Charged particle beams are the most frequently used in high energy physics. So instead of a simple lamp that provides the light for our 'microscopy', we use particle beams that are created in particle accelerators.

In normal microscopy the observation of the irradiated sample is done by eye. In the case of irradiation with particles of high energy this can better be done with instruments, because the radiation can be harmful and there is much more than only the visual information at hand. The detection of the particles with high energy emanating from of the sample, is done with dedicated particle detectors. With these detectors, we can measure the intensity of particles at a certain position, and measure the energy and position of each individual particle. The information from the detectors is passed on to the experimentalist, usually electronically.

This thesis discusses a new 'microscope' for high energy physics, the Large Hadron Collider (LHC). This machine will accelerate proton beams to the world record energy of 7 TeV per particle (so that the kinetic energy of the protons is 7,000 times their mass) and collide them head-on at a well-defined spot. The high energy of the colliding particles allows us not only to study the structure of matter to a tinier scale than ever, but also to create new, heavy particles that were never created before in a laboratory. To study the proton collisions in the Large Hadron Collider, there is a need for new particle detectors because the conventional detectors cannot cope with the large flux of particles generated in collisions at the LHC. A large part of this thesis is devoted to a candidate new detector: the Microstrip Gas Counter (MSGC).

In this first chapter, a motivation is given for the construction of the Large Hadron Collider, concentrating on the possible existence of a heavy particle called the Higgs boson. Chapter 2 to 4 are devoted to the operation principles of the Microstrip Gas Counter; the last chapters discuss the implementation of these detectors in a Large Hadron Collider experiment, and here we will address the question how the Higgs boson could be identified and studied.

## 1.2 The Standard Model

### 1.2.1 Particles and interactions

Many years of experimental high energy physics have lead to the belief that all matter is composed of particles that are smaller than  $10^{-15}$  cm. These particles are described in a quantum mechanical way and as they have spin 1/2 they follow Fermi-Dirac statistics<sup>1</sup>. For this reason they are called fermions. Two types of fermions are distinguished: the leptons, which are particles that may live freely in space (such as electrons), and the quarks, that are confined to participation in a group: quarks never occur singly, they always come in clusters. These clusters are called hadrons. A large amount of hadrons has been discovered, amongst which the most common particles are the proton, the neutron, and the kaons and pions. The set of leptons and quarks is shown in table 1.1. (These fermions are called 'elementary' since there is no evidence that these particles are composites.) The arrangement of these fermions in the table implicitly introduces a classification. The particles can be grouped into three families with four members each, two leptons and two quarks. The only difference between the families seems to be in the mass of the members: the muon ( $\mu$ ) is a heavy copy of the electron (e), and the  $\tau$  lepton is even heavier. The same goes for the quarks. Only for the neutrinos the situation may be different: no determination of the neutrino masses has been possible so far. One generally assumes that they are massless, for which there are many indications. Yet it is clearly observed that these three neutrinos are different. So roughly we can say that matter is composed of four fundamental particles: e,  $\nu_e$ , u and d, called the first family, and copies of these particles which may have a higher mass.

It was only recently discovered that there are probably only three of these 'families'. This was studied by counting the number of different light neutrinos at the Large Electron Positron

---

<sup>1</sup>Throughout this thesis, we use natural units:  $\hbar = c = 1$ .

lepton name	symbol	charge	mass	quark name	symbol	charge	mass
electron	$e$	$-e$	511 keV	up	$u$	$+\frac{2}{3}e$	
electron-neutrino	$\nu_e$	0	< 17 eV	down	$d$	$-\frac{1}{3}e$	
muon	$\mu$	$-e$	106 MeV	charm	$c$	$+\frac{2}{3}e$	
muon-neutrino	$\nu_\mu$	0	< 270 keV	strange	$s$	$-\frac{1}{3}e$	
tau	$\tau$	$-e$	1.78 GeV	top	$t$	$+\frac{2}{3}e$	$\sim 174$ GeV
tau-neutrino	$\nu_\tau$	0	< 35 MeV	bottom	$b$	$-\frac{1}{3}e$	$\sim 5$ GeV

Table 1.1: The known elementary fermions in Nature with some of their properties. The tau-neutrino is only observed indirectly so far; the direct observation of the top quark is very recent [1]. The mass of the light quarks (u,d,c,s) is not defined unambiguously [2]. Of all these particles, also anti-particles exist with the same mass but opposite charge.

collider LEP [3]. This number is 3, and if there are only three neutrinos, we assume that the same goes for the other fermions.

This set of 12 particles can be doubled if we consider the fact that each of these particles has its anti-particle. The antiparticle is usually denoted by a bar above its symbol:  $\bar{\nu}_e$ ,  $\bar{u}$ ,  $\bar{d}$  etc., except for the charged leptons where the distinction is made with the particle charge:  $e^-$  is the electron,  $e^+$  its antiparticle the positron. The question why Nature consists predominantly of particles and not anti-particles is still open although there are models that explain this imbalance in the framework of the Big Bang model.

The charged fermions in the second and third family are instable. (The neutrinos are usually assumed to be stable.) A heavy fermion will eventually decay into lighter fermions due to the weak interaction. This is why the first family of particles is very familiar to the physicist, but the other, instable particles were discovered only when the tools were developed to create these particles in a laboratory and observe their decay (often within a fraction of a second). (The only exception being the muon that was observed first in cosmic rays.)

These fermions are the building blocks of matter. Apart from the fermions, also their quantum mechanical counterparts exist: bosons, particles that follow Bose-Einstein statistics. The photon is the most common of these bosons. The other elementary bosons were only discovered with the use of accelerators. They are called  $W^+$ ,  $W^-$ ,  $Z^0$  and gluons. The known elementary bosons are listed in table 1.2. The bosons play a different role in our understanding of Nature than the fermions: they carry the force between interacting particles. The four forces of Nature each have their own bosons (as shown partly in the table): the electromagnetic force is carried by the photon, the weak nuclear force by the so-called 'intermediate vector bosons'  $W^+$ ,  $W^-$  and  $Z^0$ , and the strong nuclear force by the gluons. The gravitational force is assumed to be propagated by a hypothetical particle called the graviton, but this particle has never been observed. Gravity does not play a quantitative role in the interactions studied in high energy physics, so it is ignored in our models.

boson	mass	associated force
$\gamma$ (photon)	0	electromagnetic
$W^+, W^-$	80.2 GeV	weak
$Z^0$	91.2 GeV	weak
8 gluons	0	strong

Table 1.2: The known elementary bosons in Nature with some of their properties.

### 1.2.2 The standard theory of interactions

The electromagnetic interaction between the fermions is extremely well described by Quantum Electrodynamics, founded by Feynman, Schwinger and Tomonaga. This theory was later extended to include the description of weak interactions forming the electroweak theory, which is also well established. The strong interaction, acting only on quarks and gluons, is described by Quantum Chromodynamics. Although the confirmation of this theory is more difficult (especially at energies below  $\sim 300$  MeV) the theories of electroweak and strong interactions seem a good package to describe the elementary particles and their interactions.

Yet there are problems. *A priori*, in this theory all particles are massless. As stated before, most of them are not, so something must be missing in the description of the particle interactions. Secondly, the model predicts some anomalous cross sections at high energies (beyond 1 TeV). The cross section of the simple process  $W^+ + W^- \rightarrow W^+ + W^-$  increases as a function of the centre-of-mass energy of the two bosons; at a centre-of-mass energy larger than 1 TeV, the probability that two interacting W's produce two W's turns out to be larger than unity! A few solutions to this problem have been proposed. The most favoured of these solutions is to introduce a new boson, the so-called Higgs boson, that interferes with the  $W^+W^-$  scattering such that the calculation changes and produces a consistent result. The Higgs mechanism solves the anomalies at high energy in this way.

The introduction of the Higgs boson is not limited to the simple addition of a particle to the set of known particles. To end up with one Higgs boson, one has to introduce two new bosons and mix these with the carriers of the electroweak force. In this mixing, the W and Z bosons become massive while the photon remains massless (a process called electroweak symmetry breaking). The Higgs mechanism finds its charm in solving both the high energy problem and (at least part of) the mass problem. Therefore this mechanism is normally accepted as a necessary extension to the theories of electroweak and strong interactions. The electroweak theory together with the Higgs formalism is called the Standard Model of Electroweak Interactions, or briefly the Standard Model.

### 1.2.3 Higgs searches

The introduction of a Higgs boson in the world of elementary particles may solve problems with the theory, but does it match reality? Many experiments were used for the search of the Higgs boson, which should manifest itself as a resonance in particle collision cross sections.

The particle was never found, and this leads us to conclude that if it exists, it should be too heavy to be produced at the current particle accelerators. The actual lower limit set on the mass of the Higgs boson is now 63.5 GeV (at 95% confidence level)[4]. The theory itself gives an *upper* limit to the mass of the boson: for  $m_H \gg m_W$ , the width of the Higgs resonance is proportional to the Higgs mass to the third power, and we can readily assume that the particle is not a particle if the width is larger than the mass itself. This sets an upper limit at 1–2 TeV for the Higgs mass, depending on the details of the calculation of the resonance width [5]. Other arguments lead to an upper limit of only 500–800 GeV [6]. So if we can build a particle accelerator powerful enough to create particles with a mass up to 1 TeV plus an experimental arrangement that is able to identify these particles, we can in principle give a final word on the existence of this Higgs boson.

On the other hand, one cannot pretend to be sure about the existence of the Higgs boson. The theory without a Higgs extension breaks down around 1 TeV, and so this energy scale is favoured to find out which is the real solution to the problem of anomalous cross sections. So while the Large Hadron Collider can give a definitive answer to the question whether the Higgs boson exists, more generally speaking it is proposed for the study of elementary particles in the energy range of 1 TeV, in which the bare electroweak theory is unsatisfactory.

## 1.3 The Large Hadron Collider

### 1.3.1 The choice of beam particles

To probe the 1 TeV energy scale, we need particle collisions with equivalent collision energies. For this type of collisions we have to use charged long-living particles: charged because then electromagnetic acceleration can be used, and long-living because then there is enough time to accelerate the particles. This limits our possibilities to electrons, protons, and their antiparticles.

While the acceleration of the beam particles is always done with electromagnetic waves, two different types of colliders can be distinguished: linear and circular colliders. In linear colliders, two beams of particles are accelerated towards each other by a number of accelerating elements. After the crossing of the two beams, the particles are dumped. Modern techniques are not adequate to realise a linear collider for the TeV energy range, although new developments are promising [7].

In circular colliders, the beam is bent back to the accelerating elements to be re-used. The advantage of circular colliders is obviously the more efficient use of both the particle beam and the electromagnetic components. The main disadvantage is, that bending magnets are needed, and that the bending introduces radiation losses (synchrotron radiation). The average energy loss through synchrotron radiation per revolution in a circular accelerator is given by

$$-\Delta E = \frac{e^2 \beta^3}{3\epsilon_0 R} \left( \frac{E}{mc^2} \right)^4, \quad (1.1)$$

where  $E$  is the energy of beam particles with mass  $m$ , charge  $e$  and velocity  $\beta = v/c$ , and  $R$  is the radius of curvature of the accelerator. The factor  $m^{-4}$  determines that electrons suffer

much more from radiation loss than protons. The use of an electron-positron storage ring in the energy range of 1 TeV is out of the question for this reason. Even if we would build an enormous accelerator with 200 km circumference, a 500 GeV electron would lose more than 150 GeV per revolution.

Protons have much less synchrotron radiation loss, because their mass is much higher. Protons are therefore relatively easy to store and accelerate in a circular machine. The same goes for antiprotons. With protons, the art is in the bending. The minimum circumference of a circular machine is given by the magnetic field strength in the bending magnets, and if we want to probe the 1 TeV energy scale with colliding proton beams, the storage ring will have at least the size of the LEP collider (with a radius of curvature of 3.5 km). For this reason, the existing LEP-tunnel is well suited to host a future proton collider.

Protons, however, have the disadvantage of being composite objects. They consist of three valence quarks, plus a sea of gluons and quarks. When two protons are brought into collision at these energies, it is difficult to tell which of these constituents actually collided and which were merely spectators to the event. What is worse, the proton as a whole may have the exact energy up to which it is accelerated in the ring, but its constituents carry an *a priori* unknown fraction of this energy. The 'real' centre-of-mass energy in proton-proton collisions is lower than the sum of the energies of the protons. This adds to the complexity of the analysis of proton-proton collisions. By far, most of the collisions involve an effective energy much lower than the sum of the beam particle energies. Since we aim at the energy range of 1 TeV, we need beams of much higher energy than 1 TeV. Also we have to accept that for every interesting collision, there will be millions of soft collisions obscuring our measurements. The interaction rate must be enormous to have a few collisions with a large energy transfer.

This collision rate imposes another requirement on us: the beams must be very intense to achieve a high interaction rate. Unfortunately, this requirement forces us to use two proton beams. Only protons can be created in such large numbers as needed. This is unfortunate because it is much simpler to build a machine that collides a proton beam with an antiproton beam: then the same accelerating and bending units can be used for both beams. The two proton beams in the LHC machine will have separate beam pipes and are only brought together at the interaction points.

So to open up the TeV range the Large Hadron Collider will collide two proton beams of high intensity in the LEP tunnel. Some parameters of the collider are listed in table 1.3. Each proton beam consists of needle-shaped packets called bunches. These are focused onto each other in two interaction regions. In each of these, of the order of  $10^9$  interactions per second will take place. The luminosity  $\mathcal{L}$  describes the potential interaction rate of colliding beams: it can be defined as

$$\mathcal{L} = f \frac{N_1 N_2}{A}, \quad (1.2)$$

where  $N_1$  and  $N_2$  are the numbers of particles in each bunch,  $f$  is the bunch crossing frequency and  $A$  is the cross-sectional area of each particle bunch (assuming the two bunches overlap completely during the crossing) [9]. The luminosity relates the cross section of a certain process to its rate of occurrence  $R$ :  $R = \sigma \mathcal{L}$ . Note that the 25 ns bunch crossing interval and the  $10^9$  interactions per second imply that each bunch crossing will cause more than

one collision. Each interesting collision will be accompanied by about 25 collisions, that are generally soft hadronic collisions. When an LHC experiment registers collisions without any requirement (bias) on the type of collision, only this type of events will be seen, and therefore these soft collisions are called minimum bias events.

Proton beam energy	7.0 TeV
Bunch size	$75 \text{ mm} \times 16 \text{ } \mu\text{m} \times 16 \text{ } \mu\text{m}$
Collision frequency	40 MHz
Number of particles per bunch	$10^{11}$
Nominal luminosity	$10^{34} \text{ cm}^{-2}\text{s}^{-1}$
Circumference	26.66 km
Number of bending magnets	1152
Field of bending magnets	8.65 T
Radius of curvature	3.50 km
Number of interaction regions	2

Table 1.3: Some parameters of the LHC machine (taken from [8]).

### 1.3.2 The physics potential of the LHC

The Large Hadron Collider opens up a new range of energy. It allows for a discovery of the Higgs boson if it exists in the mass range 80–1000 GeV [10]. At the startup of the LHC, either the boson has been found at LEP200, or it does not have a mass below 80–90 GeV (see e.g. [11]).

The Higgs particle couples to mass, and can be found to decay in as heavy a particle as possible. When the mass of the  $H^0$  lies in the range 80–130 GeV, it decays predominantly into  $b\bar{b}$  quark pairs. Expectations are that the boson cannot be identified from this decay, because the direct production (not via  $H^0$ ) of  $b\bar{b}$  has a  $10^9$ – $10^{10}$  higher cross section [12] so that the Higgs signal will be flooded by this 'background'. In this mass range, we rely on a (higher order) decay into photons:  $H^0 \rightarrow \gamma\gamma$ . This decay is rare (its occurrence is about one in a thousand), but can be identified because the background due to two-photon occurrences is lower. (The techniques of particle identification are discussed in the next section.) The Higgs boson can also be found when lying in this range through associated production of a Higgs boson with a W or Z. At nominal luminosity, only a few tens of events of this type are expected *per year*. Nevertheless, the background is low so that an identification of the boson is feasible through this channel.

In the mass range 130–800 GeV, the Higgs boson can be identified easiest through what is called the gold-plated decay  $H^0 \rightarrow ZZ \rightarrow \ell^+\ell^-\ell^+\ell^-$ , where  $\ell^+\ell^-$  stands for  $e^+e^-$  or  $\mu^+\mu^-$ . (For  $m_H < 2m_Z$ , one of the two Z bosons is virtual.) The signature of four leptons in the final state can give a pronounced signal above the continuous background (mainly from the direct creation of two Z bosons in the proton-proton collision). This signal can only be seen when

a good lepton identification is reached, combined with an accurate measurement of the four-vectors of these particles (so that the error on the measured invariant mass is small). The detection of a Higgs boson through this gold-plated channel is discussed in detail in chapter 6 of this thesis.

Above 800 GeV, it becomes increasingly difficult to find the Higgs boson through the gold-plated channel, because the cross section for Higgs production becomes very low. In this region one can gain a factor 6 in statistics by taking into account not only the Higgs decay into four leptons, but also  $H^0 \rightarrow ZZ \rightarrow \ell^+ \ell^- \bar{\nu} \nu$ . The neutrinos leave nothing but a signature of missing energy, the two leptons can be identified. At this very high mass, low backgrounds are expected.

The Large Hadron Collider, in opening a new energy range, offers many more particle physics processes of interest than just the creation of the Higgs boson. First of all, the Standard Model is not all there is. Extensions to the theory like Supersymmetry and Technicolor should be tested on their validity, in particular in the context of Grand Unification Theories. To go into these models is way beyond the scope of this thesis.

The LHC also enables us to study the bottom and top quark in great detail. The current top quark studies at the Tevatron are severely limited by statistics. The mass of this quark will therefore not be determined very accurately. At the LHC, top quarks are produced at thousands per day, so its mass can be pinned down to an accuracy of around 3%, limited by theoretical uncertainties rather than statistics, and also its decay channels can be studied in detail.

The bottom quark will be produced at an enormous rate at the LHC, so in fact it can only be studied when the machine runs at a low luminosity (or in another configuration than the proton-proton collision mode<sup>2</sup>). In bottom quark decay the invariance under time reversal may be violated. This effect has only been seen elsewhere in the decay of K-mesons and it is not very well understood yet.<sup>3</sup>

Finally, the collider allows us to directly observe the tau-neutrino ( $\nu_\tau$ ). This particle is difficult to identify as it hardly interacts with matter, the best visible reaction being  $\nu_\tau + e^- \rightarrow \tau + \nu_e$ . When a large flux of tau-neutrinos can be achieved in a large amount of material, the particle may be recognised from the sudden appearance of a tau lepton. The experiment sketched here is not easy, because the tau lepton decays very quickly ( $c\tau \approx 90 \mu\text{m}$ ). The tau lepton decay vertex must be seen to identify the tau-neutrino through this process. No tau-neutrino experiment has been proposed yet to the LHC committee.

Cross sections and production rates of various particles are displayed in figure 1.1, which is very illustrative in showing the difficulty in finding heavy particles such as the Higgs boson. It takes  $10^{11}$  collisions to create one Higgs boson (if  $m_H = 500 \text{ GeV}$ ).

---

<sup>2</sup>The LHC machine will also be used to collide heavy ions, and fixed target experiments are foreseen with one of the proton beams.

<sup>3</sup>In fact one observes a violation of the invariance under inversion of charge and parity (C and P). This is equivalent to a violation of time reversal (T) invariance if one accepts the CPT-theorem.

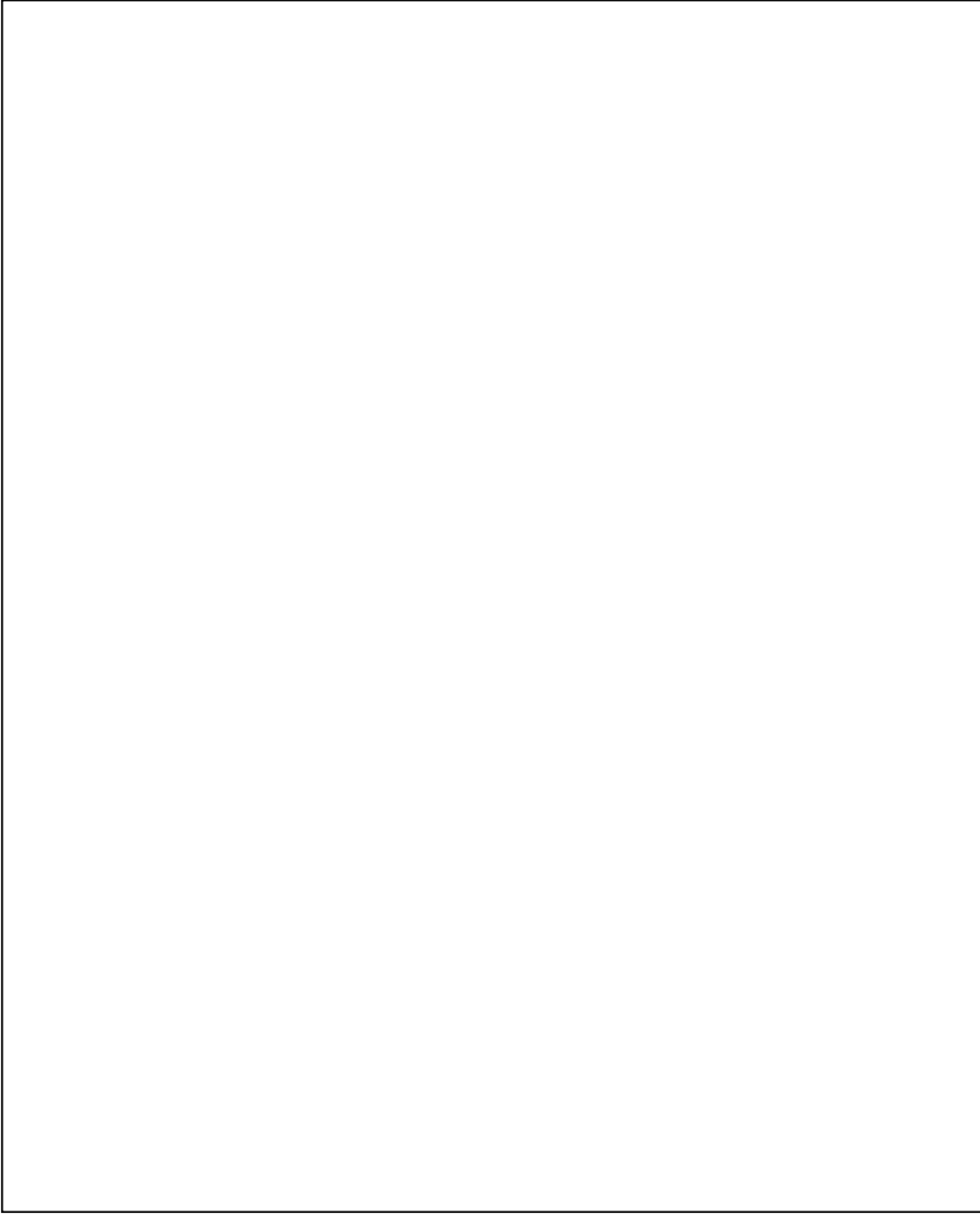


Figure 1.1: *The cross-section of some characteristic processes like the production of a Higgs boson (lowest curve) and the total cross-section (top curve), as a function of the proton-proton accelerator energy. Taken from [12].*

### 1.3.3 The experiments

To identify and study any of these predicted particles, an arrangement of particle detectors will be built around the points where protons are brought into collision. New particles are either identified by their decay products or on the contrary by the lack of decay products. For instance, an intermediate mass Higgs boson can decay into two photons with a distinct invariant mass equal to the mass of the Higgs boson. A supersymmetric particle will decay in detectable and undetectable particles, so a collision can be identified, but part of the collision energy seems to have disappeared. The purpose of an experimental setup at the Large Hadron Collider is therefore to identify all particles coming out of a collision, and measure their energy. From this information we try to reconstruct the underlying collision process.

Two types of detectors are used in LHC experiments: tracking detectors, which measure the position of a crossing particle with minimal interference, and calorimeters, which measure the energy of a particle by total absorption. For particle identification, both these tools are used. From the collision point outward we have first an arrangement of tracking detectors, then a calorimeter, and then tracking detectors again (see fig. 1.2). Each particle has a different signature in this arrangement, as shown in the figure for the most important particles. These signatures are by far the most probable patterns to be found, but in some cases a charged pion may leave the signature of an electron, etc.

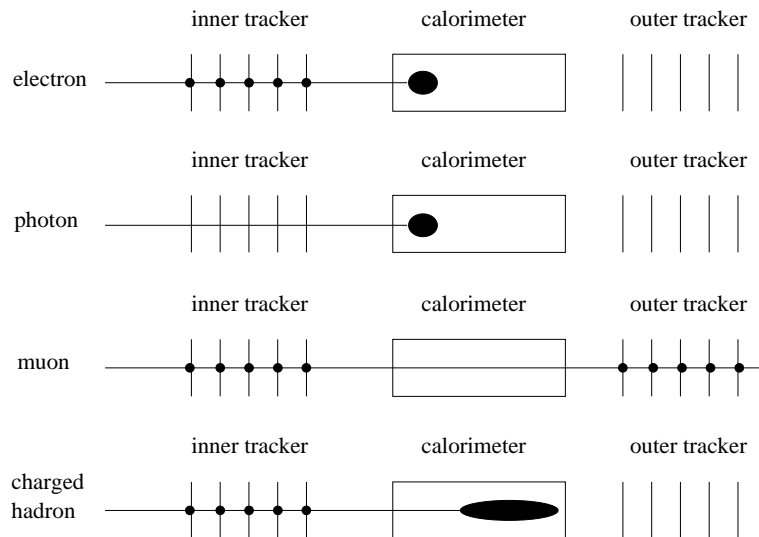


Figure 1.2: Signature of some highly energetic particles in a tracker, electromagnetic calorimeter, hadronic calorimeter and muon tracker. An electron (or positron) deposits a little energy in the inner tracker elements, and all of its remaining energy in the first part of the calorimeter. Photons leave no trace in the inner tracker; hadrons shower deeper into the calorimeter than electrons and photons. Muons traverse the calorimeter and leave a signal in the trackers. Jets are a combination of hadronic and electromagnetic particles, and generally give rise to activity in most detectors.

Electron, muon and photon identification is the prime tool of LHC experiments. But not only 'single' particles are studied. The collision of protons results in the production of streams of particles in certain directions, called jets. These jets are created by a quark or gluon with a large kinetic energy. They contain hadrons like pions and kaons, but through further decays of the jet contents they may include muons, photons and electrons. The signature of a jet is a number of tracks and calorimeter clusters close to each other. The accurate measurement of the energy and the lepton content of a jet gives a means of determining the top mass to an accuracy of  $\pm 6$  GeV [65]. The spectrum of the total jet energy can reveal a quark substructure [13]. Jets are however mostly considered as a source of problematic background levels. When most of the jet energy is carried by one particle, the jet may be misidentified as a single particle. Most problematic in this sense are single pions that create an electromagnetic shower, because they leave photon or electron signatures.

The two experiments proposed to run at the Large Hadron Collider, A Toroidal LHC Apparatus (ATLAS) and the Compact Muon Solenoid (CMS) are displayed in fig. 1.3 and 1.4. In both experiments, the sequence of tracking-calorimetry-tracking is pursued all around, except for the region around the beam where the particle flux is so high that particle identification becomes very difficult.

The two experiments are complementary in the sense that CMS focuses on the accurate measurement of muon direction and momentum, while the ATLAS collaborators intend to compromise a bit on the muon measurement while gaining in electron, photon and jet measurements. It is common practice in High Energy Physics to build two complementary general purpose experiments for a proton collider, to fully exploit the accessible spectrum of particle physics research. The ATLAS experiment will be described in chapter 5.

#### 1.3.4 Research

The ATLAS and CMS detectors consist of many different particle detectors, like Silicon Strip detectors, Microstrip Gas Counters and Liquid Argon Calorimeters, and all these detectors have one thing in common: they were developed specifically to meet the heavy experimental requirements of the Large Hadron Collider. This development was started in High Energy physics laboratories around the world, and was later on coordinated at CERN by the Detector Research and Development Committee (DRDC), founded in 1990. The committee was assigned the task to distribute the available CERN resources over those groups proposing to do detector R&D, and to monitor their progress. Over 30 collaborations were formed under the DRDC flag. These collaborations carry the code names RD1, RD2, etc. One of these collaborations, RD28, is devoted to the research and development of the Microstrip Gas Counter towards the LHC experiments [14]. For this specific detector, R&D had already started in 1986, and at the time of approval about 30 laboratories were working on it.

The following chapter will introduce the Microstrip Gas Counter, and describe its functionality in detail. Chapter 3 describes the results of seven years of R&D by a growing community of physicists. In chapter 4, a Monte Carlo model of the detector operation is presented. In chapter 5 and 6, we will turn from the physics of particle detection to the physics of particle discovery.

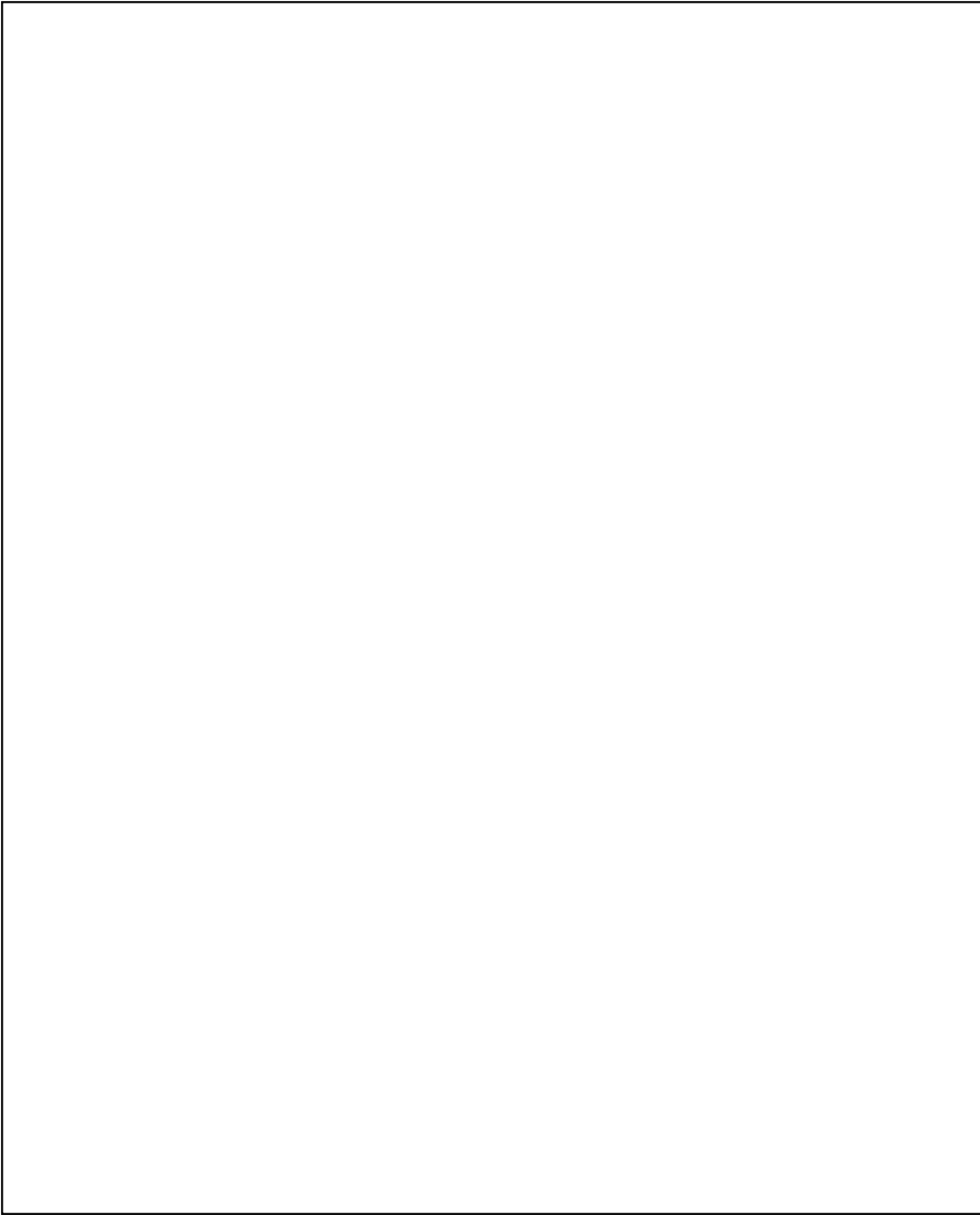


Figure 1.3: *The proposed ATLAS experiment for LHC.*

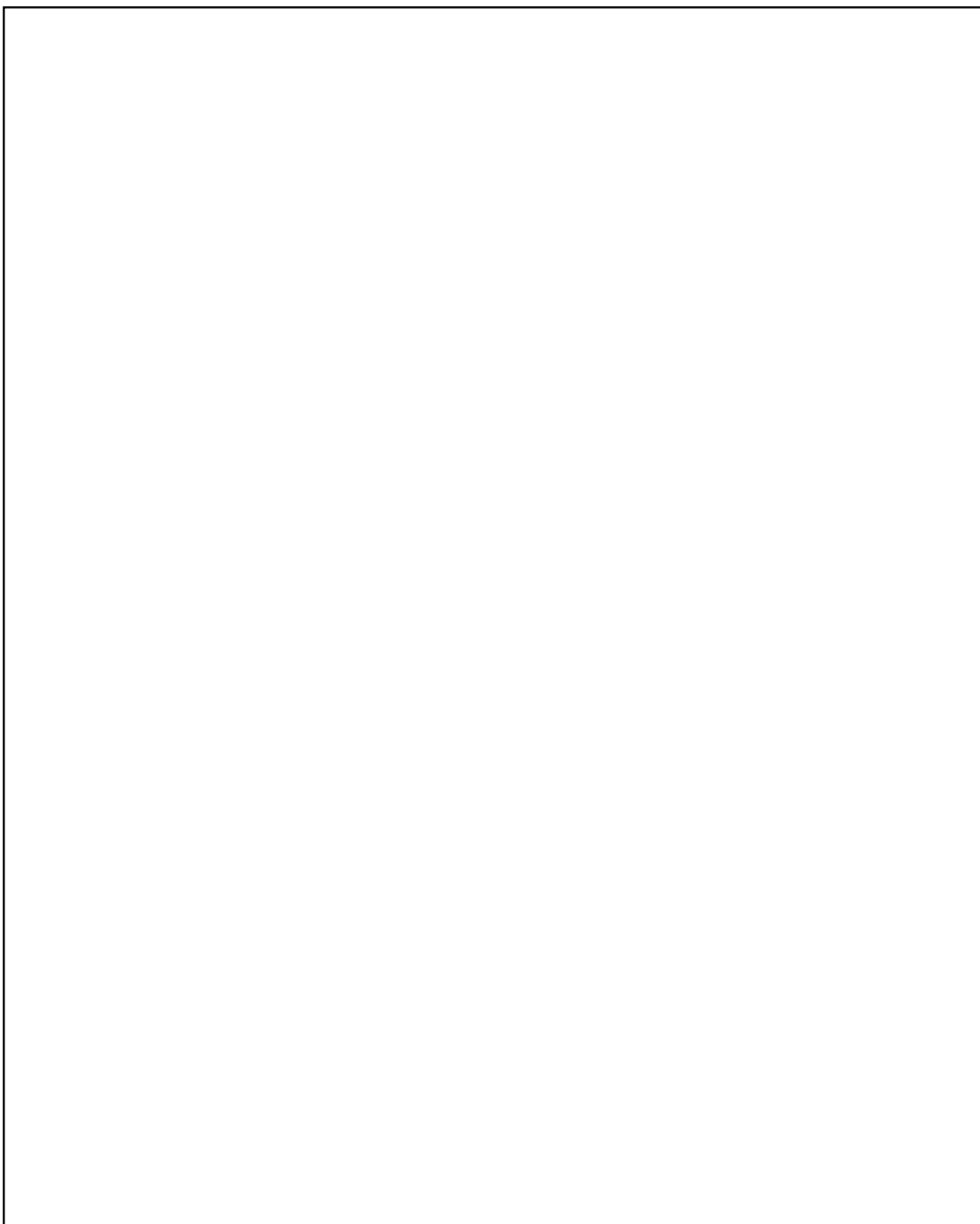


Figure 1.4: *The proposed CMS experiment for LHC.*



## Chapter 2

# Description of the Microstrip Gas Counter

### 2.1 Introduction: the multiwire proportional chamber

As mentioned in the previous chapter, one of the newly developed detectors that will be used in LHC experiments, is the Microstrip Gas Counter (MSGC). This detector is a modern variety of the Multiwire Proportional Chamber [15] shown in figure 2.1. As the geometry and operation of the MSGC are very similar to that of an MWPC, the latter detector will be described first as an introduction to the MSGC.

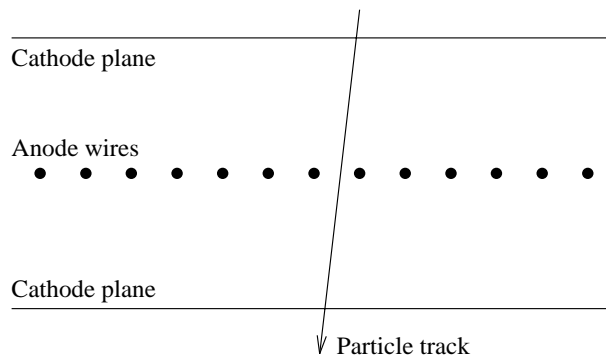


Figure 2.1: *Outline of the multiwire proportional chamber. Wires on a high voltage are strung parallel in a gas volume, closed by conducting planes on a low voltage. A particle crossing this gas volume may be detected by the ionisation trail it leaves behind in the gas.*

The MWPC is a detector for charged relativistic particles and photons. When these particles cross the active volume of an MWPC, a gas volume, they ionise gas molecules on their way. The gas volume is enclosed by cathode planes with a plane of anode wires in between (following the concept of a Geiger-Müller counter). The electric force makes the liberated electrons move towards the anodes, and the (positive) ions to the cathode planes.

The electrons will cause a signal on the anodes when the electric field strength around these anodes is very high, as will be explained later on. When the anode region is segmented, one receives position information of the original ionisation because only a few of the anode segments will have a signal.

More specifically, the sensitive plane of the MWPC consists of a set of parallel anode wires (usually tungsten, copper or aluminium). The position information achieved from the anode segmentation is most accurate when particles cross the gas volume in the direction perpendicular to the anode plane.

## 2.2 The invention of the MSGC

The MSGC is the result of a series of attempts to build a highly granular Multiwire Proportional Chamber in which the sense (anode) wires are less than 2 mm apart. Closer sense wires give better spatial resolution and allow for higher particle fluxes, but there is a physical limit to the miniaturisation of the MWPC along this line. To achieve sufficient gas amplification with small wire distances, there should be a cathode close to the sense wires. In practice, these wires are therefore often interleaved with cathode wires. The smaller the inter-wire distance is made, the higher the electrostatic forces become. Eventually this leads to an excessive displacement of the wires.

This displacement can be reduced by fixing the wires e.g. each 10 cm using insulating spacers. The extrapolation of this solution, to fix the wires all along, was first made in 1970 by Neumann and Nunamaker who constructed a detector consisting of wires attached to an insulating foil. They achieved rather promising results [16], but this research was not pursued much further.

In 1986 Anton Oed from the Institut Laue-Langevin, Grenoble, came with a new approach. He realised that the chip processing technology had reached a level of sophistication that enabled printing of conductor patterns on various (flat) carriers. Oed built a particle detector with Chromium anode and cathode strips on a small glass plate, and published his findings in 1988, which marked the birth of the Microstrip Gas Counter [17].<sup>1</sup> The detector introduced in this paper is shown schematically in figure 2.2. On a glass plate, thin parallel anodes are interleaved with broader cathode strips which shape the field. This plate is positioned in a gas volume which functions as the active medium: passing particles can ionise molecules in this gas volume, and the negatively charged drift plane pushes the liberated electrons towards the anodes. Close to these anode strips, the electric field is extremely high ( $\gg 100$  kV/cm) so that each free electron causes a cascade of additional free electrons, resulting in a measurable signal (or current) on the anode strip. Particles are meant to enter the detector perpendicular to the substrate surface (from either side). The bottom side of the substrate is covered with a thin metal layer on a fixed potential.

Oed's detector shows a number of advantages over the classical wire chamber:

---

<sup>1</sup>The device was originally called 'MS-detector' (Micro-Strip detector); however, as Silicon Strip Detectors are often called Microstrip Detectors, this name leads to confusion. In 1993, the community decided to adopt the predicate MSGC [18] which was introduced by the NIKHEF group in 1991.

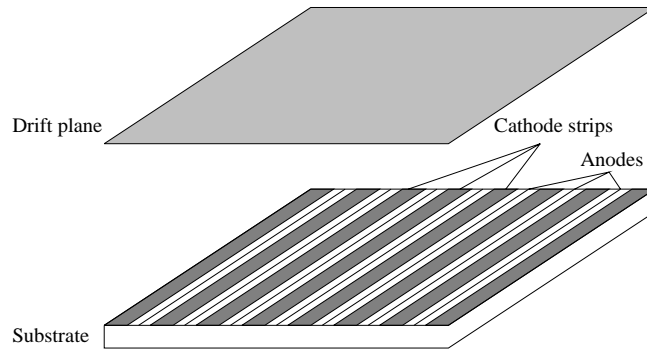


Figure 2.2: Outline of the MSGC detector: a substrate carrying conductive strips is positioned in a gas volume, covered by a conductive drift plane.

- The high granularity of this device enables an accurate position determination of the liberated charge (by identifying which of the anode strips register a signal) and hence tracking of the ionising particle.
- The maximum flux an MSGC can stand is higher than for an MWPC. Generally the maximum tolerable flux of a detector is inversely proportional to the area of one sensitive cell, and to the duration of the signal. The cells of an MSGC are an order of magnitude smaller than MWPC cells. The signal on an MSGC anode is much faster than on an MWPC anode, because the positive ions are collected quicker which follows from the detector geometry.
- Having many fixed strips on one substrate makes the accurate positioning of the sense strips within a gas volume much easier than if anode wires must be strung individually. The printing process is performed such that almost identical copies can be made using a single mask.
- There is no need of a strong frame to take the tension of the wires.
- When a strip breaks, it remains fixed to the substrate. In wire chambers the breaking of a wire often causes catastrophic changes of the electric field and short circuits. A broken MSGC strip can do little harm.

The main drawbacks of the MSGC (not surprisingly) have to do with the substrate which carries the strip pattern. This substrate should influence the detector operation as little as possible: the detector should function as if the substrate were not there. This is in practice very hard to achieve: electrons, ions and gas pollutants can stick to this substrate and cause a modification in the field, discharges, radiation damage, etc. This is further discussed in chapter 3.

The MSGC can be seen as an intermediate tracking detector, with charged particle detection qualities lying between those of an MWPC and a Silicon Strip Detector: the position resolution of  $30 \mu\text{m}$  and signal speed  $< 50 \text{ ns}$  are better than those achieved with an MWPC,

but not as good as the performance of Silicon Strip Detectors. The radiation hardness study of Sauli et al. [19] shows that the detector can be more radiation resistant than the others under particular conditions.

## 2.3 Charged particle detection with the MSGC

### 2.3.1 Introduction

In this section we discuss the detection mechanism for relativistic charged particles. The operation of the MSGC is very similar to that of the MWPC. When the detector is used to study relativistic particles, we are mainly interested in three properties of the particle: its location in space, its time of passage and its energy loss in a certain amount of material. In the case of the LHC trackers, the localisation of the particle tracks is essential to determine their production vertex, their momentum and finally their identity. On the other hand we want the particle to be 'undisturbed' by the measurement, i.e. it should cross as little material as possible so that energy loss and scattering are reduced to a minimum. The ideal orientation of an MSGC in this case is when the strip plane is perpendicular to the particle direction. In this orientation the particle travels through a minimum amount of substrate and cathode plane material.

When the relativistic particle crosses the gas volume, it ionises gas molecules on its way. This ionisation trail will be pulled apart by the electric field: the positive ions are pulled towards the cathode plane, and the electrons will move towards the anode strips. The ions are discharged at the cathode plane. The electrons however will cause a cascade of other electrons when they reach the high electric field close to an anode strip. This cascade can be detected with sensitive electronics, and when more than one strip senses a cascade, the ratio of the signal strength on neighbouring strips gives us the approximate position of the crossing particle. The signal height on the anode strips is roughly proportional to the energy loss of the particle in the gas. So particle detection with the MSGC comes down to the analysis of the signals on the anode strips.<sup>2</sup>

In the next sections the detection process discussed above is discussed in more detail. This facilitates the later description of the Monte Carlo simulation of the detector.

### 2.3.2 Ionisation of a gas

As any other particle detector, the MSGC relies on the interaction of a moving particle with the material it traverses. Like in MWPCs, the interaction is electromagnetic and the active material is the gas. Charged particles have an average energy loss per unit length  $-dE/dx$  given by the Bethe-Bloch equation [2] (not valid for electrons):

$$-dE/dx = 4\pi N_A r_e^2 m_e c^2 z^2 \frac{Z}{A} \frac{1}{\beta^2} \left[ \log \frac{2m_e c^2 \gamma^2 \beta^2}{I} - \beta^2 - \frac{\delta}{2} \right]. \quad (2.1)$$

---

<sup>2</sup>The signal on the anodes is counterbalanced by a signal of opposite sign and almost equal magnitude on the cathode strips; there is therefore no fundamental difference between MSGCs with anode readout and MSGCs with cathode readout, although there are subtle differences [20].

The energy dependence can be found in the velocity  $\beta = v/c$  and the Lorentz factor  $\gamma = (1 - \beta^2)^{-1/2}$ . The dependence on the material is in the nuclear charge  $Z$  (in units  $e$ ) and the atomic mass number  $A$ . The density is accounted for in  $dx$  which is measured in  $\text{g}/\text{cm}^2$ . The charge of the traversing particle is  $z$ ;  $I$  is the ionisation constant, and  $\delta$  represents the effect of polarisation of the medium.

The charged particle energy loss shows a broad minimum around  $\gamma = 3.2$  [2]. Charged particles with this minimum energy loss are called minimum ionising particles (or 'mips'). These particles are often used to quote the benchmark performance of a detector when used for charged particle tracking. If it has a certain detection capability for mips, the properties of the detector are usually somewhat better for particles with a higher energy loss.

In wire chambers and MSGCs, charged particles can be traced because they ionise gas molecules along their way. A charged particle leaves behind a trace of free charges, electrons and ions, and the detection of the particle amounts to the localisation of these charges in the gas volume. For each collision, cross sections apply which are dependent on the type and energy of the incoming particle and the type of molecule. To translate these cross sections into a directly measurable quantity one usually defines the primary ionisation density  $n_P$  which can be written as

$$n_P = \rho \sigma_{ion}, \quad (2.2)$$

where  $\rho$  is the number of molecules per unit volume, and  $\sigma_{ion}$  the total cross section for ionisation. The ionisation cross section is of the order of  $10^{-18} \text{ cm}^2$ .

The result of an ionising collision is that the incoming particle is scattered and loses energy. In high energy physics experiments, we usually measure tracks of relativistic particles, with a kinetic energy much larger than the energy lost in an ionising collision. So both the energy loss and the scattering can be neglected. We can therefore assume that particle trajectories are straight lines, and moreover that subsequent collisions are independent (because the cross section does not change, as the particle energy is hardly modified). In that case, the actual number of ionisations per unit length follows a Poisson distribution with mean value  $n_P$ .

The liberated electron is emitted in a direction almost perpendicular to the track direction, unless the electron kinetic energy is very high [21]. The electron may ionise one or a few other molecules if its kinetic energy is high enough. Consequently, the observed number of free electrons (and ions) is higher than  $n_P$ . The average number of electron-ion pairs liberated per unit length is denoted  $n_T$ , the total ionisation density.

For minimum ionising particles,  $n_P$  and  $n_T$  are listed for a number of commonly used gases in table 2.1. When a mixture of gases is used,  $n_P$  can be calculated by weighting the relative abundance of components (as subsequent collisions are independent). In most cases  $n_T$  can also be calculated by averaging [23], but the Penning effect [24] can lead to a total ionisation density greater than the one expected from averaging (because excitation of one molecule is converted into an ionisation of another molecule).

The average kinetic energy of a primary electron liberated by a mip amounts to a few tens of eV. The distribution of the probability for an electron to receive an energy  $E$  goes approximately as  $E^{-2}$  when  $E$  is much larger than the electron binding energy (Rutherford scattering), so it has a long tail (limited at the maximum energy transfer that is kinematically

Gas	$n_P$	$n_T$
	( $\text{cm}^{-1}$ )	( $\text{cm}^{-1}$ )
He	3.3	7.6
Ne	10.9	39.9
Ar	24.8	96.6
Kr	33.0	197.5
Xe	44.8	313.3
CH <sub>4</sub>	24.8	59.3
C <sub>2</sub> H <sub>6</sub>	40.5	117.7
C <sub>3</sub> H <sub>8</sub>	67.6	176.5
iC <sub>4</sub> H <sub>10</sub>	83.6	232.8
DME	55	*
CO <sub>2</sub>	33.6	100.0

Table 2.1: Primary and total ionisation densities of mipcs for gases commonly used in gas filled particle detectors (at standard temperature and pressure) [22]. For DME (dimethyl ether),  $n_T$  was never published.

allowed in the collision). This means that a small fraction of the primary electrons have an energy large enough to travel a macroscopic distance through the gas while ionising molecules. The free charge in the gas volume does not occur exactly along the track of the original particle in this case, which can lead to an error in the position determination of the particle.

Not much is known about the statistical distribution of the number of electrons in an ionisation cluster. Given  $n_P$  and  $n_T$ , the average number of electrons per cluster is known, but actual distributions are hardly ever measured and theoretical distributions (even when starting from first principles) are not accurate. Measurements on the cluster size are presented in [25] for a few gases, including a thorough discussion of the observed discrepancy with various theoretical models.

### 2.3.3 Drift and diffusion of electrons and ions

The electric field in MSGC detectors is illustrated in figure 2.3. All field lines end on anode strips, so we can expect that an electron is submitted to a force towards an anode, wherever it is liberated within the gas volume. The result of this force is a motion globally along the field line ('drift'); because of numerous elastic collisions of the electron with gas molecules the electron will lose speed and change direction<sup>3</sup>. The drift is characterised by an average drift velocity  $v_D$  and two diffusion parameters. On average the electron drifts along a field line, with the average drift velocity. The deviation away from the field line (perpendicular to it) is called transverse diffusion. The deviation along the field line (caused by a statistically

---

<sup>3</sup>The use of gases that 'absorb' free drifting electrons by attachment, such as O<sub>2</sub>, is usually avoided in gaseous detectors.

Figure 2.3: *Electron trajectories in the MSGC.*

varying drift velocity) is called longitudinal diffusion. Both diffusion effects originate from random walk processes and thus follow a Gaussian distribution with a variance proportional to the number of collisions. This implies a proportionality with the distance  $L$  traveled by the electron (on a macroscopic scale). Thus we can define the transverse and longitudinal diffusion coefficients  $\sigma_T$  and  $\sigma_L$  as follows:

$$\Delta R = \sigma_T \sqrt{L}; \quad (2.3)$$

$$\Delta L = \sigma_L \sqrt{L}, \quad (2.4)$$

where  $\Delta R$  ( $\Delta L$ ) is the width ( $\sigma$ ) of the transverse (longitudinal) distribution of electrons after drift over a distance  $L$ .<sup>4</sup> Although the electron does not move along a straight line, for  $L$  one usually takes the straight-line distance between the liberation point and the end point. The drift velocity and diffusion coefficients are important parameters when a gas mixture is selected for the use in a track detector, because they can influence the detection accuracy and speed. For this reason these properties were measured for many gas mixtures under different conditions. A compilation of these measurements is given in [26]. The gas mixture optimisation problem is treated in section 3.9.3 for the application of MSGCs in LHC experiments.

The drift velocity and electric field are interrelated by the mobility  $\mu$  of the charged particle, according to

$$\vec{v} = \mu \vec{E}. \quad (2.5)$$

---

<sup>4</sup>By some authors, the widths  $\Delta R$  and  $\Delta L$  are sometimes denoted as  $\sigma_T$  and  $\sigma_L$ , respectively.

For low values of  $E$ ,  $\mu$  is a constant [27].

The positive ions drift towards cathode planes in the opposite direction of the electrons. Because of their size, the drift velocity of ions is much smaller (a factor  $10^3$ – $10^4$ ) than of electrons. The ions will therefore remain in the gas volume until long after the electrons have reached the anode. Also, the diffusion coefficients of ions are higher than of electrons.

When the detector is placed in a magnetic field, the drift behaviour of charged particles changes. The Lorentz force operates on a moving charged particle when it has a velocity component perpendicular to the magnetic field, so that the total force on the charged particle becomes

$$\vec{F} = q\vec{v} \times \vec{B} + q\vec{E}, \quad (2.6)$$

where  $\vec{B}$  is the magnetic and  $\vec{E}$  the electric field (both could be dependent on the position in space). The velocity of a drifting particle changes with each collision, and the net effect is that the drift of electrons does not follow the electric field lines, but a path that is tilted w.r.t. these field lines in the direction of  $\vec{E} \times \vec{B}$ . The tilt angle is called the Lorentz angle  $\alpha_L$ , and can be expressed in terms of the mobility [28]:

$$\tan \alpha_L = \mu B. \quad (2.7)$$

The Lorentz angle is usually undesired and where possible the effect of the magnetic field is minimised by either choosing settings where the Lorentz angle is minimal, or orienting the detector such that  $\vec{E} \parallel \vec{B}$  (corresponding to Lorentz angle zero).

Another solution is to orient a detector such that the relativistic charged particles will cross the detector along a line of electron drift, just as in the nonmagnetic case. The detector is then rotated over the Lorentz angle, if  $\vec{E} \perp \vec{B}$ . For a more extensive discussion of gas detectors in magnetic fields, see [23].

### 2.3.4 Gas amplification

When a drifting electron enters a region with very high electric field strength, it will cause a cascade of other free electrons because the electric force will give it enough energy to ionise other molecules. In the MSGC, a strong electric field is created close to the anodes by adding cathode strips in between the anodes. (This high field strength can also be achieved without the cathode strips, but only when the anodes are very narrow and set to an extremely high voltage.) The ionisation probability of a drifting electron per unit length is called the first Townsend coefficient,  $\alpha$ . A commonly used approximation suggested by Korff gives the following relation between  $\alpha$  and the electric field [29]:

$$\alpha = \frac{A}{\lambda} e^{-AV_{ion}/\lambda E}, \quad (2.8)$$

where  $V_{ion}$  is the effective ionisation potential of a gas molecule,  $\lambda$  is the mean free path of the electron, and  $A$  is a constant. This theory gives good predictions for low values of  $\alpha$ . The ionisation probability becomes significant in the range  $10 \leq E \leq 100$  kV/cm (at standard temperature and pressure). The electric field strength close to an MSGC anode is plotted in

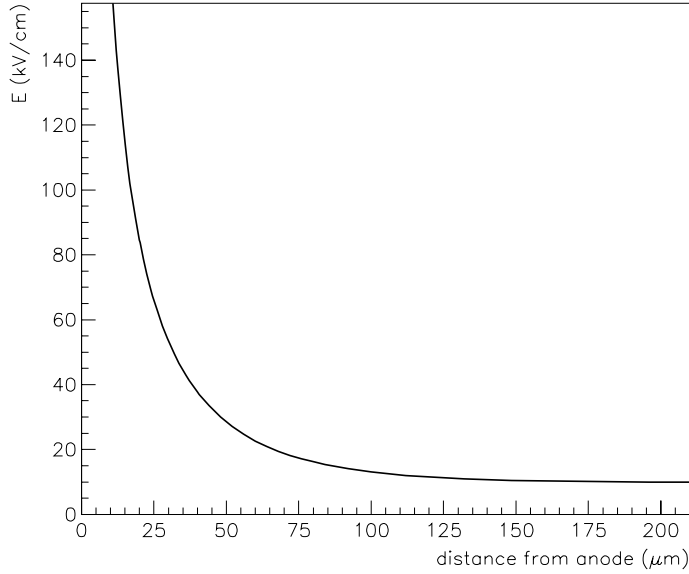


Figure 2.4: The electric field strength straight above an MSGC anode, for typical dimensions and operation voltages, and a drift field of 10 kV/cm.

figure 2.4. There is a region of around 30  $\mu\text{m}$  in which many ionisations occur. Each liberated electron will start drifting towards the anode and take part in the ionisation of gas molecules so that an exponential increase of the number of free electrons can be expected in this region. This process where one free electron liberates many others, is called gas amplification or gas multiplication. In this process many millions of electrons can be liberated by one initial electron, but in MSGCs the nominal gas amplification factor is kept below  $10^4$ , usually.

If the gas amplification is lower than about  $10^5$ , the total number of liberated electrons is proportional to the initial number of free electrons. At higher amplification saturation effects occur: so many ions are produced in the avalanche that they disturb the electric field, shielding the anode and reducing the electric field strength in the amplification region. Beyond the proportional region, the region of limited proportionality follows, and when the gain factor is even increased further we enter the region of limited streamers. A thorough discussion of the higher amplification regions can be found in many references, amongst which [27].

The proportional region is characterised by the linear relationship between the number of electrons  $N_{amp}$  found after gas amplification and the number of initiating electrons  $N_{ini}$ :

$$N_{amp} = G N_{ini}, \quad (2.9)$$

where  $G$  is the (average) gain factor. The gas amplification is a statistical process so that the actual gain for one single electron fluctuates. The fluctuations around the average value of  $G$  are usually described with the Polya distribution [30]

$$P_m(x) dx = \frac{m(m x)^{m-1}}{\Gamma(m)} e^{-m x} dx. \quad (2.10)$$

So the probability to find a gas amplification  $g = xG$  is given by  $P_m(x)$ . The mean value of the Polya distribution is 1, the variance  $m^{-1}$ .  $P_{3/2}(x)$  is called the Curran distribution [30, 31], which is a good approximation of the gas gain fluctuations in wire chambers.

### 2.3.5 Signal development

Ideally, all liberated electrons end on the anode strip of the MSGC. The positive ions in the gas drift towards cathodes and are collected there. This means that a current is flowing through the gas. With sensitive electronics, this current can be measured. So the detection of a charged particle finally comes down to the measurement of an electric quantity, which is very convenient for automatic data processing. However, the current in an MSGC is so small, that only state-of-the-art electronics can fulfill the task of discriminating a particle from (electronic) noise.

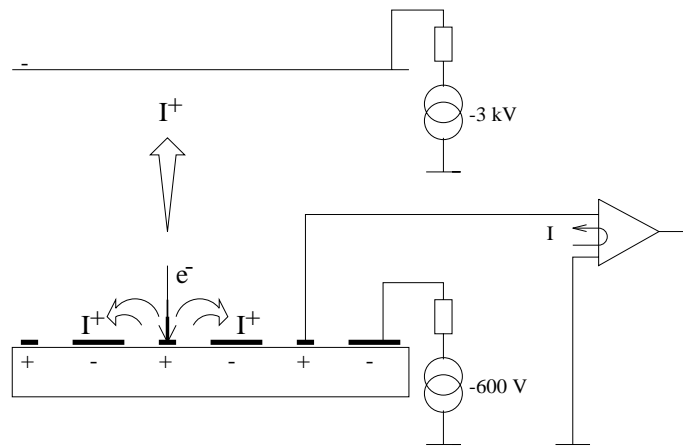


Figure 2.5: *Electron and ion currents in the MSGC and a simplified scheme of the electronic connections to the electrodes (in the case of anode readout). Each anode has its own preamplifier. The values of the voltages are indicative.*

Figure 2.5 gives an overview of the electric behaviour of the MSGC. The currents running through the gas are indicated. When the voltage settings are appropriately chosen, the majority of the positive ions liberated in the gas amplification process will be discharged at the cathode strips, not at the drift plane. (The ions will only have a chance to move into the drift field when the ion diffusion coefficient is very small and the drift field strength is large<sup>5</sup>.) This means that the ions are rapidly discharged. Each anode is connected to a sensitive charge amplifier so basically the electron current is measured.

The development of the current in the anode is dictated by the behaviour of the positive ions around the anode: as long as these ions are close to the anode, they induce charge on the

<sup>5</sup>In the nominal operation conditions described in the next chapters, in fact the diffusion coefficient is low (in DME/CO<sub>2</sub>) and the drift field high (7–10 kV/cm); under these circumstances about half the ions drift towards the cathode plane.

surface of the anode and so as many electrons are held at the strip surface as were liberated in the avalanche. When the ions move away they come closer to a cathode strip and cause an induction charge on that strip, while the induction charge on the anode is released. Only then, the electrons now free on the conducting anode will cause a current from the anode to ground (through the preamplifier). It is therefore important that the ions reach the cathode strips quickly, if we want to have a fast signal.

Parasitic capacitances between the strips and ground add to the complexity of the signal development: they slow down the signal and increase the preamplifier noise. The electrostatic coupling between anode and cathode strips can cause ghost signals on neighbouring strips (crosstalk). The resulting signal speed of a single avalanche is of order 10 ns, as measured by Smadja [32] and discussed on the basis of simulations in ref. [33].

The properties of the detected particle are derived from the signals collected on the electrodes. When the MSGC is used to detect perpendicularly incident charged particles, we can expect a signal from the crossing particle on the anode strip that lies right under the track segment of the particle in the gas. Also the neighbouring strips can have a relatively small signal because of the transverse diffusion of the electrons during their drift. If a perpendicular track crosses physically through an anode, the left and right neighbours will have equal signals on average, and the central strip has a much higher signal. If on the other hand the track crosses a cathode strip, the charge will be shared equally between the surrounding anodes. So the distribution of the electrons on the anodes (and hence the anode signals) gives us information about the position of the track within the detector. The particle position can be calculated with various algorithms which take into account this specific behaviour of the distribution; it turns out that a centre of gravity calculation gives very accurate results. In this way the position resolution of MSGC prototypes was measured to be 30  $\mu\text{m}$  for beam particles (see [34] and sections 3.9.3 and 4.3).

The sum of the signals on the anode strips is proportional to the number of liberated electrons, so this gives an indication of the energy loss of the particle in the gas. This proportionality is global and not valid from event to event because gas amplification statistics influence the size of the signal. The fluctuations in gas amplification were found to be rather low for MSGCs in argon based mixtures: down to 11% FWHM <sup>6</sup> for 5.9 keV photons from <sup>55</sup>Fe decay [35, 36].

## 2.4 Photon detection with the MSGC

Apart from ionising particles the MSGC can be used for photon detection. Photons in the visible and UV range can be detected using the photo-electric effect; photons with an energy larger than  $2m_e$  can be converted into an  $e^+e^-$  pair inside the gas volume, which leaves an ionisation trail. Photons in the intermediate energy range create free charge in the gas via the Compton effect. The liberated charge created in the gas volume will cause a signal on

---

<sup>6</sup>Full Width at Half Maximum: disregarding the precise shape of the peak, we can express the width of this peak by determining the distance between the two points on either side of the peak where the amplitude is  $\frac{1}{2}$  of the peak amplitude. If this is expressed in a percentage, this distance is related to the position of the peak.

the electrodes just as described in the previous section. An example of the use of MSGCs for photon detection is given in [37].

## 2.5 Aspects of the electric field

The gas volume between the strip surface and the drift electrode can be divided into two regions. Close to the microstrips a quadrupole field exists. In this quadrupole region the electric field strength is very high and inhomogeneous. It extends out to a height above the strip surface equal to the pitch of the anodes. Beyond this border, the fine granularity of the strips is invisible to probe charges, and the field is homogeneous with a direction perpendicular to the strip plane and the drift plane (if these are parallel). This region is called the drift volume, because here the electrons and ions merely drift (while in the quadrupole region they take part in a cascade).

All the electrons liberated in the drift field follow very closely the same trajectory when they come close to the anode, so we can assume that electrons from this region have the same gas amplification. Electrons liberated in the quadrupole region however, follow different paths. In most cases this leads to a higher gas amplification because the electric field in most of the quadrupole region is very high. An experimental observation of this effect is reported in section 4.4.

Ideally the electric field in the MSGC gas is symmetric w.r.t. each vertical plane through an electrode centre. In reality the detectors will carry a finite number of strips resulting in field distortions at the edges. It is therefore advisable to end with a broad strip on an intermediate voltage between the cathode and anode strip potential. Otherwise the field lines in the drift region will not be straight, leading to a loss of position accuracy. At the ends of the strips, the same problem occurs, but here the bending of field lines takes place mainly in the direction along the strips, which does not affect the position resolution.

The electric field has to be 'finished' not only at the edges of the substrates, but also at the back side of the strip substrate. Here a conductive layer is added which is often set on the anode voltage. In fact a small induced signal can be measured on this back electrode, and when the substrate is made thin enough this signal can be used to determine the position of a track in the coordinate along the strips which turns the MSGC into a two-dimensional track detector (e.g. through the segmentation of the back electrode). This subject is discussed in section 3.6.

The details of the electric field in the MSGC are very important to its operation. Numerical computations of the field characteristics are reported in [38].

## Chapter 3

# R&D of the Microstrip Gas Counter

The text of this chapter is based on experience with MSGC prototypes obtained in experiments of many groups. The research and development work that the author took part in, was published in the following articles:

F. HARTJES, B. HENDRIKSEN, J. SCHMITZ AND F. UDO, *Recent tests with a gaseous microstrip chamber*, CERN 89-10 (II) 455;

F. HARTJES, B. HENDRIKSEN, J. SCHMITZ, H. SCHUIJLENBURG AND F. UDO, *Operation of the microstrip gas detector*, Nucl. Instr. and Meth. A310 (1991) 88;

M. GEIJSBERTS, F. HARTJES, J. PANNEKOEK, J. SCHMITZ AND F. UDO, *Optimization of the microstrip gas counter*, Nucl. Instr. and Meth. A315 (1992) 529;

M. GEIJSBERTS, F. HARTJES, J. PANNEKOEK, J. SCHMITZ AND F. UDO, *Tests of the performance of different gas mixtures in microstrip gas counters*, Nucl. Instr. and Meth. A313 (1992) 377 (printed at the end of this chapter).

### 3.1 Introduction

The MSGC was invented as a solution to the problem of limited granularity of an MWPC. This problem only occurs in experiments where a high position accuracy is needed in combination with a high particle flux. In case of a low particle flux an MWPC used in drift mode is a very elegant solution with good position resolution. A high particle flux asks for highly granular devices with high speed. So the MSGC is an interesting particle detector for the use at the Large Hadron Collider, but also for smaller experiments where the particle flux is high, like in the SODART X-ray telescope [37] and the Spin Muon Collaboration experiment at CERN [39].

There is a long way to go between the invention of a new detector concept and its application in a physics experiment. Many aspects of the detector operation and production must be extensively tested before the device can be built into a reliable instrument for experimental physicists. After the Oed paper [17] several groups of physicists started an R&D effort to study the capabilities of this detector for their respective fields, mainly nuclear and high energy physics. This resulted in the successful realisation of prototypes and several laboratory

tests were performed to investigate the properties of the detector:

- radiation hardness;
- high flux performance;
- switch-on behaviour;
- micro-discharges;
- energy resolution;
- position resolution;
- particle detection efficiency;
- variations of the geometry;
- gas, geometry and readout optimisation for experiments.

All these issues should be very well under control before the detector can be used as a tool. From the beginning, all groups studying the MSGC were involved in most of these items. Later on each group developed its own specialisation. The NIKHEF group specialised on position resolution, geometry and detector optimisation, computer modelling and the problem of readout. A group in Manchester studied the problem of micro-discharges in detail and performed extensive readout simulations [40]. The CERN group achieved important results with their studies of radiation hardness, high flux operation, and switch-on behaviour. The Oed group focused on various aspects of photon detection. The Pisa group looked into alternative designs, and geometrical solutions for two-dimensional readout. The CERN and Pisa groups developed computer programs to calculate electric field configurations in complex MSGC geometries (with conducting surfaces, etc.). Most of the laboratories working on MSGC R&D now joined the RD28 collaboration, established in 1991. The member institutes of this collaboration focus on problems associated with the application of MSGCs in LHC experiments. In the following sections a brief overview of the R&D results is given; research is going on more intensively than ever at the moment of writing, so this overview is one of the momentary situation.

## 3.2 Radiation hardness

The radiation hardness of a detector is its quality to withstand a long-term irradiation without a change of performance. Radiation can change the detector behaviour because for instance it ionises all materials involved, creating new molecules that may attach to the electrodes and/or the substrate surface. Radiation damage has been studied extensively for wire chambers and many other types of detectors, and most of the processes involved are well known although not always understood at a quantitative level. An extensive overview and evaluation of wire chamber aging is given by Kadyk [41]. The most important conditions for a wire chamber to be radiation hard are:

- the gas mixture used should contain very little impurities (such as water vapour and oxygen);
- the materials that form the detector should not contain evaporating components;
- components of the gas mixture and the detector itself should be very carefully chosen; some materials are found to be worsening the detector performance in general (like PVC), others can be harmful in certain combinations (like DME and Teflon).

For the problem of radiation hardness we can profit from over 20 years of experience with MWPCs, because many aspects of radiation hardness are similar in both detectors. Only, the electric field close to the anode strips is a bit higher than close to anode wires, which can lead to a dissociation of gas molecules into free radicals. The MSGC substrate can also cause additional problems: deposits, a change of resistance, etc., can cause the detector performance to change as a function of time under radiation. Many studies of radiation hardness focus on the properties of the substrate. It turns out that an MSGC with a highly resistive substrate deteriorates fast [19]. For the application in LHC experiments, one can use substrates with either a bulk resistivity less than  $10^{12} \Omega\text{cm}$  or a surface resistivity around  $10^{13}\text{--}10^{14} \Omega/\square$ , which is much less resistive than normal insulators like glass.<sup>1</sup> The bulk resistivity of an insulator can be decreased by ion implantation. The surface resistivity of an insulating material can be lowered for instance by the evaporation of a thin layer of a weakly conducting material on top of the microstrip substrate (e.g. a few nm of Germanium, as presented in [42]).

A systematic study of MSGC aging is now performed by the CERN group [43].

### 3.3 High flux performance and switch-on behaviour

The substrate also plays an important role in the performance of the MSGC at high particle fluxes. With a wire chamber, the maximum flux is determined by the occupancy of each sense wire, i.e. we should still be able to tag individual particles so the wires should not detect a signal continuously. At high rates the detector operation is changed by the large amount of free ions drifting around in the gas volume, influencing the electric field and recombining with drifting electrons liberated by a new particle.

The MSGC substrate can add to the ion pollution problem by attachment. The ions that are liberated in the gas amplification process will be pulled towards the cathode strips, and during their drift towards these strips they can bump into the substrate, even when all field lines from the anodes run towards a cathodic conductor (because transverse diffusion takes the ions off their field line path). When a fraction of these ions will actually adhere to the substrate, between the anode and the cathode strip, they may stay there for a relatively long period. So the substrate surface may be charged up, influencing the electric field in the detector and therefore the gas amplification process. This effect is very significant in MSGCs: it is found that when the detector is switched on, it has an initial gas amplification that

---

<sup>1</sup>The specific resistivity of a surface has dimension  $\Omega$ , but is often denoted  $\Omega/\square$  because the specific resistivity is the resistivity of a square sample of any size of this material when measured between two opposing edges.

either drops or rises as a function of time, and only after a time period of 10–30 minutes the gain stabilises. This switch-on effect is reported in many papers, see eg. [44]. The resulting equilibrium depends strongly on the particle flux that the detector is exposed to.

### 3.4 Micro-discharges

Like in MWPCs, the high voltage applied to the various electrodes can cause sudden discharges in the gas. It has been found that the occurrence of discharges can be lowered considerably by using a quench gas in the gas mixture (i.e. a gas which absorbs ultraviolet light in a wide spectral range), such as hydrocarbons. The possibly damaging effect of these micro-discharges can be reduced by electronic quenching (when the strips are connected to voltage supplies through a high impedance, the maximum energy liberated in the discharge is the stored capacitive energy in the strips). Snow et al. have studied the specific problem of discharges occurring at the ends of the cathode strips [45], and an electronic protection circuit is presented in [36].

### 3.5 Energy and position resolution and efficiency

The energy resolution of the detector is determined by the statistical fluctuations in the gas amplification process (when the detector is operated in the proportional range). Various instrumental effects can add to the measured energy resolution: a different gas amplification factor on each strip, pedestal drift, electronics noise etc. Optimisation of the energy resolution therefore involves a very good control over the experimental setup.

The position resolution of the detector depends very much on the particles one studies: in a typical MSGC the conversion location of 6 keV photons can be determined much more accurately than that of a crossing minimum ionising particle, because the number of electrons liberated by the photon is much larger.<sup>2</sup> The position resolution of the MSGC for minimum ionising particles is discussed in the next chapter. It cannot be separated from the detection efficiency because when a higher signal threshold is required to distinguish particles from noise, we also select events with higher signal and these are events with higher primary statistics. A better resolution can generally be obtained at the expense of detection efficiency.

### 3.6 Second coordinate readout

Many groups investigated the possibility of the localisation of the signal in the second coordinate by picking up the signal at the back plane [46]. The main problem with this readout of the second coordinate is that the signal is much weaker at the back side than at the strips. The smaller the distance between the back electrode and the strips, the larger the pick-up signal. For this reason complex multi-layer MSGCs are proposed and built by some groups,

---

<sup>2</sup>A 'photon conversion' in this energy range is an interaction between the photon and matter, which results in ionisations.

where the back plane is only a few microns away from the strip pattern. The disadvantage of these detectors is their technical complexity: they are preferably made on a monocrystalline Si substrate, and more than one mask is needed in the manufacturing process, which increases the cost of mass production of these detectors. The cheapest MSGC can be made with a one-mask process, and starting from an ordinary carrier like glass or alumina (amorphous  $\text{Al}_2\text{O}_3$ ).

### 3.7 Variations of the geometry

The MSGC-theme got many variations over the years. Researchers have tried to improve the concept, by making geometrical changes. Two groups of high-energy physicists created a microstrip pattern on various types of plastic foils (Kapton, Tedlar) to see if this could be operational as a normal MSGC [47], with the advantage of a very thin substrate (and therefore little interaction with the particle). Results have so far not been good enough to see the foil substrate MSGC as a candidate detector for future experiments: the switch-on effect is very large in foil MSGCs, with a drop of the gas amplification of more than a factor 2. The energy resolution of these detectors was rather bad (the  $^{55}\text{Fe}$  peak showed a width around 20% FWHM), which is assigned to the fact that the strip pattern is coarser than on glass (because of the roughness of the plastic foils). Others have circumvented the complex step of photolithography creating the microstrip pattern on a Printed Circuit Board (PCB). This technique is cheaper but coarser; one can produce large-area devices with a relatively large anode pitch (down to  $\sim 0.5$  mm) [48].

As the event topology of many particle physics experiments is azimuthally ( $\phi$ -) symmetric, most detectors in these experiments share that symmetry. For that reason it is interesting to think of an MSGC with a substrate and cathode plane bent along the surface of concentric cylinders. A prototype of such a detector was built in 1992 [49] and one has proposed this geometry for a vertex detector in CLEO. A simpler geometry, with a planar substrate but nonparallel strips, was successfully constructed at NIKHEF in 1993. This substrate carries strips that point towards a common origin outside the substrate, yielding a  $\phi$ -symmetric fan out pattern. This geometry is proposed for the forward MSGCs in ATLAS and CMS, as will be explained in chapter 5.

The detector is also proposed as the sensitive plane of a TPC (Time Projection Chamber) [50, 51]. This essentially means that the drift plane is very far away from the strip plane and the position of a crossing particle (moving parallel to the strip plane) is derived from the arrival time of its signal, rather than from the charge distribution over the anodes.

For experiments with a low flux, the MSGC setup with one preamplifier per anode is not very effective, because the numerous amplifiers register only few pulses per time interval. The optimum use of this type of electronics is when the preamplifier occupancy is of order 0.1–1%. The MSGC can be used for low-flux experiments when more than one anode is read out by a preamplifier. Two schemes based on this philosophy are shown in figure 3.1. The left figure was shown in the original patent request from A. Oed [52]. The difference in arrival time of the pulses on either preamplifier contains position information. The scheme

in the right figure is used for tracking highly energetic heavy ions in the fragment separator

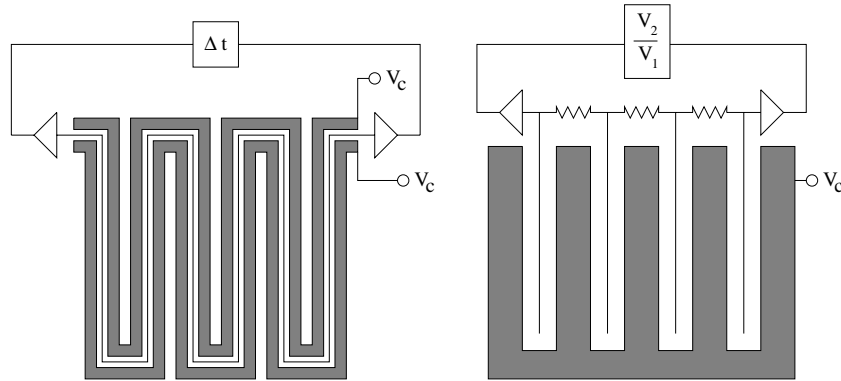


Figure 3.1: Two variations of an MSGC with more than one anode per electronics channel.

at GSI [53]. Particles are localised by comparing the signal strength as registered by the two preamplifiers. The position resolution of the latter detector is a few mm (depending on the operating conditions), which is sufficient for the purpose of the experiment.

### 3.8 Readout

Consider again an MSGC that is read out at the anode strips. The signal on the anodes caused by relativistic particles is only very small and needs amplification with a dedicated low-noise amplifier. For most purposes, there will be one (pre)amplifier per anode strip. The signal can in principle be a voltage decrease (when the input impedance of the preamplifier is high), but for such fast signals a better signal-to-noise ratio is achieved with a current preamplifier (with a low input impedance).

For the readout of the MSGC detectors, different preamplifiers were used by different groups. Hybrid preamplifiers are well suited for small-scale prototyping, so these were often used in the early days of MSGC testing. Nowadays most groups have switched to integrated circuit preamplifiers, because they are cheaper per channel. Mostly, preamplifiers are used that were originally developed for silicon strip detectors: for instance, the MX5 chip developed for vertex detector readout at LEP experiments [54], or the APC chip for H1 at HERA [55]. Some specifications of these preamplifiers are given in table 3.1, giving an impression of the sensitivity and noise level needed to effectively use the MSGC for particle tracking. In charge-sensitive preamplifiers, the noise is most commonly expressed in the Equivalent Noise Charge (E.N.C.). A noise figure of 2000 electrons E.N.C. means that the RMS value of the noise at the preamplifier output equals the signal at the output when a test charge of 2000 electrons is injected at the input.

When the MSGC is applied in a large experiment it will be worthwhile to design a new preamplifier specifically for this detector at this experiment, so that the detector is optimally read out. For the application of MSGCs in LHC experiments, the specific design criteria are

	MX5	APC	Fastplex
Clock frequency (MHz)	$\leq 5$	10	40
Sensitivity ( $\mu\text{V}/\text{ke}^-$ )	500	*	2000
Noise level (electrons E.N.C.)	$350+18/\text{pF}$	$675+28/\text{pF}$	$<2000$
Dissipated power per channel (mW)	0.6–2.0	0.3	1

Table 3.1: Technical specifications of three preamplifiers used for the readout of the MSGC anodes. An asterisk indicates that the entity is not quoted in the reference.

that it should operate at 40 MHz clock frequency (which is the bunch crossing frequency of the machine), it should be fast enough to cope with a 1% hit probability on each channel, and it should be radiation hard. In a joint project started by NIKHEF and CERN groups, an ASIC (Application Specific Integrated Circuit) is now under development for this purpose under the name Fastplex. A tentative design specification for this preamplifier is also given in the table. (The noise specification refers to an input capacitance of around 10 pF.) Note that the target noise level and power dissipation of the Fastplex are higher than those of the MX5 and APC. This is inevitable due to the requirement of a higher clock frequency. These design criteria follow from dedicated Monte Carlo simulations that generate the MSGC signal as an input and analyse the output of the simulated preamplifier (presented in section 4.5). Apart from the preamplifier section, this ASIC will contain a discriminator, a pipeline to buffer the information, and some logic to reduce the data flow from the Fastplex to the data storage units. Of the order of 100,000 of these chips will be needed to read out the MSGC detectors in ATLAS!

## 3.9 Detector optimisation for high-flux experiments

### 3.9.1 Geometry limitations

The geometry of the MSGC is determined essentially by four numbers: the dimensions of the substrate surface, the size of the gas gap, and the anode pitch. The substrate size is chosen as large as feasible in most cases. This size is determined by the tools used to fabricate the pattern on the substrate. These tools are 'borrowed' from silicon wafer processing industry, so they can handle sizes up to 4"×4" ( $\sim 10 \times 10 \text{ cm}^2$ ) in general. Developing new tools for larger detectors will involve a major investment.

The anode pitch is a parameter that determines the granularity, and therefore both the position accuracy and the number of individual read out channels. It has been shown that MSGCs with a pitch ranging from 100  $\mu\text{m}$  to 1 mm function well [56]. Below 100  $\mu\text{m}$ , it becomes increasingly difficult to design a microstrip pattern that can be operated with a high gas amplification factor. One requires cathode strips much wider than the anode strips, anodes wider than 3  $\mu\text{m}$  (because thinner anodes are difficult to produce with high yield and become too resistive), and a reasonable gap between the strips to be able to maintain a high

voltage difference between the two.

The gas gap determines position resolution, signal speed and efficiency. It will be different in different experiments, because in some experiments speed prevails over position resolution, while in others one may aim for a good position resolution up to large angles (which requires a small gas gap). The influence of pitch, gas gap width and angle of incidence on the resolution is discussed in the next chapter.

### 3.9.2 Gas mixtures for the MSGC

The gas mixture in each gas filled particle detector used in a high energy physics experiment has been subject to intensive optimisation. Because the mixture is both the active medium and acts as a signal transport and amplification medium, it should fulfill many requirements at the same time which makes an optimum gas choice hard. The final choice will depend strongly on the demands following from the specific experimental conditions. In the case of MSGCs these conditions are known. The detector is most suitable for precision tracking in a high flux environment, and therefore gas mixtures used in this detector should have the following characteristics:

- The primary ionisation density of the gas mixture should be very high to reach full efficiency in a thin layer of gas.
- The electron drift velocity  $v_D$  should be very high to achieve a large signal speed. (In a high-flux environment this is needed to keep the detector occupancy low.)
- The maximum gas amplification factor should be at least 2000 to match the signal height to the noise level of state-of-the-art electronics.
- The gas mixture should not cause a fast detector aging.
- When the detector is used in a magnetic field, the gas mixture should have a low Lorentz angle, which can be obtained when the electric field strength in the drift region is high.

And, of course, the more general restrictions for a drift gas apply: it should not contain electronegative components, it should not be explosive and preferably it should work around 20° C. The requirements of high drift velocity combined with a low Lorentz angle ask for a low mobility and a high electric field (see equations 2.5 and 2.7). Together with the other criteria we can preselect the following gases of interest: Xe, CO<sub>2</sub>, CF<sub>4</sub> and DME (dimethyl ether, (CH<sub>3</sub>)<sub>2</sub>O). Isobutane (*i*C<sub>4</sub>H<sub>10</sub>) can also be regarded as a candidate, but it has a rather low drift velocity even at high fields.

Dimethyl ether and CO<sub>2</sub> reach a high electron drift velocity only at high electric fields (around 10 kV/cm); CF<sub>4</sub> and isobutane reach a maximum drift velocity around 2–4 kV/cm. Hence, mixtures of DME and CO<sub>2</sub> will perform well at high electric field strength (7–10 kV/cm), while mixtures of CF<sub>4</sub> and isobutane have an optimum drift velocity at lower fields; drifting electrons tend to attach to CF<sub>4</sub> molecules when high drift voltages are applied. For Xe, no information is available on the electron drift velocity in electric fields above

3 kV/cm, but the measurements presented in the next subsection indicate a rather high drift velocity over a large range of the electric field strength (2–8 kV/cm). Specific measurements of the electron drift velocity and the performance of some qualified gas mixtures in the MSGC are presented in the following reprint.

### **3.9.3 Reprint: tests of the performance of different gas mixtures in microstrip gas counters**



















## Chapter 4

# Monte Carlo simulations of the MSGC performance

Sections 2 and 3 of this chapter are based on the following articles:

J. SCHMITZ, *Results on Monte Carlo simulations of a Microstrip Gas Counter*, Nucl. Instr. and Meth. A 323 (1992) 638;

J. SCHMITZ, *Monte Carlo simulations of the Microstrip Gas Counter*, Proc. of the international conference on Monte Carlo simulation in High Energy and Nuclear Physics (MC93), Tallahassee, World Scientific, eds. P. Dragovitsch *et al.*, page 293.

Early results from these simulations were presented in

M. GEIJSBERTS, F. G. HARTJES, J. G. PANNEKOEK, J. SCHMITZ AND F. UDO, *The resolution optimization of the microstrip gas counter*, Proc. of the LP-HEP 91 conference Vol. 1 page 239, Geneva 1991.

### 4.1 Monte Carlo simulations

Many processes that determine the functioning of the MSGC are of a statistical nature: the ionisation of gas molecules, the diffusion of the free electrons in the gas, the gas amplification, etc. These statistical processes can be measured and understood; however, even if all probability functions involved in the detector performance are known, it is often difficult or impossible to find analytical expressions for the parameters that determine the detector quality, such as efficiency and energy resolution. Numerical integration is an interesting alternative, but often slow. When many probability distributions must be taken into account simultaneously in a physical process of interest, a good, and often the only alternative to the analytical approach is the so-called Monte Carlo simulation. This is a simulation (on a computer) of the physical process: from a given initial condition, all processes are evaluated, and whenever a statistical distribution is involved in a process, a random choice is made according to this distribution. This is done many times to determine the average behaviour and the size of the fluctuations around the average.

Monte Carlo simulations can be very powerful tools to help understand and optimise

particle detectors. In modern high energy physics experiments these simulations are indispensable at all stages, from the initial design of the experimental setup until the estimate of systematic errors in the final results from the experiment. In the case of detector optimisation, simulations are done because running a program under many different conditions is easier than building a new prototype for each try. Caution should be exercised in relying on the results of a Monte Carlo simulation, because the predictions are always made from a model, which may be limited in validity. Therefore predictions of the simulation should always be checked by performing dedicated experiments, and the model may be tested on other available measurements.

In the next section, a Monte Carlo simulation of the MSGC is described. This simulation describes the ionisation process, electron transport, and signal development. It is used to relate beam test measurements to the model of the detector behaviour. The model was tuned on data taken in a 4 GeV  $\pi$  beam at CERN (presented in section 3.9.3), and checked later on data taken with a cosmic ray setup (as described in section 4.4). The Monte Carlo simulation was used to estimate the performance of the MSGC when read out with a high-speed front end preamplifier. This simulation study is presented in section 4.5. Another application is the simulation of a full MSGC tracker in the ATLAS experiment for design optimisation [57].

## 4.2 Simulation of the MSGC

### 4.2.1 Introduction

In fact the recipe to set up a Monte Carlo simulation of the MSGC has been given in chapter 2. A program was written according to that model of the detector functionality.<sup>1</sup> The core of this program is a Monte Carlo simulation of the initial ionisation processes in the gas volume, the drift and diffusion of the electrons, and the gas amplification process. This simulation is not complete because many aspects of the current model of the MSGC detector behaviour are omitted. The simulation is complete in the modelling of the liberation and transport of charge in the gas volume. What should be added to achieve a simulation with the required accuracy, depends on the goals of the user. For instance, when the performance of the detector in a very high rate environment is studied, the abundance of positive ions from a former particle crossing may influence the next particle detection. In the presented simulation however, subsequent events are not correlated. The general purpose 'test beam' simulation used for comparison of beam data with the model is publicly available since June 1992 [59].

### 4.2.2 Description of the MSGC model

The MSGC is simulated in two dimensions (as in figure 4.1), labeled  $x$  (the direction parallel to the substrate, perpendicular to the strip orientation) and  $y$  (the direction perpendicular to the substrate). The third coordinate,  $z$ , runs along the strips. This latter coordinate has no relevance in the ideal MSGC, with infinitely long electrodes; it can become important when the charged particle has a velocity component in this direction, when saturation effects occur

---

<sup>1</sup>A similar program was later written by M. Esten [58].

in the gas amplification process, and at the ends of the strips. However, the two-dimensional model is good enough for our purposes.

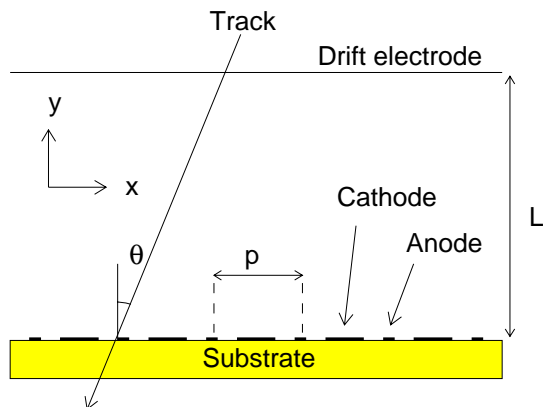


Figure 4.1: Geometry of the MSGC.

### Ionisation

A minimum ionising particle traversing the gas gap causes a number of primary ionisations  $N_p$  which follows a Poisson distribution. Each primary electron ( $\delta$ -electron) can in turn ionise some more molecules, so the free charge is generated in clusters. The clusters are not generated exactly along the track. The  $\delta$ -electrons travel a distance  $R_p$  from the ionising track during the secondary ionisation process. The practical range of electrons,  $R_p$ , depends on the initial energy  $E$  of the  $\delta$ -electron, and is modelled with the empirical formula [60]

$$R_p = 0.412E^{1.265-0.0954\ln E}, \quad (4.1)$$

where  $R_p$  is given in  $\text{g}/\text{cm}^2$  and  $E$  in  $\text{MeV}$ .<sup>2</sup> Eq. (4.1) is obtained from a fit over the energy range  $E = 10 \text{ keV} - 2.5 \text{ MeV}$ . The use of this equation in the simulation of the MSGC implies an extrapolation in energy down to 1 keV, which is a worst-case approximation [62]. The  $\delta$ -electron is emitted randomly in the plane perpendicular to the direction of the incoming relativistic particle. In the simulation the electron is assumed to travel over a distance  $R_p$  along a straight line in this plane. The secondary ionisation is distributed homogeneously along the  $\delta$ -electron path. (It is found that in most of the practical cases one can assume  $R_p = 0$  because the occurrence of macroscopic practical ranges is very low.)

### Drift and diffusion

From their starting point, the liberated electrons will drift towards the strip plane, while they undergo a displacement in  $x$  and  $z$  because of transverse diffusion. Transverse diffusion in

<sup>2</sup>The practical range, or extrapolated range, has a non-trivial definition (see eg. [60, 61]) but it is close to the maximum range of electrons in a given material.

$x$  is important in the model because it is responsible for the spread of the signal over more than one anode strip. (Longitudinal diffusion does not have any significant effect so it is not implemented.) When the electrons reach the quadrupole field (at a height above the strip plane roughly equal to the pitch of the strip pattern) they will be focused towards one of the anodes. This electrostatic focusing makes the probability very low that a drifting electron will diffuse to an adjacent anode. Therefore the diffusion is switched off in this region.

### Gas amplification

The gas amplification process is parametrised following equations 2.9 and 2.10. For a complete description of the MSGC, the Polya parameter  $m$  (which relates to the variation in gas gain as  $\sigma^2 \propto m^{-1}$ ) should be tuned to experimental data. The amount of the gas gain fluctuations is known for several gas mixtures containing argon, from the measurements of the pulse height spectra of  $^{55}\text{Fe}$ . These indicate  $\sigma \approx 0.7$  which yields  $m \approx 2$ . Measuring the pulse height spectrum of  $^{55}\text{Fe}$  in other gas mixtures will not suffice to determine the gain fluctuations in these mixtures: one needs to know the number of electrons liberated after the  $\gamma$  conversion, and the variation in this number (expressed in the Fano factor [63]) to interpret the spectrum. Dedicated measurements to determine the gain fluctuations in the MSGC have not been reported so far, so by lack of experimental data we take  $m = \frac{3}{2}$ , the canonical (Curran) value for wire chambers.

### Simplifications

Electronic noise is described as uncorrelated. All strips have identical performance. The code does not include a description of magnetic field effects and the electric field is perfect (no edge effects etc.). And finally, the electrons created in the quadrupole field near the strips are treated in the same way as those liberated in the drift field.

### 4.2.3 Tuning the Monte Carlo to experimental data

The model described in the previous section contains a large number of free parameters. These are fixed to values from the literature if possible, and otherwise (in the case of  $\sigma_T$  and the cluster size distribution) tuned to data collected during the beam test reported in section 3.9.3. The data taken with the gas mixture DME/CO<sub>2</sub> 60/40 were optimal for tuning of the model because they included a fine angular scan around perpendicular incidence. The gas gap  $L$  was  $(2.7 \pm 0.1)$  mm for two detectors, and  $(2.9 \pm 0.1)$  mm for the other two.

All parameters in the Monte Carlo simulation are listed in table 4.1. The gain factor, the cluster size distribution and the transverse diffusion coefficient needed tuning to the data because no other information was available. (This problem can be avoided with the latter two by using a more common drift gas mixture such as P10.)

The signal was measured in ADC counts, and the average signal of one drifting electron was around 80 ADC counts. The chamber was operated in proportional mode (gas gain around 5000). The noise had a  $\sigma$  of 40 ADC counts. A negative crosstalk of 5% occurred between the anodes (because cathode strips were interconnected). Instead of correcting for

Parameter	symbol	value	determination
Pitch	$p$	200 $\mu\text{m}$	Defined
Gas gap width	$L$	2.7-2.9 mm	Defined
Primary ionisation	$n_P$	4.66 $\text{cm}^{-1}$	[22]
Transverse diffusion	$\sigma_T$	49 $\mu\text{m}/\sqrt{\text{mm}}$	Tuning
Amplification factor	$G$	80 ADC counts/ $e^-$	Tuning
Crosstalk		5%	Data analysis
Cluster size distr.	$w(n)$	$w(1) = 0.70$	Tuning
		$w(2) = 0.20$	Tuning
		$w(n > 2) \propto 1/n^2$	[25]
Polya parameter	$m$	1.5	[30]
$\delta$ -electron range	$R_P$	see eq. 4.1	[60]

Table 4.1: The free parameters in the Monte Carlo simulation of the MSGC, with their values and origin, for the gas mixture DME/CO<sub>2</sub> 60/40. (The Polya parameter is adopted from MWPC literature.)

this effect in the data, we put it in the simulation, because there was no proper way we could correct the data for events where one of the strip signals caused an ADC overflow.

To simulate the ionisation process, one needs the statistical distribution of the number of electrons in a cluster. For DME this distribution is not known; data for CO<sub>2</sub> are given in [25]. A simple approximation is made for the mixture DME/CO<sub>2</sub> 60/40. The probability to find  $n$  electrons in a cluster is  $w(n)$ . According to the Rutherford theory,  $w(n)$  is proportional to  $1/n^2$ , apart from deviations at small  $n$  that depend on the electronic structure of the gas molecules. The maximum allowed energy transfer in the collision determines a cut-off at high  $n$ . From experiments it is known that  $w(1)$  is around 0.70 for most gases. We set  $w(n) \propto 1/n^2$  for  $3 \leq n \leq 1000$ . The parameters  $w(1)$  and  $w(2)$  were tuned by comparing the Landau distributions of simulation and data.

The Landau distributions matched best with  $w(1) = 0.70$  and  $w(2) = 0.20$ , which case is shown in figure 4.2. This figure shows the signal spectrum for the strip with the highest signal. It turns out that the optimum values of  $w(1)$  and  $w(2)$  are very sensitive to the exact value of the gas gap width  $L$ . To establish the actual cluster size distribution we need more accurate information.

The transverse diffusion of the electrons in the drift region can be tuned by comparing the average number of firing strips, in the data and the Monte Carlo. A more thorough comparison between MC and data can be made by looking at the distribution of the RMS of the charge cluster in both cases. If only one strip has a signal above threshold, the RMS of the charge distribution is 0  $\mu\text{m}$ . If two adjacent strips fire, the RMS is between 0 and 100  $\mu\text{m}$ , depending on the relative pulse height of the strip signals. If three strips have a signal above threshold, the RMS is between 0 and 200  $\mu\text{m}$ .

The distribution of the RMS of clusters is shown in figure 4.3 for data and Monte Carlo,

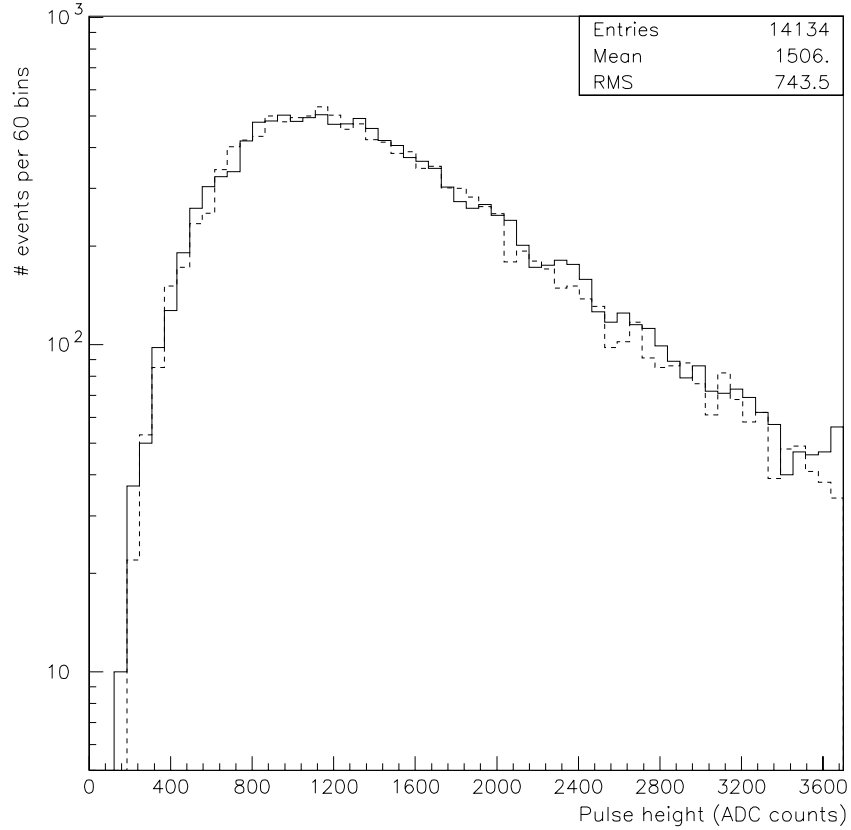


Figure 4.2: Measured signal from a minimum ionising particle on one strip (solid line), and the same entity as simulated with the Monte Carlo program (dashed line).

after tuning the diffusion constant. We found  $\sigma_T = (49 \pm 4) \mu\text{m}/\sqrt{\text{mm}}$ . The gap between  $\text{RMS} = 0$  and  $38 \mu\text{m}$  is caused by the fact that signals are always between threshold and ADC-overflow. The two histograms compare very well, only the number of events with an  $\text{RMS} > 100 \mu\text{m}$  is too low in the simulation (the simulation predicts 2 events, there are 17 events in the data with an  $\text{RMS} > 100 \mu\text{m}$ ). These events have a moderate total signal, which leads us to the conclusion that they are not caused by highly energetic  $\delta$ -electrons.

Two explanations of the occurrence of these events can be brought forward. The events can be explained as double-tracks with a distance in  $x$  around  $250 \mu\text{m}$ , which are not removed by a cut on separate clusters but do give rise to a wide cluster. The discrepancy is solved if one assumes that 2% of the triggers of the beam test contained two tracks close together. Another explanation is that secondaries from a particle interaction in the substrate enter the gas volume. One can distinguish between these two effects because the double tracks should be seen in the same manner in consecutive layers, while the shower products would manifest themselves in one layer only. Unfortunately the statistics in this data sample were too low to determine the origin of these events.

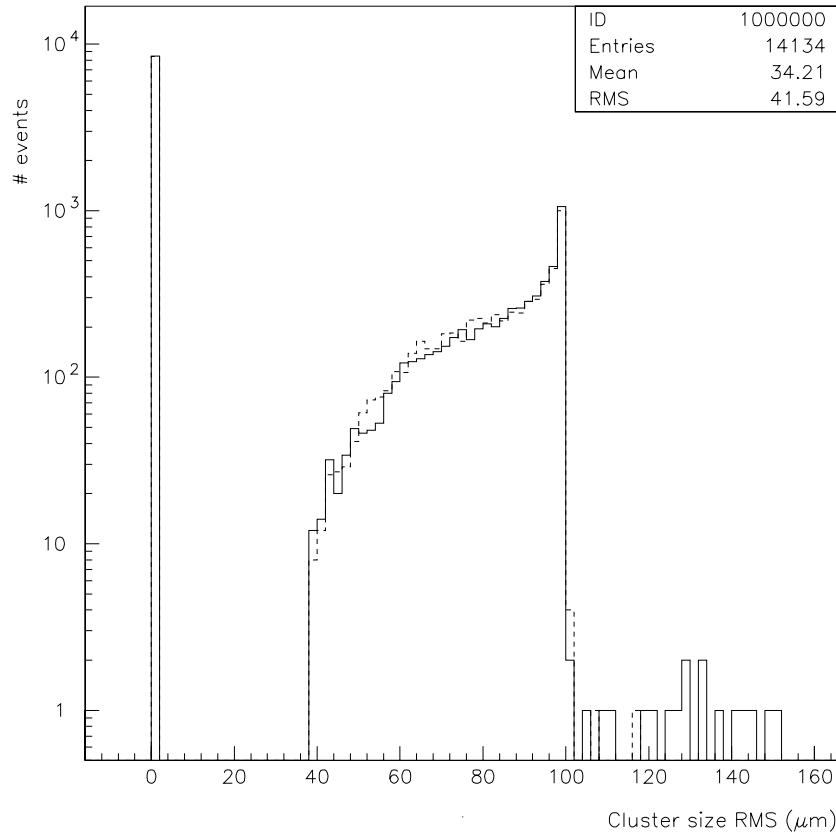


Figure 4.3: The RMS of signal clusters arising from a crossing minimum ionising particle, for data (solid histogram) and Monte Carlo (dashed histogram).

## 4.3 The position resolution of the MSGC

### 4.3.1 Determination of the position of a track

The liberated electrons drift towards the detector substrate while they undergo a transverse diffusion. The consequence is that the signal spreads out over more than one anode strip. When the profile of the signal is measured, this allows an accurate determination of the track position at crossing time. A very good position determination can be achieved by calculating the centre of gravity of the signals on the anode strips, and only a small improvement can be made by correcting for systematic effects (this improvement becomes important when the electron cloud is much smaller than the anode pitch). Only signals above a certain threshold are taken into account.

It has been suggested that a somewhat better position resolution can be achieved when the cathodes are read out instead of the anodes. The idea behind this is that when a particle crosses the anode on the left side, the liberated electrons will create a cascade at the left side of the anode strip; this cannot be distinguished on the anodes, but the left cathode should have

a larger signal than the right cathode in this case. This is not verified by any measurement and the hypothesis seems rather weak when we consider the electric field in the detector. The field line plot of figure 2.3 shows that the paths of electrons from left and right side almost overlap over a length of  $80 \mu\text{m}$ . This implies that, when we take into account the transverse diffusion, electrons from the left and right side will be mixed, and left/right information will be lost. Only the electrons liberated in the quadrupole region could contribute to a signal difference in the above manner. The effect might therefore be significant when the quadrupole region is large compared to the drift region.

### 4.3.2 Contributions to the measurement error of the position

Assuming that the electronic readout of the detector is perfect, the position resolution of the MSGC is determined basically by five effects:

- ionisation density of the drift gas;
- range of  $\delta$ -electrons;
- transverse diffusion;
- undersampling of the ionisation cloud;
- gain fluctuations.

#### Ionisation density of the drift gas

The ionisation density enters as a determining factor in the statistical contributions to the position resolution and should be as high as possible. In a gaseous detector one mostly uses drift gases with a high ionisation density (such as the heavy noble gases, higher alkanes and DME).

#### The contribution from $\delta$ -electrons

For detectors like the MSGC, where the path length of a particle in the drift gas is typically a few mm, the occurrence of long-range  $\delta$ -electrons is rather low. In pure Argon, the probability that a liberated electron is a  $\delta$ -electron with a practical range of  $> 100 \mu\text{m}$  is less than 0.2% [23].  $\delta$ -electrons cause non-Gaussian tails to the distribution of residuals. In an MSGC with a 2 mm gas gap, about 1–2% of the events are found outside  $\pm 3\sigma$  (Gaussian prediction: 0.3%). When a cut is applied on  $\pm 3\sigma$  the remaining contribution to the position resolution from occurrence of  $\delta$ -electrons is around 3–6  $\mu\text{m}$ . For larger gas gaps,  $\delta$ -electrons add more significantly to the position resolution [64].

A cut on  $\pm 3\sigma$  is very effective to get rid of events with a spoiled position measurement (not only in the case of a long-range  $\delta$ -electron). However, one can only apply this cut when position information is available from external sources. Instead of cutting events on  $\pm 3\sigma$  the heavy ionisations caused by long-range  $\delta$ -electrons can also be identified by their

anomalous pulse height. This method is less effective though, because also some 'good' events are rejected.

### Transversal diffusion

The contribution of the transverse diffusion to the position resolution is (to first order) geometry-independent, and depends only on the drift gas characteristics. This dependence can be intuitively seen as follows. Consider perpendicularly incident particles in the MSGC. The position of the track is determined from the centre of gravity of the ionisation cloud. An electron, liberated along the track of the incoming particle at a height  $h$  above the anode plane, will diffuse during its drift towards the anode plane and end up at a distance  $x$  from the average given by the Gaussian distribution

$$P(x, h) = \frac{1}{\sigma_T \sqrt{\pi h}} e^{-x^2/\sigma_T^2 h}, \quad (4.2)$$

where  $\sigma_T$  is defined as in equation 2.3. If we consider a single electron released along a track,  $h$  is not known. The distribution of single electrons coming from ionisation of a crossing particle can be found by integrating eq. 4.2 over  $h$ , with  $h$  running from 0 to  $L$ . The resulting distribution shows a Gausslike curve with a sharp peak and a long tail (figure 4.4 shows its shape as generated by a Monte Carlo simulation). The RMS of this distribution is approximately

$$\Delta x \approx \frac{1}{2} \sigma_T \sqrt{L}. \quad (4.3)$$

This value is the same as the RMS of the position distribution of electrons liberated at  $h = \frac{1}{2}L$ . The dependence on  $L$  cancels if we consider  $N$  electrons distributed homogeneously along the track of the incoming particle. With the substitution  $N \approx n_T L$  the RMS of the distribution of these  $N$  electrons on the anode plane can be written as

$$\Delta x_N \approx \frac{\Delta x}{\sqrt{N}} \approx \frac{\sigma_T}{2\sqrt{n_T}}. \quad (4.4)$$

Essentially, this means that if the gas gap is increased, the cloud width becomes larger, but the improving electron statistics causes the spread in centre of gravity to remain the same. In practice,  $N$  varies from event to event and the electrons are not distributed homogeneously, but the replacement of  $N$  by  $n_T \times L$  holds when  $N$  is large. If  $N$  is small ( $< 100$ ),  $\Delta x_N$  is larger than eq. 4.4 would suggest.

Equation 4.4 gives us the approximate contribution from the transverse diffusion to the position resolution. Note that this term only depends on drift gas properties. The value of  $\Delta x_N$  amounts to  $7 \mu\text{m}$  for Xe/DME/CO<sub>2</sub> and DME/CO<sub>2</sub>, assuming  $\sigma_T = 62$  and  $50 \mu\text{m}/\sqrt{\text{mm}}$  respectively (determined by fitting the Monte Carlo results to the charge distribution data measured in 1991). It is higher for most other gas mixtures because both  $n_T$  is relatively high and  $\sigma_T$  is relatively low for Xe/DME/CO<sub>2</sub> and DME/CO<sub>2</sub>.

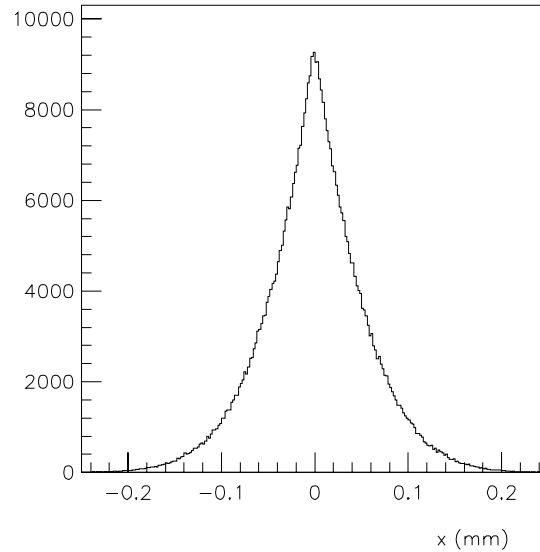


Figure 4.4: *Distribution of electrons along the  $x$ -direction after drift and diffusion, for a 5 mm gas gap and  $\sigma_T = 50 \mu\text{m}/\sqrt{\text{mm}}$ .*

### Undersampling

Undersampling of the electron cloud takes place when the pitch  $p$  of the anode structure is large compared to the size of the electron cloud. For  $p \ll \Delta x$  (see eq. 4.3), the cloud is efficiently sampled. When  $p \approx \Delta x$ , systematic deviations occur in the measured position of the track. In the case that  $p \gg \Delta x$ , generally only one anode gives a signal when a particle crosses, and the position resolution is given by  $p/\sqrt{12}$ .

### Gain fluctuations

Fluctuations in the gas amplification confuse the determination of the centre of gravity of the electron cloud, and therefore deteriorate the position resolution of an MSGC. If undersampling of the electron cloud can be avoided, the diffusion error and gain fluctuations are in practice the most important contributions to the position resolution.

There seem to be two ways to achieve the optimum resolution in an MSGC: a thin gap ( $L$  of the order of 2 mm) detector must have a very low pitch and minor gain fluctuations. In a large gap ( $L > 1$  cm) detector the requirement of small gain fluctuations can be relaxed because the number of electrons is larger. The pitch can be larger because the electron cloud is broader. The occurrence of  $\delta$ -electrons increases with  $L$  and this will add to the position measurement error.

Probably the best way to suppress the problems associated with low electron statistics is

to improve the ionisation density along the  $y$  direction either by pressurising the drift gas or by tilting the detector. Pressurising the drift gas has the additional advantage that the range of  $\delta$ -electrons becomes smaller, but this adds to the technical complexity of the experimental setup.

### 4.3.3 Optimisation of the MSGC resolution

In the beam test of 1991, the clouds spread out over only 1.5 strips on average, so undersampling of the electron cloud contributes to the position resolution. A better position resolution can therefore be achieved by increasing the gas gap or reducing the pitch. Monte Carlo predictions of the position resolution for varying pitch and gas gap are shown in fig. 4.5. (The track position was always calculated with the centre of gravity method.) To remove the tails in the residual distribution, a cut was set on  $\pm 100 \mu\text{m}$  ( $\pm 200 \mu\text{m}$  for those geometries where the resolution was larger than  $40 \mu\text{m}$ ).

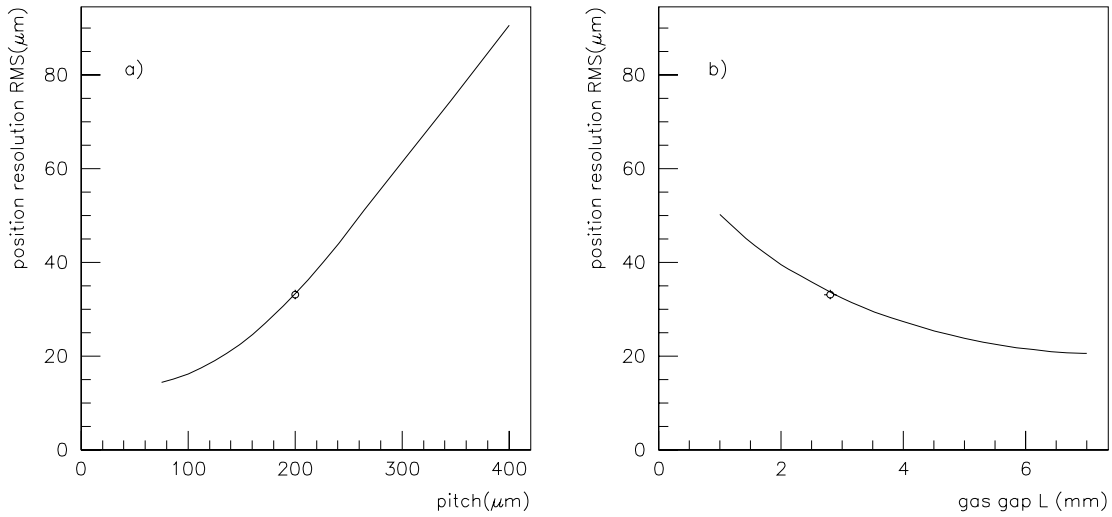


Figure 4.5: a) The position resolution as a function of the pitch for an MSGC with  $L = 2.8 \text{ mm}$ . The point represents the test beam result using the same position determination algorithm. b) The position resolution of an MSGC as a function of the gap thickness  $L$  with pitch  $p = 200 \mu\text{m}$ . The point represents the test result.

If a large pitch is chosen, the resolution is determined by the anode pitch (undersampling). Most tracks then give a signal on a single strip; only tracks that cross in the middle between two strips will cause signals on two strips so an accurate position determination can be done by the centre-of-gravity method. The straight part of the curve in figure 4.5a can therefore be approximated by the relation

$$\sigma = \frac{p-d}{p} \times \frac{p}{\sqrt{12}}, \quad (4.5)$$

where  $p/\sqrt{12}$  is the resolution when there is no transverse diffusion at all, and  $d$  is the average

diameter of the electron cloud after diffusion ( $d \propto \sigma_T \sqrt{L}$ ). The above relation only has a meaning in the undersampling region, that is when  $p > d$ . The curve shown in the figure yields  $d \approx 90 \mu\text{m}$ . This radius can be increased by choosing a gas mixture with a higher diffusion constant, or simply by increasing the gas gap. At very low pitch, the position measurement error is dominated by the gain fluctuations and the transverse diffusion, both giving an error around  $10 \mu\text{m}$ .

Figure 4.5b shows the effect of varying the gas gap width (thereby varying the electron cloud size and the total signal). For optimal resolution the MSGC should have a gas gap as large as possible within the experimental constraints. These constraints are twofold: the size of the gas gap determines the signal duration (given by the electron drift time) and the larger the gas gap is, the worse the resolution becomes for particles that do not enter the detector perpendicularly.

The model prediction for the resolution of an MSGC with very low pitch has a limited meaning because the uncertainty in the tuning becomes important here, especially in the variance of the gas gain. Also, instrumental effects (e.g. alignment) could have a sizable influence for resolutions below  $20 \mu\text{m}$ . However, both figures indicate that the position resolution of  $30 \mu\text{m}$  measured in two independent beam tests is strongly dependent on the geometry chosen.

#### 4.4 Reprint: study of inclined particle tracks in micro strip gas counters

The article reprinted on the following pages is accepted for publication in Nuclear Instruments and Methods in Physics Research A, and will probably appear in issue 349, around October 1994. This paper and the following are both examples of the application of the MSGC Monte Carlo described in this chapter, for the better understanding of the observed phenomena and the prediction of the detector performance under similar circumstances.

The MSGCs studied in this paper were irradiated with cosmics. The cosmic ray spectrum at sea level consists predominantly of muons with an energy spectrum falling approximately with  $E^{-2}$  [2]. One can expect discrepancies between the Monte Carlo predictions and the data, especially where the Landau distribution of the signal is concerned, because the Monte Carlo was tuned to mono-energetic pions. Indeed such discrepancies are observed and reported, although a more thorough study would be needed to prove that these arise from the different ionisation properties of the probe particles.

One should note that the detecting properties of this device for particles crossing it under large angles can be important in some experiments. In the LHC experiments, the arrangement of MSGC detectors is such that high-momentum particles originating from the vertex will traverse the detectors in the  $(y, z)$  plane (as defined in figure 4.1). However, for low-momentum tracks ( $p_T < 10 \text{ GeV}$ ) the magnetic bending causes an incidence under a significant tilt angle. This results in a worse position resolution and may lead to a lower detection efficiency, as quantified in the following paper. For the LHC experiments, these results are mainly important for the simulation of minimum bias background to the physics events, and for the study of bottom quark decays.



















## **4.5 Reprint: simulation of front end preamplifiers for the MSGC**

The following article on MSGC electronics was released as a NIKHEF preprint. It provides part of the answer to the question whether the MSGC signals would be better amplified with a preamplifier/shaper or a preamplifier/integrator in combination with a Double Correlated Sampling (DCS) algorithm. These two algorithms (labeled Fastplex-A and Fastplex-B in the paper) are compared, and it is shown that the DCS method is more effective when high speed is a requirement, like in the LHC experiments. The DCS method was therefore adopted in the development of the Fastplex preamplifier.

In the line of this thesis, this article can be read as an example of the application of the MSGC Monte Carlo in design studies. It does not contain essential information that is used in the coming chapters of this thesis, and can therefore be skipped if found too technical.

# Simulation of frontend preamplifiers for the MSGC

J. Schmitz

*NIKHEF-H, Amsterdam, The Netherlands*

## Abstract

Two candidate architectures for frontend preamplifiers for the Microstrip Gas Counter are tested using a Monte Carlo simulation of the detector and frontend. The simulation describes ionisation in the gas, electron drift and diffusion, gas amplification, signal development and the discriminator. The first architecture is based on the current design of the Fastplex, while the alternative design uses a subtraction method. The simulations indicate that the current Fastplex-design matches the MSGC best when the shaping time is as high as possible (around 50 ns). The signal is extracted more accurately with the alternative design.

## 1 Introduction

The Microstrip Gas Counter (MSGC) is a very thin gas-filled detector, used for the localisation of relativistic charged particles, and photons. It is based on the geometry and operation of a Multiwire Proportional Chamber (MWPC); to come to a higher granularity than the MWPC can reach, the MSGC has strips etched on an insulating substrate, instead of wires strung in a gas volume. This way the anode-to-anode distance can be decreased to  $\sim 200 \mu\text{m}$ , which leads to a very high rate capability ( $> 1 \text{ MHz}/\text{cm}^2$ ) and good position resolution ( $30\text{--}50 \mu\text{m}$ ). This makes the device a very interesting candidate for charged particle tracking in LHC and SSC experiments.

The geometry of the detector is shown in fig. 1. Particles are supposed to cross the detector vertically, i.e. perpendicular to the strip plane ( $\theta = 0$  in the figure). The distance between the strip plane and the drift cathode,  $L$ , is a few mm. This dimension determines the duration of the signal on the strips, because it takes an electron tens of nanoseconds to drift through this gap, from the top towards one of the anodes.

This paper describes the requirements on a fast frontend preamplifier for the MSGC strip readout. Essentially, with 'fast' we mean that the detector should have a minimal dead time on the scale set by the LHC bunch crossing period of 25 ns. In section 2, the simulation of the MSGC is briefly described. A more detailed description can be found in [1]. Section 3 deals with the different schemes proposed for the frontend preamplifier. The results are listed in section 4.

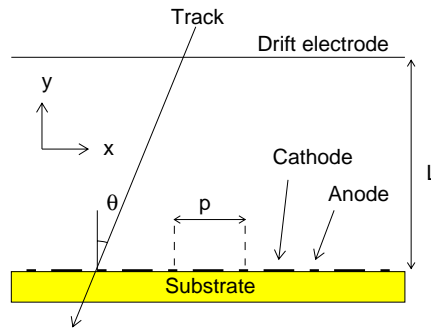


Figure 1: Geometry of the MSGC.

## 2 Description of the Monte Carlo simulation

A two-dimensional projection of the detector is used for simulating the MSGC (as in figure 1). A minimum ionising particle traveling through the detector causes a number of (primary) ionisations of gas molecules (typically 3–25 on a 3 mm track). Each primary electron ( $\delta$ -electron) can in turn ionise more molecules, so the electrons are grouped in clusters. In the simulation, these clusters are pointlike. They occur almost on the track of the crossing particle.

From their starting point, the liberated electrons will drift towards the strip plane with an average speed  $\geq 50 \mu\text{m/ns}$ . While drifting they undergo a displacement in  $x$  because of transverse diffusion. When the electrons reach the quadrupole field (close to the strips) they will be focused towards one of the anodes. Here the electric field is so high that gas amplification occurs: each electron will cause a shower in the gas, and more and more electrons are liberated. This way tens of thousands of electrons will reach the anode strips. This signal is in principle high enough to be detected with state-of-the-art electronics, with noise levels below 1500 equivalent noise charge (ENC).

The detector was described with the following parameters. The gas amplification factor was set to 2000, the drift velocity to  $60 \mu\text{m/ns}$ , the anode pitch to  $230 \mu\text{m}$  and the gas gap to 3 mm. These numbers match the current design of the ATLAS MSGC detector. As a gas mixture we took DME/CO<sub>2</sub> 60/40. Each electron gives rise to a negative current pulse on an anode, with a fluctuating amplitude around 2000 electrons and a decay time constant of 3 ns.

In the simulation the signal development is followed step by step, where each step is around 0.3 ns. In this time bin the signal is assumed to be constant. Usually, most of the noise in a preamplifier is  $kT$ -noise at the input of the first preamplifier component. This white noise is approximated by adding a different Gaussian random number to the bare anode signal in each time bin. The noise is calibrated at the input to give the requested noise level at the preamplifier output. Before the particle crosses the detector, each channel is simulated over a period of 3 times the integrator decay time to randomise

the low frequency component of the noise.

### 3 Two schemes for a fast frontend preamplifier

The MSGC is currently under study for inner tracking in experiments at the Large Hadron Collider (LHC). The high bunch crossing frequency (40 MHz) and high charged particle flux (1% hit probability on each channel) in these experiments call for fast preamplifiers, to have a recovery time of the order of 100 ns or less. Because the signal of an MSGC is spread out over a period of the order of 50 ns, a very fast preamplifier/shaper will tend to 'forget' the first part of the signal even before the last part has come in. This degrades the signal-to-noise ratio. The shaping time of the analog preamplifier of a frontend therefore needs careful optimisation to avoid signal loss in this very first stage of the signal processing.

In principle, this discussion deals with the signal-to-noise ratio of the MSGC together with the frontend preamplifier. But with a signal that is as highly fluctuating as the one from the MSGC, the *average* signal-to-noise does not tell us how often we lose a particle signal. We decided therefore to determine the probability that the signal of a crossing particle goes over threshold (the detector efficiency) for various preamplifier designs, because this is essentially the parameter we are interested in.

Two preamplifier schemes were simulated. At the time of the simulation, no information was available on the expected noise level of these preamplifiers, so this number was left as a free parameter. Instead, we fixed the detector efficiency to 98%, which seems a reasonable aim (there will be other contributions to the overall detector inefficiency but the detector efficiency in this context is just the probability that if everything else works, a crossing particle will be detected by an MSGC monolayer). So all MSGC parameters are fixed, and we determine the maximum tolerable noise level of each preamplifier design. The two schemes simulated as MSGC frontends are shown in figure 2. (These schemes symbolise the implementation in the simulation, not the optimal implementation in reality.) The first scheme, labeled 'Fastplex-A', looks most like the current design of the Fastplex preamplifier [2]. The analog part of this chip has a preamplifier/shaper with a peaking time around 15 ns and a shaping time constant of about 10 ns. It consists of an integrator/amplifier followed by a differentiating element. The shaping time (determined by the values of the resistors and capacitors) should be kept below around 50 ns, because the shaping time determines how long the signal will be over threshold and therefore the dead time of the detector. Two parameters determine the characteristic behaviour of the simulated shaper: the rise time (which is the time the signal needs to grow from 10% to 90% of the peak signal, in response to a test pulse), and the shaping time (the characteristic time of the integrator and differentiator). Both are determined by the values of the resistors and capacitors in the scheme. The discriminator is continuous, it will switch to 1 when the signal at the input goes over threshold and is reset at each bunch crossing clock signal. (A latched discriminator was also tried in the simulation but it combines

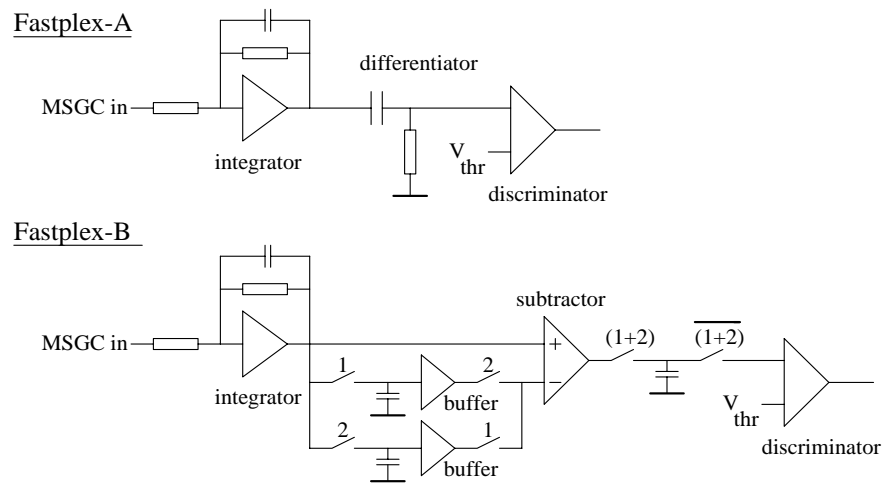


Figure 2: The two schemes compared in the simulation.

very badly with the fast shaper, yielding much signal loss in case the shaping time is less than 40 ns.) In all simulation runs, the threshold was set to 5 times the noise level.

The second scheme ('Fastplex-B') is a bit more complex. It starts with a slow integrator (decay time of the order of  $1 \mu s$ ). The rise time of this scheme will be around 20 ns. Two memory units (capacitors) behind the integrator store the signal every two bunch crossings, alternatingly. This signal is lead through to a subtractor two bunch crossings later, where it is compared to the signal at that time (see figure 3). This way the (latched) discriminator behind the subtractor will switch to 1 when the current integrator output is much higher than the signal two bunch crossings before. (The comparison is made over

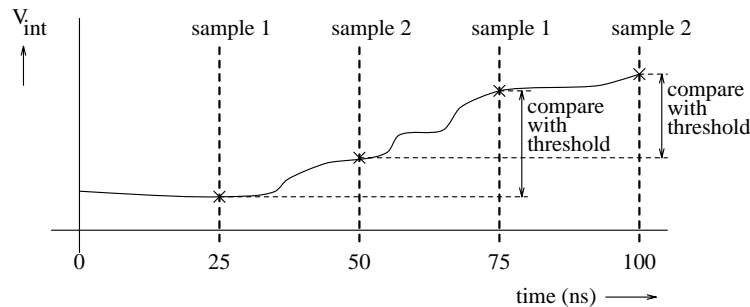


Figure 3: Signal processing of the Fastplex-B behind the integrator. The integrated signal is stored each 25 ns. The discriminator always compares signals between samples that are two bunch crossings apart.

2 bunch crossings (50 ns) because the signal of the MSGC will have a similar duration.) The slower integrator gives a better stacking of the signals from the individual ionisation

clusters, so this scheme will yield a higher signal than the Fastplex-A. On the other hand, the switches may add to the noise figure, depending on the hardware implementation.

In the simulation, the integration of the signal is approximated by a summation. The signal is divided into time bins of one time unit  $t$ ; the 'integral' at time  $T$  is given by

$$I(T) = \sum_{t=0}^{t=T} S_t (e^{-t/\tau_{int}} - e^{-t/\tau_{rise}}) \quad (1)$$

Here,  $S_t$  is the signal at time  $t$ , and  $\tau_{rise}$  is the characteristic time constant that determines the rise time. It is not the rise time itself, because this parameter is (here) defined as the time in which the integrator output rises from 10% to 90% of the maximum signal, in response to a test pulse. Although in real life  $\tau_{rise}$  and  $\tau_{int}$  are not independent, they are varied separately in the Monte Carlo.

The differentiation (in case A) is described by the weighted differential sum

$$D(T) = \sum_{t=0}^{t=T} (I_t - I_{t-1}) e^{-t/\tau_{dif}} \quad (2)$$

The differentiation causes an undershoot of the signal which gives rise to a recovery time. The response of preamplifier A to a single electron is shown in different stages in figure 4 (the noise is switched off). The negative tail of the differentiator signal gets longer with

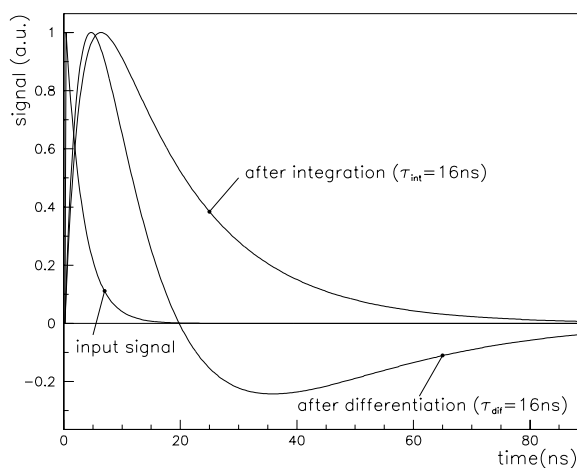


Figure 4: *Ideal response of the integrator and differentiator to a test pulse for case A with a shaping time of 16 ns and a rise time of 0 ns. All curves are normalised to 1 separately. Note that even this infinite bandwidth integrator does not come up at once because of the exponential tail of the input signal.*

a longer integration and differentiation time; this forces us to use time constants as low as possible. We limit ourselves to  $\tau_{int} < 50$  ns. We set  $\tau_{int} = \tau_{dif}$  in all simulations of the Fastplex-A, so that the shaping time is simply equal to  $\tau_{int}$ .

The integrator of the Fastplex-B has a much higher integrator decay time, of at least  $1 \mu\text{s}$ , so that the negative tail is smeared out over a much larger time interval. Therefore it will not contribute significantly to the signal of later events. The implication of this large integration time is that signals from consequent particles will add up, because it takes the signal from one particle very long to return to zero. This should match the expected rate of  $10^5$  Hz per strip, so  $\tau_{int}$  should be less than  $10 \mu\text{s}$ .

With both schemes one should be careful to avoid integrator saturation when a lot of charge is injected at the input. In that case the preamplifier will be dead for many microseconds. As a benchmark event one can take the case that a  $\gamma$ -ray coming from the Transition Radiation Detector in the ATLAS experiment, converts into an  $e^+e^-$  pair in the detector. The energy of such a photon can be tens of keV's (it is 6 keV on average). If we want the preamplifier to be able to handle a 30 keV  $\gamma$ , it should not go into saturation at an input charge of 2,000,000 electrons (while the discriminator level is set typically on 10,000 electrons). This sets a scale for the needed dynamic range of the preamplifier.

The bunch crossing scheme of the LHC shows periodical gaps where no beams interact; one can reset the preamplifier on these bunch crossings (by discharging the integrator capacitance). This limits the period of saturation.

## 4 Optimisation of the frontends for the MSGC

For the Fastplex-A, the Monte Carlo predicts a typical MSGC signal as shown in figure 5. The top left figure shows the signal coming from the anode. Each peak corresponds to the arrival of a cluster to the anode, and the tail of the peak has a decay time of 3 ns, determined by the velocity of the ions that drift away from the anode after the gas amplification process. The figure on the top right is the same signal plus white noise. The signal is integrated with a time constant  $\tau_{int} = 40$  ns, of which the result is shown in the bottom left figure. After the differentiation (with time constant  $\tau_{dif} = 40$  ns) the signal looks as in the bottom right figure. The Fastplex-B performs an almost ideal integration of the anode strip signal with a rise time of  $\sim 20$  ns and a very high decay time.

Figure 6 shows the results of the MSGC/frontend simulation. In this figure the signal is kept constant, and the noise is tuned to such a value that the resulting detector efficiency is  $98.0\% \pm 0.05\%$ . The actual values of the maximal noise are very sensitive to small variations of the electron drift velocity, gas gap thickness and gas mixture, so only comparative conclusions can be drawn. The shaper circuit (case A) turns out to have a strong bias towards relatively high shaping time. With a higher shaping time, the signals from individual clusters are stacked on top of each other giving rise to a higher signal. It also shows a bias towards high rise time. When the rise time is high, the signal slowly approaches the peak value, so it is high over a long period. When the rise time is 0, the signal falls off right from the start. So a longer rise time yields a signal that is maintained longer, thus giving again a better stacking of the different pulses from the primary clusters.

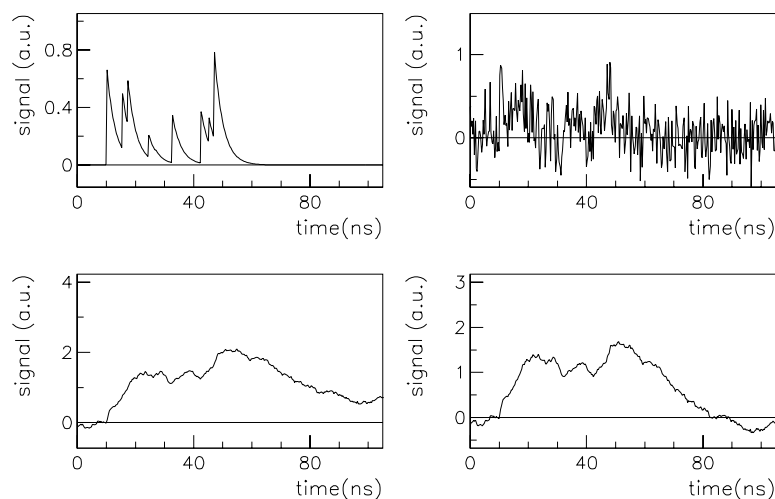


Figure 5: Typical signal on an MSGC anode, before the integrator, after the integrator and after the differentiator.

The Fastplex-B shows no significant difference in performance as we vary  $\tau_{int}$  in the region of interest. This is not surprising because the integrator time constant is higher than the largest time constant in the MSGC in this case. The integration time of the Fastplex-B can be optimised on different criteria than detector efficiency, e.g. on the expected noise level. A small rise time is preferred because the introduction of a rise time results in a smearing of the signal in time so that the subtraction does not yield exactly the collected charge during the past 50 ns.

Note that the scales are very different for the two amplifier schemes. The high shaping time curves have no points at the low edge of the graph, because  $\tau_{int}$  should be larger than  $\tau_{rise}$  in equation 1.

## 5 Conclusions

As compared to signals from silicon strip detectors, the signal from an MSGC has a low amplitude and is highly stochastic; it therefore needs careful handling. The presented simulations show that to achieve a good detector efficiency, it is necessary to integrate the signal of the MSGC strips with a time constant  $> 40$  ns to smooth the spiky signals. One can either use a fast shaping circuit ( $\tau \approx 50$  ns) combined with a continuous discriminator, or a very slow integrator ( $\tau \approx 1 \mu s$ ) if the signal difference over a certain time slot is discriminated. The latter scheme seems preferable, because the requirements on the discriminator are much easier to fulfill and the maximum tolerable noise is about 25% higher than with the fast shaping circuit. A disadvantage is the complexity of the Fastplex-B scheme. Of course, there are more parameters involved in a proper comparison of the

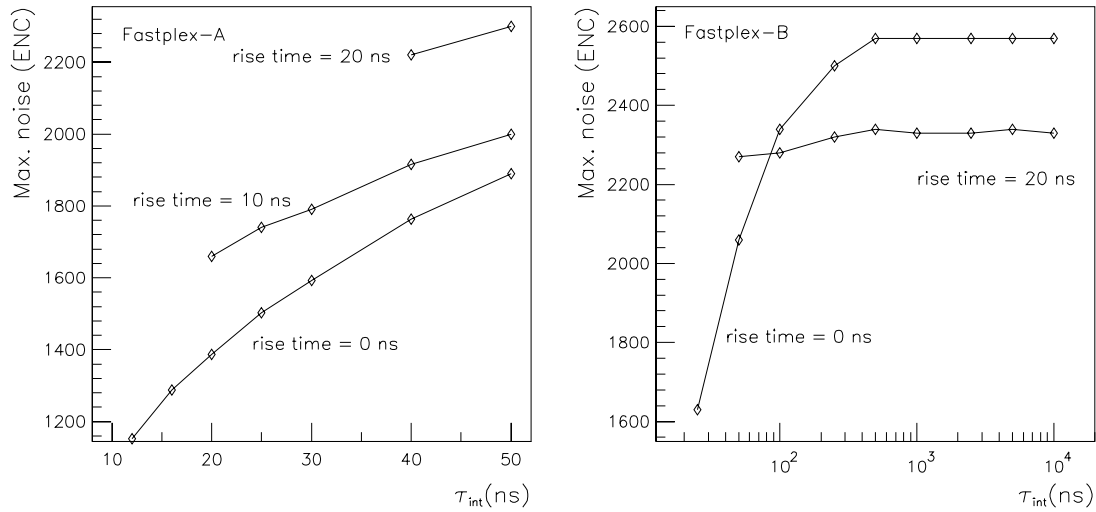


Figure 6: Noise level (in equivalent noise charge) that can be tolerated in the Fastplex-A and Fastplex-B schemes, as a function of the integrator rise and decay time. The shown noise level yields a 98% MSGC efficiency when the discriminator threshold is set to  $5 \times \text{noise}$ .

two than just the detector characteristics discussed in this paper. A detailed simulation or test batch of the frontend electronics is required to find out whether the needed low noise levels can be obtained.

## 6 Acknowledgements

This work would have been impossible without the input from Ruud Kluit and Paul Rewiersma concerning the behaviour and simulation of the two preamplifier schemes. Ruud Kluit also provided me with figure 3. Bob van Eijk came up with many useful suggestions.

## References

- [1] J. Schmitz, Nucl. Instr. and Meth. A323 (1992) 638.
- [2] F. Angholfini et al., CERN 90-10 (1990) 84.

## Chapter 5

# The ATLAS inner detector

This chapter gives an overview of the ATLAS inner detector layout. The author contributed to the design of the inner detector of ATLAS, and its predecessor EAGLE. This work is documented in the following reports:

A. POPPLETON, K. BOS AND J. SCHMITZ, *Momentum resolution of three tracker designs for Eagle*, EAGLE INDET-NO-001;

K. BOS, M. GEIJSBERTS, F. HARTJES, J. SCHMITZ, F. UDO AND J. VERMEULEN, *Technical aspects of a MSGC detector for Eagle tracking*, EAGLE INDET-NO-006;

A. POPPLETON, K. BOS AND J. SCHMITZ, *The radiation thickness of three Eagle trackers*, EAGLE INDET-NO-008;

K. BOS AND J. SCHMITZ, *Detector positions in the ATLAS forward tracker*, ATLAS INDET-NO-019;

V. KLYUKHIN, A. POPPLETON AND J. SCHMITZ, *Field integrals for the ATLAS inner tracker*, ATLAS INDET-NO-023;

B. VAN EIJK AND J. SCHMITZ, *A proposal for the ATLAS inner tracker based on the Panel and Coseners House layouts*, ATLAS INDET-NO-050;

THE ATLAS COLLABORATION, *Letter of intent for a general-purpose pp experiment at the Large Hadron Collider at CERN*, CERN/LHCC/92-4.

### 5.1 Introduction

Much of the effort that went into the development of the MSGC was based on the expectation that this detector can be used in LHC experiments. By the time of this writing, the experience with MSGC prototypes has led to confidence that a large scale tracker consisting of these detectors can be realised. The LHC committee has expressed its approval for two proton-proton experiments, namely ATLAS and CMS. The Microstrip Gas Counter plays an important role in both these experiments.

The ATLAS and CMS collaborations are now in the final stage of writing their Technical Proposals, in which the design of the experimental setup will be described in full detail. The basis for these experiments was earlier documented in two Letters of Intent [65, 66] and four

progress reports [67]-[70]. The primary goal of the experiments is to identify and study the Higgs boson if it exists in the mass range 80–1000 GeV. The experimental arrangements are optimised at first such that the visibility of the Higgs signal is as good as possible (within practical constraints).

The coordinate system of the LHC experiments is the following: the beam axis is the  $z$ -axis. The vertical coordinate is  $y$ , and the direction of  $x$  then follows from the right-handedness of the system (see figure 5.1). Positions and directions are also expressed in the radius  $r$ , the angle  $\phi$  and the pseudorapidity  $\eta$ :  $\phi$  is the angle in the  $(x, y)$  plane,  $r^2 = x^2 + y^2$ . The pseudorapidity is defined as

$$\eta = -\ln \tan \frac{\theta}{2}, \quad (5.1)$$

while  $\theta$  is the angle in the  $(r, z)$  plane. The spatial location of  $\eta$  is illustrated in figure 5.1. In the final state of an inelastic hadron-hadron collision the particle density per unit of  $\eta$  and  $\phi$  is constant (in the high energy limit), on average. Hence the preference for these coordinates. The transformation  $\eta \rightarrow -\eta$  equals  $z \rightarrow -z$ . Often the pseudorapidity is called rapidity (as in this thesis), although the rapidity ( $y$ ) has a slightly different definition [9].

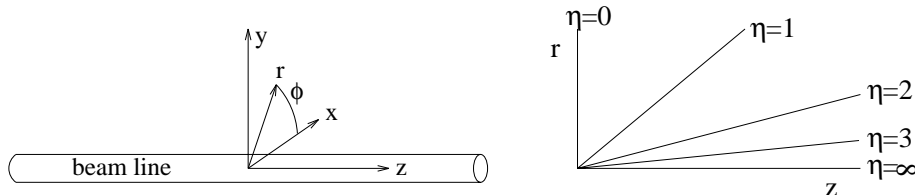


Figure 5.1: *Left: the coordinate system in hadron collider experiments. The origin lies at the (average) interaction point. The direction along the beam is  $z$ , the vertical direction  $y$ . Right:  $\eta$  values in the  $rz$  plane.*

In this chapter, the design of the ATLAS inner detector is discussed in detail. The purpose of the tracker is given; then the available track detector technologies are listed with their most important characteristics. Finally, the "Cosener's House" layout of the ATLAS tracker is discussed, and performance estimates are given.

## 5.2 The ATLAS experiment

The layout of the ATLAS experiment is shown in figure 1.3. A rather detailed description of the experimental setup is given in [67], and in the near future in the ATLAS Technical Proposal; here, only a brief overview is given. The experiment consists of a central part, called the barrel, two end-caps, and plug-shaped calorimeters at both ends. The outermost part of the detector is a muon spectrometer: it consists of superconducting toroidal magnets, that bend muon tracks with a bending radius related to their momentum. Three layers of muon detectors are used to localise the muon and to determine its curvature in the magnetic field. This results in knowledge of both direction and momentum of the particle. The coverage of

this muon system is  $|\eta| < 2.8$ , that is, a polar angle of  $\pm 7^\circ$  around the beam is not covered. The momentum resolution of this muon system is shown in figure 5.2, as a function of the muon momentum and the rapidity.

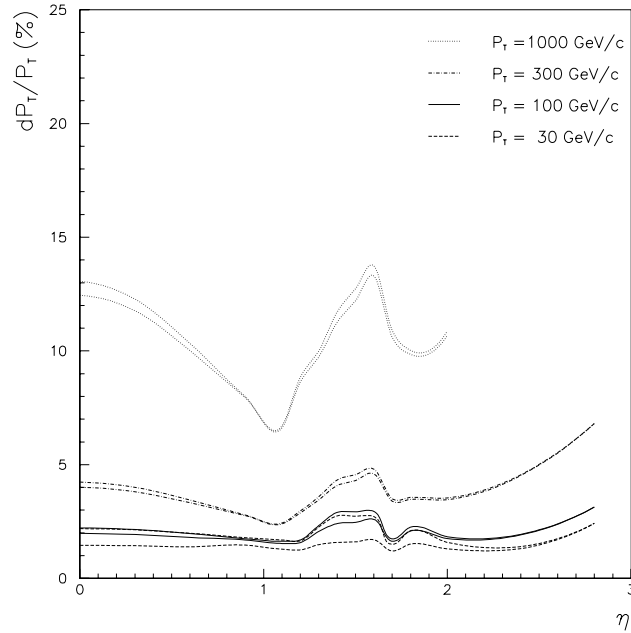


Figure 5.2: The resolution of the ATLAS detector for muons as a function of  $\eta$ , for different muon momenta, and using only the outer muon system (upper curves) or a combination of the outer and inner detector information (lower curves). The inner detector significantly improves the resolution for low-momentum muons, where the outer muon measurement is affected by multiple scattering in the calorimeters. Taken from [67].

Inside the muon system we find the calorimeters. When a particle is stopped in this calorimeter, the location of the energy deposition provides information about its nature, as described in section 1.3.3: photons, electrons and positrons are stopped in the first part of the calorimeter (called the electromagnetic calorimeter), while hadrons are stopped in the deeper regions of the calorimeter (the hadron calorimeter). Because of our special interest in photons and electrons the resolution of the electromagnetic calorimeter is of prime importance. For this reason the technique of Liquid Argon calorimetry was chosen, with as a design goal an energy resolution of

$$\frac{\Delta E}{E} = \frac{0.10}{\sqrt{E}} \oplus 0.01 \oplus \frac{0.3}{E}, \quad (5.2)$$

where  $E$  is in GeV. (The techniques with an even better resolution in the energy region of interest were considered too expensive.) A preshower detector in front of the electromagnetic calorimeter, covering  $|\eta| < 2.3$ , enhances the particle identification power.

The hadron calorimeters are less accurate (which is partly due to the nature of hadron showers): these will be scintillating tile calorimeters in the barrel, with a target hadronic

energy resolution of

$$\frac{\Delta E}{E} = \frac{0.50}{\sqrt{E}} \oplus 0.03. \quad (5.3)$$

An interesting aspect of the scintillating tile calorimeter is, that the tiles point towards the collision point, contrary to the commonly used orientation. This introduces a loss in resolution, but it makes it much simpler technically to guide the scintillator light from the tiles to the outside of the detector.

In the end-cap, a scintillating tile calorimeter is not suited because of the amount of radiation expected in that area. For this reason the end-cap hadronic calorimeter is a Liquid Argon calorimeter, which is more radiation hard. This calorimeter will cover out to  $|\eta| = 3$ . Two forward calorimeters extend this coverage out to  $|\eta| = 5$ , which is needed to identify events with missing (transverse) energy. These calorimeters are not too accurate but need to be extremely radiation resistant. The technology for this detector has not yet been chosen.

The inner detector is probably the most complex system. The environment inside the electromagnetic calorimeter is very hostile: everything in the inner cavity is subjected to a high flux of pions, photons, and neutrons. The pions and photons are produced in inelastic proton-proton interactions at the collision point (at a rate of order  $10^9$  Hz). The total charged particle flux in a unit (normal) area  $dA$  at radius  $r$  from the beam axis is [71]

$$\frac{dN}{dA dt} = \frac{1.2 \times 10^9}{r^2} \text{cm}^{-2} \text{s}^{-1} \quad (5.4)$$

at the nominal LHC luminosity of  $10^{34} \text{ cm}^{-2} \text{ s}^{-1}$ . These particles are predominantly charged pions. The photon flux from  $\pi^0$ -decays has about the same intensity. Neutrons are produced in hadronic showers in the calorimeters, and the neutron flux reaches very high levels because these particles are mainly scattered around within the calorimeter and not absorbed. The mean energy of these neutrons is around 1 MeV, and the flux is of order  $10^{12} \text{ n cm}^{-2}$  per year. Because of these high radiation levels, it is difficult to design a robust inner detector. This design is discussed in the next section.

## 5.3 Layout of the ATLAS inner detector

### 5.3.1 Aims

The purpose of the ATLAS inner detector is primarily to take part in particle identification and particle momentum measurement, and to provide information for the second level trigger. The aims can be listed as follows [72]:

- with the inner detector one should be able to reconstruct efficiently all tracks of charged particles with a transverse momentum above 5 GeV within the rapidity range  $|\eta| < 2.5$ .
- electrons should be reconstructed down to 2 GeV to suppress the background to  $H \rightarrow \gamma\gamma$  from the decay  $Z \rightarrow e^+e^- \gamma\gamma$ .

- We should be able to distinguish between electrons and positrons up to  $p_T=500$  GeV for the study of asymmetries, e.g. in the decay of the hypothetical heavy vector boson  $Z'$ .
- Low-momentum tracks close to high-momentum leptons should also be reconstructed, for instance to identify an asymmetric photon conversion.
- For the second level trigger, the inner detector should provide information to distinguish between electrons, pions and photons when a large energy deposition has occurred in the electromagnetic calorimeter.
- For the study of the bottom quark and tau lepton, a vertex detector should be able to measure the impact parameter of these particles with an accuracy of about  $25 \mu\text{m}$ . The impact parameter measurement can assist in suppressing the background from b-quarks to the signal of t-quarks. The vertex detector will also be used to decide whether tracks originate from the same collision. These physics studies can only be performed at a lower than nominal luminosity. A first level trigger signal may be needed from the vertex detector.

### 5.3.2 Design considerations

The inner detector is surrounded by a superconducting solenoidal coil. The magnetic field causes a bending of charged particle tracks if they have a momentum component perpendicular to the field lines. The total deflection  $d$  of a high-momentum particle in a magnetic field  $B$  after travelling a path of length  $L$  is [73]

$$d(L) = \frac{0.3}{p_T} \int_0^{L \sin \theta} \int_0^{r/\sin \theta} B \sin \theta \, dl \, dr. \quad (5.5)$$

where  $\theta$  represents the angle between the track and field vectors. (In a solenoidal field parallel to the beam as in ATLAS, the deflection is in the  $r\phi$  direction if the  $\phi$ -component of the particle momentum can be neglected.) The magnetic field allows for a determination of the (transverse) momentum of all charged particles. When the magnetic field is homogeneous, the trajectory of a charged particle is a helix, and  $d$  is proportional to  $B(L \sin \theta)^2 = BR^2$ . For a precise measurement of the track bending, we need accurate tracking detectors to determine  $d$ , and a large  $BR^2$ . In ATLAS a magnetic field strength of 2 T is chosen in combination with  $R = 1.06$  m.

Along the beam axis, the inner tracker extends out to  $z=\pm 3.40$  m. The radial and longitudinal dimensions are determined by a trade-off between inner detector performance and calorimeter cost (a larger inner detector gives a larger  $BR^2$ , but with a radial increase of the inner detector the calorimeters and muon system are pushed outward). Inside this volume, four separate tasks must be fulfilled for all charged tracks within  $|\eta| < 2.5$ : vertexing, photon conversion identification, tracking and electron identification.

## Vertexing

The origin of each charged track must be determined. This will allow us to separate the different collisions that occur simultaneously due to the high luminosity of the LHC machine, because the simultaneous collisions will be separated, most clearly in the  $z$  direction (see table 1.3). The identification of b-quarks and  $\tau$ -leptons through their impact parameter also relies on the precise knowledge of the vertex.

Vertexing is easiest with a tracking detector very close to the interaction point. With a highly accurate measurement of the track direction the extrapolation back to the vertex has a small spatial error. An arrangement of tracking detectors close to the vertex is called a vertex detector.

## Photon conversion identification

A high-energy photon can convert into an  $e^+e^-$  pair by passage through material. It is very important to be able to identify these conversions because otherwise photons produced at the vertex will fake electrons and positrons, and separately we lose statistics on the interesting events where photons are part of the final state (such as  $H \rightarrow \gamma\gamma$ ).

Merely identifying these events from the identification of an  $e^+e^-$  pair with an origin outside the true vertex, is not effective enough because of tracking inefficiency for low-momentum electrons and a poor vertex resolution for a high-momentum  $e^+e^-$  pair. The very first layer of the vertex detector must be highly efficient for charged tracks, so that when we see a charged track without a corresponding hit in the first plane, we know that it comes from a photon that converted later on in the inner detector.

## Tracking

The position of each charged particle must be measured in a few places so that its track is known and the momentum determined. The severe background of low-momentum tracks from minimum bias collisions troubles this tracking. For instance, two low-momentum tracks can fake one high-momentum track when position measurements of the two happen to fit on a helix with low curvature. The most effective way of suppressing this problem is to use tracking detectors with a high resolution (so that the probability that random hits form a good helix is low), and to use many of these detectors in a row so that more than two low-momentum tracks would be needed to fake a high-momentum track. The pattern recognition criterion set by the ATLAS collaboration after early simulations was, that one needs four space point measurements along a track to find only true tracks. The vertex detector measurements are not included in this count, because of the high track density in that region. This pattern recognition criterion has been tested with Monte Carlo simulations to be robust. Implicitly one also requires a good choice of the positions of each of the four space point measurements along the track.

The inner detector should also provide a precise space point at the end of each track to enable an unambiguous association with calorimeter clusters and tracks in the muon chambers.

### Electron identification

Electrons must be efficiently recognised. The recognition of electrons (and positrons) is normally based on their shower profile in the electromagnetic calorimeter, and the match between the measured energy and momentum. Other identification methods can enhance this identification power. Electron identification is difficult but essential in a collider experiment. It is discussed in the following section.

### Practical constraints

The abovementioned tasks must be fulfilled within the following constraints:

- A particle must cross as little material as possible inside the inner detector. The purpose of the tracker is to determine charged particle tracks with minimal interference; the particle ideally should not deviate or lose energy before the calorimeter. Still, any detector will consist of some material or other. Thin, low- $Z$  materials are preferred.<sup>1</sup>
- The inner detector should be modular and easy to take apart so that replacement of malfunctioning elements is possible.
- All detectors should be aligned to a precision close to their intrinsic position resolution or (preferably) better.
- The detectors should not interfere with each other in a harmful way (the temperature of each detector should be kept to a proper level individually; there should be no electromagnetic interference).
- The whole inner detector, as well as the beam pipe, has to be supported from a cylinder (the cryostat wall) between the inner detector and the solenoidal magnet.
- For safety reasons, some materials are completely excluded for use in the experiment, others may be used only in limited amounts [74]. For instance, the total amount of flammable gases in the experiment should not exceed the equivalent of 40 kg hydrogen, unless the gases are mixed with inert gases in a safe and guarded ratio.
- The detectors should be able to withstand 10 years of running at the nominal LHC luminosity, without serious radiation damage or other aging effects.

#### 5.3.3 Electron identification

The electron plays a very special role in the physics of the Large Hadron Collider. Electrons and positrons are created in processes like  $H \rightarrow e^+e^-e^+e^-$  and  $t \rightarrow W^+b \rightarrow e^+\nu_e j$  (where  $j$  stands for jet). These processes can be exploited to measure the mass of the Higgs boson and

---

<sup>1</sup>The 'amount of material' is usually expressed in the number of radiation lengths crossed by a particle. The radiation length ( $X_0$ ) is defined as the amount of material in which an electron loses all but  $1/e$  of its energy by bremsstrahlung on average.

the top quark. But although electrons in the final state are easy to recognise, there is a huge background problem. This background consists of real electrons and other particles giving an electron signature in the detector. The main sources of real electrons with a transverse momentum  $p_T > 10$  GeV are (X and X' signify 'anything'):

- $pp \rightarrow Z X \rightarrow e^+e^- X$ ;
- $pp \rightarrow W^\pm X \rightarrow e^\pm \nu X$ ;
- $pp \rightarrow \tau^\pm X \rightarrow e^\pm \nu \bar{\nu} X$ ;
- $pp \rightarrow b\bar{b}X \rightarrow e^\pm \nu X'$  (a so-called semi-leptonic decay of the bottom quark);
- $pp \rightarrow t\bar{t}X \rightarrow e^\pm \nu X'$ ;
- $pp \rightarrow \gamma X \rightarrow e^+e^- X$  (photon conversion).

Electrons from these sources are much more abundant than those from an interesting process like  $H \rightarrow e^+e^-e^+e^-$ , as can be seen from the cross sections in figure 1.1, so there is a need to identify the source of an electron. The most common methods are, to determine whether an  $e^+e^-$  pair has an invariant mass equal to  $m_Z$ , to look for missing transverse energy to identify the subprocesses involving neutrinos, and to look for an impact parameter (to recognise electrons coming from  $\tau$  or b decays). This type of source identification is effective, but the mere abundance of background makes it inevitable that occasionally a wrong event passes all the cuts and is still regarded a Higgs candidate. We will return to his problem in the last chapter.

Apart from these real electron rates, there are also other processes that leave an electron signature. The standard signature of an isolated electron is the following:

- a localised energy deposition in the electromagnetic calorimeter;
- a curved track in the inner detector, pointing towards the electromagnetic cluster;
- no signal in the hadronic calorimeter and the muon chambers behind the electromagnetic cluster;
- in the energy range considered ( $>1$  GeV), a perfect match between the curvature of the track and the energy deposition in the calorimeter, such that  $E=p$  (because  $m_e \ll E$ ).

When needed, the electron identification can be enhanced with dedicated detectors: a pre-shower detector, measuring the activity in the first radiation lengths of the calorimeter, and a Transition Radiation Detector, that identifies electrons by their enhanced cross section for generation of transition radiation (see section 5.3.4). The sources of fake electrons are Dalitz decays, photon conversions and jets. Dalitz decays ( $\pi^0 \rightarrow e^+e^-\gamma$  and  $\eta^0 \rightarrow e^+e^-\gamma$ ) and photon conversions can simulate a single electron when one of the two electrons is not reconstructed (in the case of Dalitz decays, this occurs frequently because the electrons obtain a different energy). An ATLAS-specific study [75] shows that the rate of Dalitz decays and conversions

passing the above electron criteria are around a factor 10 below the electron rate from  $W \rightarrow e\nu$ , and therefore sufficiently well suppressed.

Although jets look very different from electrons, their mere abundance ( $\sim 10^5$  times higher than the real electron rate) determines that even if only a small fraction of the jets leave the signature of an electron, this can lead to a large background. A jet can leave a single particle signature when most of the (transverse) energy of the jet is carried by one particle. In a study for ATLAS [76] the rejection of jets was shown to be adequate to push the rate of jets faking electrons to the level of the real electron rate with the conventional electron identification tools described above plus a preshower detector. When the large theoretical uncertainties on the properties of jets are taken into account, this fake electron rate may still be a severe problem. For this reason, additional electron identification power is needed in the ATLAS detector, which is the reason to build a Transition Radiation Detector in the inner tracker. This detector assists in electron identification in the energy range 20–40 GeV. Its main contribution to the physics of ATLAS is in B-decay studies.

### 5.3.4 Available detector technologies

The technologies that are radiation resistant enough to be used in the LHC inner cavity, are listed below. Three types can be distinguished: gas filled detectors, semiconductor detectors, and scintillators. Their main characteristics are listed in table 5.1. In the environment of the Large Hadron Collider, the high bunch crossing frequency and high charged particle multiplicity determine that the position resolution of these devices is not as good as the intrinsic resolution. In the case of semiconductor detectors, the resolution is deliberately worse than the optimum to reduce cost.

Detector technology	Active medium	Intrinsic pos. resolution	Pos. resolution in ATLAS	Intrinsic signal speed
MSGC	gas	30 $\mu\text{m}$	50 $\mu\text{m}$	50 ns
straw tube	gas	$\sim 100 \mu\text{m}$	180 $\mu\text{m}$	100 ns
Si detector	silicon	$\sim 5 \mu\text{m}$	15–60 $\mu\text{m}$	<5 ns
GaAs detector	gallium arsenide	$\sim 5 \mu\text{m}$	20 $\mu\text{m}$	<5 ns
Scintillating fibre	scintillating plastic	> 60 $\mu\text{m}$	–	<5 ns

Table 5.1: The technologies available for tracking at the LHC. The quoted numbers are indicative.

### Microstrip Gas Counters

The Microstrip Gas Counter has been described extensively in the previous chapters. The intrinsic resolution of these devices is 30  $\mu\text{m}$  in one direction (the position resolution in the other two directions is of the order of millimetres). In the ATLAS design, we assumed that the

MSGC position resolution is  $50 \mu\text{m}$ , because of various instrumental imperfections (due to fast signal processing, malfunctioning channels, etc.). The alignment error will add systematically to this resolution.

### Straw tubes

A coarser gas filled detector is the straw tube. It is a thin cylindrical tube with a conducting inner surface, on negative potential. A wire is strung in its centre, which is held at positive voltage. Filled with an appropriate gas mixture, the straw tube can be operated in proportional mode or with higher gas amplification. A pack of these straws can be a very simple, cheap and robust charged particle detector, with a somewhat worse position resolution than MSGCs and semiconductor detectors. The distance of a traversing particle from the anode wire can be derived from the arrival time of the signal on the anode. This yields a position resolution of the order of  $100 \mu\text{m}$ , depending on the gas mixture used and the electronics.

Straw tubes are the detecting elements in a transition radiation detector. This detector is based on the following mechanism: when charged particles cross a transition of two materials with a different dielectric constant, they have a probability proportional to  $\gamma(=\frac{E}{m})$  to emit photons in the keV range. This effect is most pronounced for electrons due to their high  $\gamma$  factor. In a transition radiation detector, this radiation is generated in foam layers or thin foils. For the detection of these photons the straws are filled with a high- $Z$  gas like Xenon (with additives to improve the gas characteristics). The combined inefficiencies of transition radiation generation and detection lead to the need for many layers of radiator and straws, to be able to efficiently distinguish electrons from other particles. The electron identification power increases exponentially with the number of radiator/detector layers.

### Silicon Strip Detectors

Silicon Strip Detectors are based on the release of free charge by a particle traversing matter. When a diode is set on reverse bias, there is only a small (dark) current. On the passage of a particle through the depleted region, electron-hole pairs are created, which results in a briefly enhanced conductivity of the depletion region. This gives rise to a peak in the electric current through the detector. In a way this principle is similar to the detection mechanism of particles with the MSGC, only, the active material is a solid: monocrystalline silicon. Silicon Strip Detectors are a common device in modern high energy physics experiments, because their intrinsic resolution can be better than  $5 \mu\text{m}$  (depending on the size of the diodes), a pulse duration shorter than 5 ns can be achieved, and the silicon wafer can be made very thin so as to have minimal interference with the particle studied. On the other hand, the silicon wafers are too expensive to be used in large quantities. Estimates vary, but in the budget of ATLAS, the Si-detectors are assumed to cost 2.7 times more than MSGCs, per channel; the cost ratio per unit area is even higher. The radiation hardness of Silicon Strip Detectors is currently only just sufficient for the application in LHC inner trackers.

A variation on the commonly used Silicon Strip Detectors is the Silicon Pixel Detector. This is a detector with small silicon diodes, instead of the long strips usually made. The

advantage of the high granularity are a better rate capability and good resolution in two coordinates, both giving excellent pattern recognition capabilities. Its development only started recently, and therefore pixel detectors cannot be regarded as a 'proven technology' like normal Silicon Strip Detectors. These devices could be very effective for the position measurement of charged particles close to the interaction point (in vertex detectors).

### **Gallium Arsenide Detectors**

Another variation of Silicon Detectors is the Gallium Arsenide Detector. When gallium and arsenic are mixed very accurately in a ratio 1:1, the resulting monocrystal has properties similar to monocrystalline Si. It is found that electrical equipment made out of this (more expensive) semiconductor is more radiation hard. This can be advantageous in a vertex detector, where the radiation levels are high (and only few wafers are needed).

### **Scintillating Fibres**

A different solid-state approach to tracking is via the use of a scintillator. A scintillating material is a transparent material that emits light on the passage of a charged particle. The intensity of the light is measured with a photomultiplier, a CCD-camera or other devices. Scintillators have been used in many experiments, in different shapes and sizes. For tracking particles in the LHC environment, a scintillator must be very compact to keep the occupancy of each element low enough to recognise tracks. A natural solution is to bundle a group of scintillating fibres and detect the light at the ends of the bundle. When thin fibres are used and read out separately, a good position resolution can be achieved, in principle given by the radius of the fibre. Miniaturisation is limited by the decrease of the light production and transmission in the fibre. The use of scintillating fibres for tracking at the LHC was studied by RD7 [77].<sup>2</sup> The main problem with scintillating fibres is the difficulty of sensitive and granular light readout, which is especially hard in a strong magnetic field. Eventually the ATLAS and CMS collaborations decided against the use of this technology for tracking. All other technologies listed in this section can be found in at least one of the two inner detectors.

#### **5.3.5 The Cosener's House layout**

The design of the ATLAS inner detector changed since the Letter of Intent, and may be refined again. The design presented in this section is known as the "Cosener's House" layout, as it was agreed upon in a meeting in Cosener's House (Abingdon, UK) in 1993. It is documented in reference [72].

The Cosener's House layout of the inner detector is shown in figure 5.3. The most striking feature of the ATLAS inner detector is the Transition Radiation Tracker (TRT). The TRT is used to enhance the electron identification in the momentum region of 20–40 GeV, as discussed in section 5.3.3. This detector requires about 40 cm radial space, to achieve the

---

<sup>2</sup>A liquid scintillator in a capillary structure has also been under investigation as a tracking device [78].

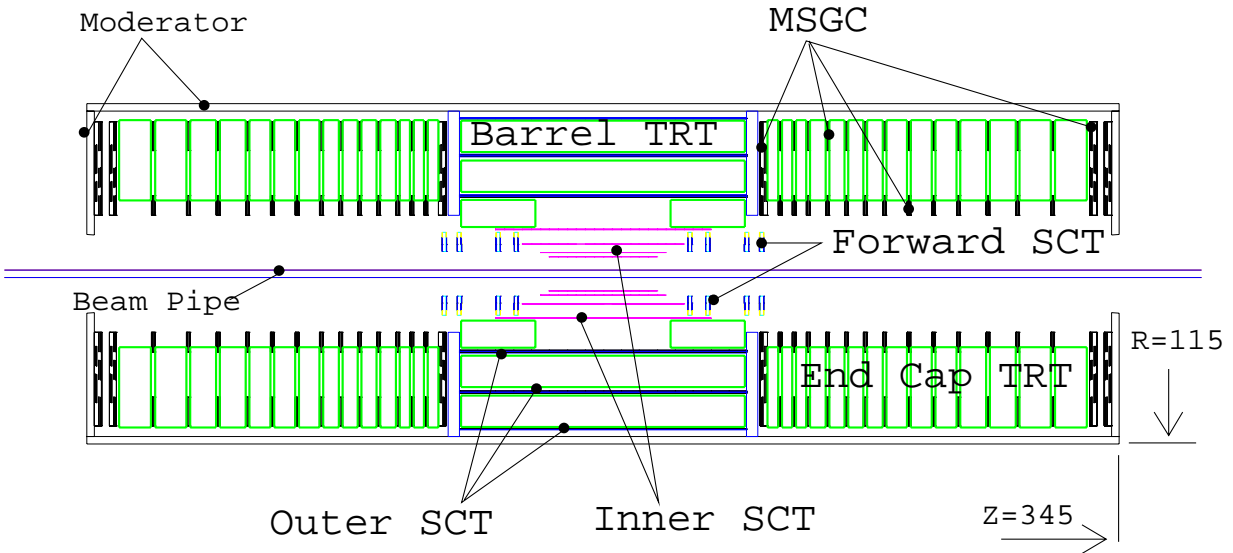


Figure 5.3:  $R$ - $z$  view of the *Cosener's House* layout of the ATLAS inner detector.

specified electron identification. Unfortunately this limits us in the design of the precise tracker needed to determine the bending of highly energetic particles.

The precise tracker should provide a few space points along the track of each particle within  $|\eta| < 2.5$ . The orientation of the precision detectors follows from the requirement that a particle should cross a minimal amount of material. For that reason the substrates should be positioned approximately perpendicular to the direction of the particles coming from the interaction point. Ideally this leads to an arrangement of thin-layer detectors on spherical surfaces around the interaction point; however, this is a technically difficult solution. The tracker is usually split into a barrel part, where detector layers are positioned on cylindrical surfaces around the beam axis, and two forward parts, where detector layers are mounted on discs around the beam pipe. When minimising the amount of material is of prime importance, the most effective boundary between the barrel and forward regions is along the line  $\theta = 45^\circ$ .

From a financial point of view, the cylinders and discs should be instrumented with MSGCs. However, in the barrel the magnetic field causes deterioration of the detector performance, because here the electric field and the magnetic field are perpendicular and give rise to a Lorentz angle in the electron drift (see section 2.3.3) which is around  $8\text{--}10^\circ$  at  $B = 2\text{ T}$  [68]. This can be compensated by a rotation of the detector with the same angle. In a practical arrangement the compensating rotation is fixed, and therefore the operation is confined to a limited combination of gas mixtures and high voltages. This orientation of the detectors also gives rise to an increased complexity of support structures and requires additional radial space.

In the CMS inner detector, the barrel tracker indeed consists of MSGC layers tilted with the Lorentz angle (around  $15^\circ$ ). In the case of the ATLAS detector, a barrel MSGC tracker and the TRT do not fit in the available radial space. Here, Silicon Strip Detectors are used.

For the vertexing, a dedicated vertex detector will be built: it consists of a few layers of Silicon Detectors very close to the interaction point, in the barrel, and Gallium Arsenide Detectors for the forward region. The other detectors are positioned outside  $r = 40$  cm, because severe radiation levels are expected close to the beam. The arrangement of the barrel detectors was based on the assumption that equidistant precision layers would provide the most robust level-2 trigger information on high-momentum tracks, independent of TRT track information. The TRT is positioned as far outward as possible because in the barrel region, a high straw occupancy is foreseen which gets lower with increasing radius. The Silicon Strip Detector layer between the two large TRT modules seriously degrades the TRT performance (because it absorbs the transition radiation that is generated in front of it), which is one of the reasons to re-evaluate the design of the barrel part.

In the forward part, the TRT straw occupancy will be lower, so that the TRT can contribute more effectively to the second level trigger for high-momentum tracks. This allows us to leave a radial gap between 50 and 84 cm. The arrangement of the Transition Radiation Tracker and the precision detectors in the forward region follows from the following arguments:

- within  $|\eta| < 2.5$ , the precise detectors (MSGCs) should provide four space points along the track;
- two of these points are measured approximately halfway between the vertex and the outer radius of the inner tracker cavity (sagitta measurement), while the other two measurements are as far out in radius as possible to make full use of the magnetic field;
- the TRT requires approximately 40 cm of radial space for an efficient separation of electrons from other charged particles;
- the forward TRT consists of modules of either 16 or 24 layers of straw/radiator, which are 7 and 10.2 cm thick in  $z$ , respectively;
- the optimum occupancy of MSGC detectors is 1–2%. A higher occupancy results in pattern recognition problems, while a lower occupancy is not cost-effective. The inner MSGC strips should be around 10 cm long to obtain this occupancy at nominal luminosity, whereas the outer MSGC strips could be twice as long. Production limitations force us to have shorter outer MSGCs (with 16 cm long strips).

MSGC rings are positioned at  $r=40$ –50 cm and  $r=84$ –100 cm. In between the MSGC rings, the TRT is positioned. In the forward part, the TRT consists of foils and radial straws that run from 50 to 100 cm. For ease of installation, the MSGC and TRT detectors are modular. The positions of these modules are chosen such that every particle crosses at least two inner and two outer MSGC wheels [79]. The radial region from 100 to 115 cm is reserved for services, support and a neutron moderator. This hydrogen-rich material will slow down and absorb part of the neutrons, which reduces the radiation damage to the inner detector components.

The outermost MSGC wheels consist of five rings of MSGC detectors, with a radial extension of 10 cm (inner three) and 16 cm (outer two), and 0.5 cm radial overlap. The MSGC

strips are radial; each ring consists of three monolayers of MSGCs. Detectors on the first monolayer are rotated over a small positive angle around their centres, such that the strips point to a spot next to the beam axis. The second monolayer is rotated over the same angle, but opposite sign; the strips of the third monolayer point exactly towards the beam. The small-angle rotation enables us to combine the hit information from two or more detectors to determine both the  $\phi$  and the  $r$  coordinate of the particle. The layout of one detector is shown in figure 5.4.

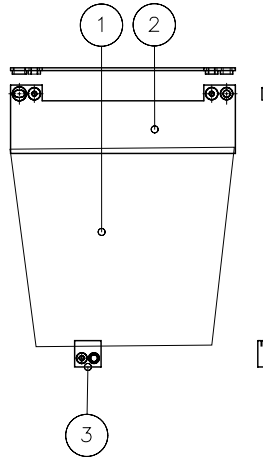


Figure 5.4: An MSGC detector for the ATLAS forward detector. The strip plane (1) carries a pattern that fans out towards the top. The front end chips are mounted on a PCB board on top (2). This PCB board and a clamp (3) hold the substrate and the cathode plane on a frame.

## 5.4 Performance estimates

With computer programs, some estimates of the performance of the Cosener's House inner detector were made. An analytic estimate of the momentum resolution can be made for high-momentum particles given the position and resolution (in  $r\phi$ ) of all detectors. The method used is described in reference [80].

In this computation, the MSGC detectors have a position resolution in the  $r\phi$  direction of  $50 \mu\text{m}$ . The Silicon Detectors will have a resolution of  $20 \mu\text{m}$  (inner three layers) and  $60 \mu\text{m}$  (outer layers). The resolution of the Gallium Arsenide Detectors is  $20 \mu\text{m}$ . Each straw in the TRT has a resolution of  $180 \mu\text{m}$ , which is derived from a drift time measurement, but the straws are not accounted for in the calculation because in this layout they do not add significantly to the momentum resolution achieved with the more precise detectors.

The result of the analytical calculation is represented in figure 5.5. The figure shows the momentum resolution as a function of  $\eta$ , for muons with a fixed transverse momentum of  $500 \text{ GeV}$ . This calculation includes the multiple scattering error (estimated at 1.5%), but

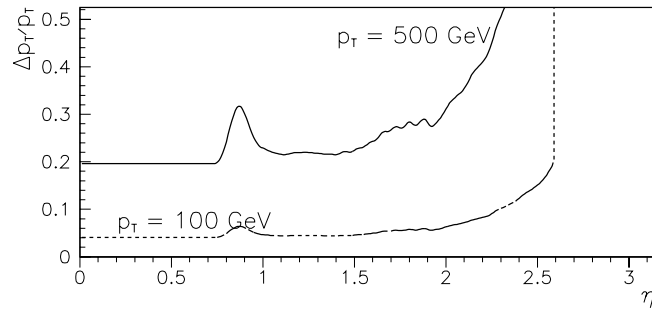


Figure 5.5: Momentum resolution of the inner detector as a function of  $\eta$ , for 100 and 500 GeV muons.

no bremsstrahlung effects. The target resolution,  $\Delta p/p < 30\%$  at 500 GeV, is met out to  $|\eta|=2.3$ . A parametric correction is made for the loss in bending power at high  $z$  due to the finite length of the coil [73].

The material distribution in the inner detector is shown in figure 5.6. This graph was made with a GEANT-based computer model of ATLAS (DICE). The total amount of material crossed exceeds 60% at  $|\eta|=1.5$ , while its average is around 30% over the rapidity interval  $|\eta| < 3$ .

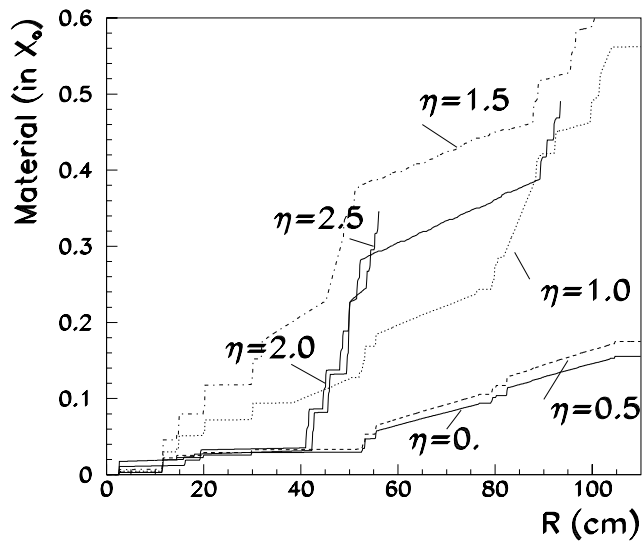


Figure 5.6: The distribution of the integrated amount of material crossed by stiff particles at different rapidity, as a function of the radius. Taken from [67].



## Chapter 6

# Higgs decay into 4 leptons in the ATLAS detector

### 6.1 Introduction

In this chapter the detection of the Standard Model Higgs boson with the ATLAS detector is discussed. Throughout the text of this chapter, the existence of this boson is assumed. We focus on the decay of the Higgs boson into four leptons in the intermediate mass range ( $130 \text{ GeV} < m_H < 180 \text{ GeV}$ ), because this is regarded as a benchmark channel to test the performance of the inner detector. The purpose of this chapter is to illustrate the functionality of the MSGC tracker in ATLAS.

Only one in  $10^9$ – $10^{11}$  proton-proton collisions at the LHC will produce a Higgs boson. When we are looking for this particle, all other collisions can in principle be regarded as background events. However, in practice an event is called a background event when it carries the signature of a Higgs boson decay while it is not. When studying the decay  $H^0 \rightarrow e^+ e^- e^+ e^-$ , in principle all other processes that produce two electrons and two positrons can be considered background. In the same context the real Higgs events are referred to as the signal. The 'visibility' of the Higgs resonance above the (continuous) background is usually expressed in terms of the significance. This entity is here defined as the number of 'signal' events divided by the square root of the number of 'background' events. A resonance peak with a significance of 7 is  $7\sigma$  above the background.

The following section deals with Higgs boson physics; the creation and decay of Higgs bosons is discussed, as well as the experimental signatures in the intermediate mass range. In section 6.3 an overview is given of the early studies on the significance of the Higgs decays in ATLAS. The focus is on the tasks of the inner detector, that are summarised in the last section.

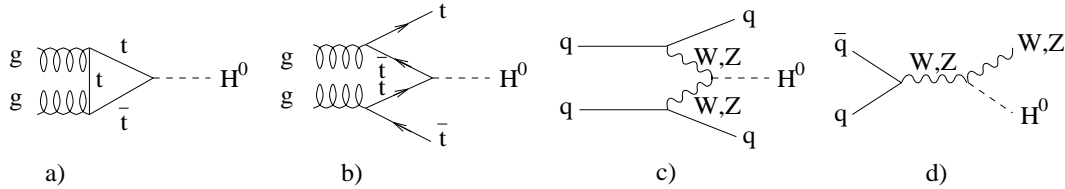


Figure 6.1: The production of a Higgs boson through four channels: a) gluon-gluon fusion; b)  $t\bar{t}$  fusion; c)  $WW$  and  $ZZ$  fusion; d)  $W$  and  $Z$  bremsstrahlung.

## 6.2 Higgs physics

### 6.2.1 Creation and decay of a Higgs boson

At the Large Hadron Collider, the Higgs boson is predominantly produced via the four mechanisms shown in figure 6.1 [81]. The first mechanism, gluon-gluon fusion, is dominant in almost the full studied mass range of  $H^0$ . The cross section for  $t\bar{t}$  fusion is 1–2 orders of magnitude lower, so its occurrence is too low to exploit the process for Higgs discovery.  $WW$  and  $ZZ$  fusion can play a significant role when Nature turns up with a heavy Higgs boson. Associated production of the Higgs boson through  $W$  or  $Z$  bremsstrahlung is important in the experimentally difficult region  $m_H < 130$  GeV. The production cross section and event rate for Higgs creation through these channels is given in figure 6.2. Note that the top mass

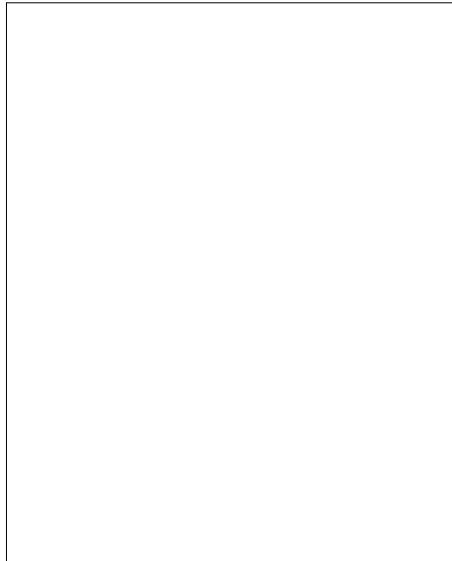


Figure 6.2: Production cross sections of the Standard Model Higgs boson through the four dominating channels (at a 16 TeV proton-proton collider) [81].

had not been pinned down when this figure was made.

The observation of all creation mechanisms but the gluon-gluon fusion is made easier

because the Higgs boson is accompanied by two quarks or an intermediate vector boson. This leads to a very typical signature: the Higgs boson is accompanied by two jets or a lepton pair, and the topology of this type of event can be used as a constraint when selecting events, such that most of the background is suppressed.

For the intermediate mass Higgs boson below 130 GeV, the probability of associated production is extremely low. Assuming  $m_H=110$  GeV we expect to see 18 events from the channels  $WH \rightarrow \ell\nu\gamma\gamma + X$  and  $t\bar{t}H \rightarrow \ell\gamma\gamma + X$ , during one year when running at nominal luminosity<sup>1</sup>. But on the other hand, the striking topology of these events makes the background very small: one expects only 7 background events in the same energy range [82, 65]. So one could call it unfortunate that the dominant channel of Higgs production, gluon-gluon fusion, does not produce accompanying particles, other than the unobserved proton remnant jets that always occur in deep-inelastic collisions.

Like the creation of the Higgs boson, its decay modes are determined by its coupling to mass. It tends to decay into the heaviest particles allowed, as can be seen from figure 6.3. The

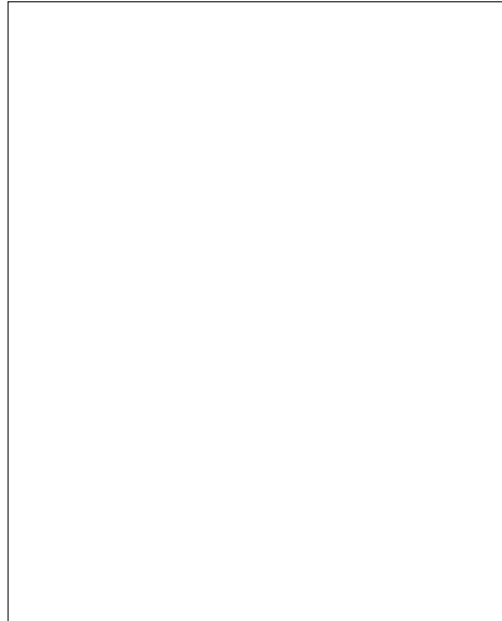


Figure 6.3: *The decay branching ratios of the Higgs boson as a function of its mass [81].*

decay into gluons and into photons is a higher-order process via a top-loop just as the Higgs production with gluon-gluon fusion. Below  $m_H=150$  GeV, the particle decays predominantly into bottom quark pairs and tau lepton pairs. At higher masses, the threshold for a decay into a  $W^+W^-$  pair is passed, and a little further, also the  $ZZ$  threshold. The intermediate vector bosons decay in their turn, the  $W$  into two different quarks or a  $\ell\nu$  pair; and  $Z$  bosons into  $e^+e^-$ ,  $\mu^+\mu^-$ ,  $\tau^+\tau^-$ ,  $\nu\bar{\nu}$  or  $q\bar{q}$ . For the identification of the Higgs boson we rely on the

<sup>1</sup>The symbol  $\ell$  is used to denote any of the particles  $\mu^+$ ,  $\mu^-$ ,  $e^+$  and  $e^-$ . It is not uncommon to talk about the decay of the Higgs boson into four leptons, even though the tau and neutrino channels are disregarded.

correct reconstruction of this decay, starting with the observable particles. For many decay channels, like the decay  $H \rightarrow ZZ^* \rightarrow \nu\bar{\nu} q\bar{q}$ , the reconstruction of the event is difficult and the background overwhelming. Only a few channels may provide a handle to look at the Higgs boson. The cleanest decay mode is when the Higgs boson decays into two Z bosons that decay into muons or electrons:  $H \rightarrow \ell^+ \ell^- \ell^+ \ell^-$ . Over the studied range of  $m_H$ , the Higgs mass resolution is comparable in the electron and muon channels.

### 6.2.2 Event rate and topology of the $H \rightarrow ZZ^* \rightarrow \ell^+ \ell^- \ell^+ \ell^-$ decay

Although the decay of the intermediate mass Higgs boson into two Z bosons has a branching ratio of 3–20%, the occurrence of  $H \rightarrow \ell^+ \ell^- \ell^+ \ell^-$  is very low due to the small branching ratio for  $Z \rightarrow \ell^+ \ell^-$  (6.5%). The cross section for production of a Higgs boson and the branching ratio for decay into four 'leptons' (e or  $\mu$ ) is shown in table 6.1.

$m_H$ (GeV)	130	140	150	160	170	180
$\sigma$ (pb)	28.3	25.9	24.0	22.4	21.2	20.4
BR( $H^0 \rightarrow ZZ^*$ )	0.032	0.059	0.074	0.034	0.021	0.062
Events $H^0 \rightarrow \ell^+ \ell^- \ell^+ \ell^-$	383	646	750	322	188	534

Table 6.1: Production cross sections and branching ratios for the Higgs creation and decay in the intermediate mass region, and the number of  $H^0 \rightarrow \ell^+ \ell^- \ell^+ \ell^-$  events expected in one year of LHC running at nominal luminosity. Taken from [83].

If  $m_H \gtrsim 200$  GeV, the topology of  $H \rightarrow ZZ \rightarrow \ell^+ \ell^- \ell^+ \ell^-$  is striking. Both Z bosons are on-shell so that each lepton pair has an invariant mass of  $m_Z$ . When the lepton momenta and directions are measured accurately, this allows a stringent cut on the kinematics of four-lepton events, such that only the irreducible (non-resonant) background of direct ZZ production is significant [84].

In the intermediate mass region  $130 < m_H < 200$  GeV, the topology is different, because one of the Z bosons is off-shell (virtual): the process is denoted  $H \rightarrow ZZ^* \rightarrow \ell^+ \ell^- \ell^+ \ell^-$ . One of the lepton pairs will have an invariant mass  $m_Z$ , while the other has a lower invariant mass. The selection of this type of events is therefore less stringent, so that more background events pass the criteria.

The leptons from a Higgs decay are biased to low  $\eta$ . This can be seen in figure 6.4 (created with the PYTHIA event generator [85] version 5.7), where the distribution of all four leptons over  $\eta$  is given, as well as the rapidity of the lepton closest to the beam axis. The figure shows, that a detector should cover the region  $|\eta| < 5$  to detect all four leptons from the Higgs decay. A practical detector arrangement will not reach this coverage. ATLAS measures electrons out to  $|\eta| < 2.5$  and muons to  $|\eta| < 2.8$  while CMS covers out to  $|\eta| < 2.5$  for electrons and  $|\eta| < 2.7$  for muons. This results in an inefficiency for Higgs events.

Similarly, not all leptons will be reconstructed: apart from a global tracking inefficiency, the leptons with a very low momentum will not be reconstructed for practical reasons (the

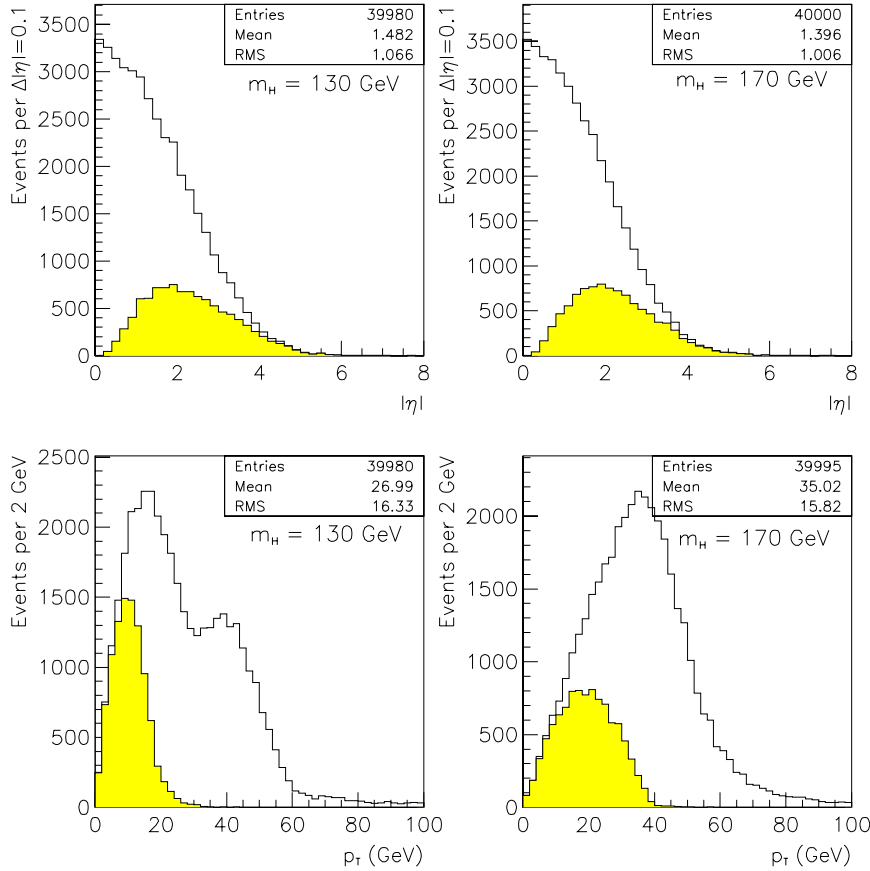


Figure 6.4: *Top figures: the rapidity distribution of the four leptons emerging from an intermediate mass Higgs decay (open histogram), and the rapidity of the outermost of the four leptons (shaded histogram), for two Higgs masses. Lower figures: the  $p_T$  distribution of these four leptons, and of the lowest- $p_T$  lepton in the event (shaded histogram).*

minimum bias background contains a large amount of obscuring low-momentum charged tracks, and furthermore these tracks are more difficult to reconstruct than high-momentum tracks). Generally, a cut at  $p_T = 5\text{--}10$  GeV is assumed. The lower two figures of figure 6.4 show the (transverse) momentum distribution of the leptons, and the transverse momentum of the lowest- $p_T$  lepton in an event. The Higgs event acceptance is shown in figure 6.5 as a function of both the  $p_T$ -cut and the rapidity coverage. With the ATLAS experiment, a reconstruction of all muons with  $p_T > 5$  GeV and electrons with  $p_T > 7$  GeV is foreseen. In CMS the muon threshold is also 5 GeV, but electrons are reconstructed if  $p_T > 10$  GeV. For both experiments only the  $p_T$ -cut and  $\eta$ -coverage lead to a Higgs acceptance around 55% at  $m_H = 130$  GeV and 75% at  $m_H = 170$  GeV.

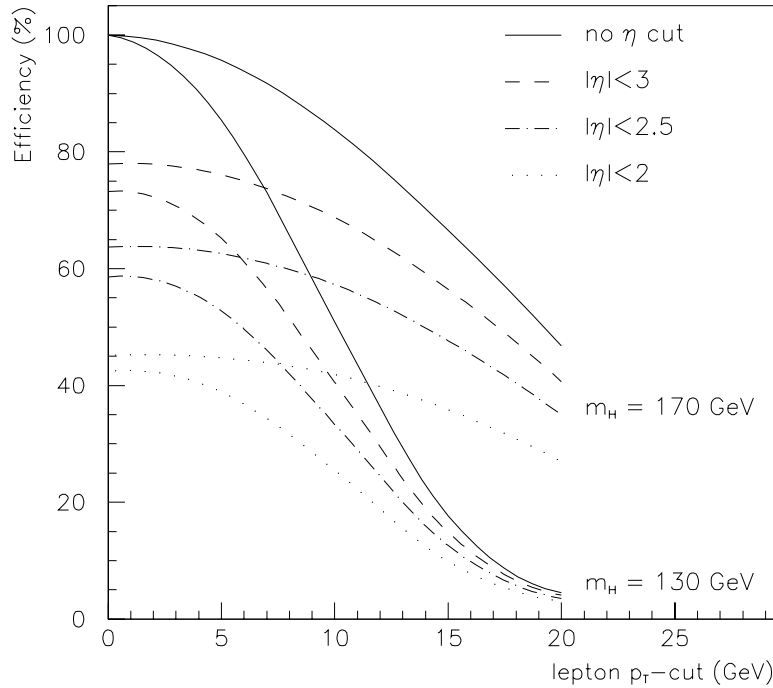


Figure 6.5: The acceptance of an experiment for  $H \rightarrow ZZ^* \rightarrow \ell^+ \ell^- \ell^+ \ell^-$  decays as a function of the  $p_T$ -threshold for charged particles and the  $\eta$ -coverage of the detector, for two  $m_H$  values.

### 6.2.3 Background to the $H \rightarrow \ell^+ \ell^- \ell^+ \ell^-$ decay

At an LHC proton-proton experiment, the observability of the signal from  $H \rightarrow \ell^+ \ell^- \ell^+ \ell^-$  depends on the quality of the experimental setup, and the background from other processes giving the signature of 4 leptons. The particle identification power of the LHC experiments is generally assumed to be sufficiently good to have a negligible background from fake muon and electron candidates to the particular case of the Higgs boson decaying into four leptons: the coincidence of four fake leptons, or a combination of fake and true leptons, is very low. The background to this physics signal is therefore limited to sources of true leptons. The main background process is the creation of a top quark pair decaying into leptons:

$$t\bar{t} \rightarrow b W^+ + \bar{b} W^- \rightarrow \ell^+ \ell^- \ell^+ \ell^- + X \quad (6.1)$$

and, also through their decay into leptons and other particles, the creation of  $Zb\bar{b}$  and the direct production of  $ZZ^*$ . Note that these backgrounds do not show the typical resonant behaviour we expect from the Higgs signal. On top of a continuous background, the Higgs boson should be seen as a significant peak.

The two background channels with bottom quark decay can be suppressed strongly using topology restrictions on the event. The lepton created in a quark decay tends to have the same direction as the resulting jet. So most of this background can be suppressed with the requirement that the lepton should not be accompanied by a jet ('lepton isolation'). We shall

return to this topic in section 6.3.3. Also, we can constrain the invariant mass of one of the two lepton pairs to equal the mass of the Z boson, and one could look for an impact parameter to identify leptons from bottom quark decay [90].

The background from direct  $ZZ^*$  production cannot be suppressed with this type of method: the event topology is of course very similar to the topology of the signal. This channel is a source of irreducible background. Several studies on the signal and background for the gold-plated Higgs decay at the LHC are compiled in the following section.

## 6.3 The observability of $H \rightarrow \ell^+ \ell^- \ell^+ \ell^-$

### 6.3.1 Introduction

The Higgs decays in the region  $80 \text{ GeV} < m_H < 1 \text{ TeV}$  can be regarded as benchmark processes to set the design goals for the experimental arrangement at an LHC collider experiment [6]. This is one of the reasons why the channel has been studied to great detail in an early stage of the LHC project: the first major results were presented in a workshop in Aachen, Germany, in 1990 (compiled in [12]). It then became clear that a major effort was needed to search the Higgs boson in the region  $80 < m_H < 130 \text{ GeV}$ , for which excellent electromagnetic calorimeters are indispensable (for  $H \rightarrow \gamma\gamma$ ). The mass range  $130 < m_H < 700 \text{ GeV}$  does not impose such severe conditions to the experimental equipment, because the clear signature of the gold-plated decay makes life easier. Yet, the inner detector information is vital for the study of Higgs decays in this mass range. At the low end of this mass range, the inner detector plays an important role in determining the lepton momenta (because low momentum muons suffer from multiple scattering in the calorimeters, and the energy of low momentum electrons is not measured well in a calorimeter). It assists in the selection of candidate events for  $H \rightarrow e^+ e^- e^+ e^-$ , by providing a means to distinguish jets and photons from electrons.

In this section, the results published by Della Negra *et al.* [83], Nisati [84], a study for the CMS Letter of Intent [86] and various studies by ATLAS collaborators [87]-[91] are reviewed, to define the tasks of the inner detector for the discovery of the intermediate mass Higgs boson. It should be noted that the large discrepancies between results achieved with different event generators set a scale of the error on this type of predictions: with the uncertainty of the gluon distribution in the proton, different models produce up to a factor 2 different cross sections for  $gg \rightarrow H$ . Estimates of the total cross section for  $b\bar{b}$  production vary from 100 to 700  $\mu\text{b}$  [92]! Also with the better knowledge of the gluon density obtained from measurements at HERA [93], the computed cross section for  $b\bar{b}$  production has a large uncertainty due to theoretical limitations. So even though extensive studies of the Higgs signal and background are very valuable for the design and understanding of a detector, one should keep this overall uncertainty in mind, especially where signal significances are quoted.

### 6.3.2 Tracking efficiency

The efficiency to find a track in the tracking detectors enters as a crucial parameter in the gold-plated Higgs decay, because when we require to see the four leptons, the tracking efficiency

comes in to the fourth power. This can be a major cause of signal loss. In early studies, a global tracking inefficiency of 10% was assumed, leading to an acceptance of 65.6% of the Higgs events. Clearly the inefficiency should not exceed the 10% level. This is not an easy design goal in itself. One can best build the detector with safety margins ('robustness'), where for instance the accidental (hopefully temporary) loss of one module of the inner detector does not degrade the detector performance as a whole drastically. Still, it is very difficult to estimate the level of robustness needed to build a reliable detector.

There is one fundamental criterion that any inner detector should meet: when everything works as designed, the resulting tracking efficiency must be safely above the minimum tolerable efficiency. In the case of electron tracking, this requirement is not easily met. The ATLAS inner detector consists of many modular detectors, each supported with frames and serviced with cooling pipes and cables, all leading to quite a large amount of material within the tracking region. Electrons may be affected by this material, particularly through the process of bremsstrahlung. The emitted photon is collinear with the direction of motion of the electron. In the ATLAS inner detector, an electron will lose typically 40% (at  $0.50 X_0$ ) of its energy through this process, before it enters the electromagnetic calorimeter. Most of this energy is still seen in the calorimeter because the photons will also cause an electromagnetic shower, but the problem with electron bremsstrahlung is, that the charged particle track does not follow a perfect helix anymore (as the energy of the electron decreases, it will follow a trajectory with a smaller radius of curvature) and the electromagnetic shower will be irregularly shaped (because the impact point of the radiated photons and the electron itself are separated). In an extreme case, the electron loses close to all of its energy and it cannot be recognised as an electron.

The topic of electron tracking in an LHC experiment is discussed into great extent in reference [75], for a generalised setup of discrete tracking detectors. In this paper, it was shown that the problem of bremsstrahlung is only severe when the electron energy is low: in that case, the particle will bend strongly, and the impact points of the electron and its radiated photons are separated (in  $r\phi$ ). The analysis algorithm presented in that paper lost 6.5% of the 10 GeV electrons (in a tracker containing  $0.50 X_0$  of material), dominated by the problem of bremsstrahlung. At 20 GeV the tracking efficiency passes the 95% level. These numbers were derived without using the hit information of the TRT. Since the release of this paper, members of the ATLAS collaboration have worked on an improvement of the presented tracking algorithm, where the bremsstrahlung information in the calorimeter is used to correct for a kink in the helix found in the tracker. The current estimate, presented in [67], is that the electron tracking efficiency is 95.9% at  $p_T = 20$  GeV, using also the TRT information. With a normal helix fit and a sensible cut on  $\chi^2$ , the tracking efficiency is only 82.2%.

The conclusion in the latter paper [67] was, that the problem of electron bremsstrahlung does not affect the ultimate goal, the measurement of  $m_H$ , because after event selection the invariant mass of the four electrons is determined from calorimeter information only. However, for low momentum electrons the inner detector could give a better momentum and position resolution (the calorimeter is better roughly above 10 GeV at  $\eta=2.5$  to 30 GeV at  $\eta=0$ ). Adding the inner detector measurement to the computation of the Higgs mass can improve the Higgs mass resolution by up to 20% (at  $m_H = 130$  GeV).

### 6.3.3 Lepton isolation

To distinguish leptons from a  $Z^0$  decay from those from quark decays, the isolation requirement is very effective. One can require a lepton to be isolated in the inner detector, which implies that no charged particles are found within a certain radius around the lepton. The optimum radius depends on the probability of random occurrences and the topology of the quark decay; at nominal luminosity, an ATLAS study [88] shows that the tracking isolation cut should be applied in a cone with dimensions  $\Delta\eta \times \Delta\phi = 0.4 \times 0.4$ . For this cut to be successful, a low ghost-track rate should be achieved. Early studies of the track finding in the TRT show that the ghost track rates are indeed negligible [94]. The ghost rates in the precision detectors are also very low, so the combination of the two will almost rule out ghost tracks. Independently, one can require that there is no activity in the hadronic calorimeter around the lepton. The same cone dimensions give a good separation between leptons from quark decays and leptons from other sources. The isolation requirement is most effective in the inner tracker.

The effect of an isolation cut (with isolation required in the inner detector and in the calorimeter) is clearly shown in figure 6.6, where a hardly significant Higgs resonance (top figure) is discriminated effectively against the background. A top mass of 140 GeV was assumed. The isolation cut increases the statistical significance with a factor 2 over the mass range  $130 < m_H < 180$  GeV. This significance improvement is also seen in a similar study for CMS, presented in [86]. Still, the effectiveness of these cuts depends on the experimental setup and the analysis algorithm, so it is important to perform a detailed study using a full detector simulation.

### 6.3.4 Direction and momentum measurement

A CMS study [86] shows, that their inner detector plays an indispensable role in the detection of muons from the intermediate Higgs. Without the inner tracker information, it was shown that in the CMS geometry the Higgs signal is almost lost. This can be seen in figure 6.7 where the reconstructed Higgs mass is plotted with the background, with and without the inner tracker information. For the reconstruction of the event,  $p_T$ ,  $\eta$  and  $\phi$  of each lepton should be known. For low-momentum muons these three observables get spoiled by energy loss and multiple scattering in the calorimeter, and in the CMS experiment the shape of the magnetic field causes a fast deterioration of the bending power with increasing  $|\eta|$ , which results in a weak muon momentum measurement in the muon system for the combination of high  $p_T$  and high  $|\eta|$ . For the ATLAS experimental setup, a comparable simulation is not yet performed. A momentum resolution comparison between the two, presented in [95], shows that the stand-alone performance of the ATLAS muon system is much better, except for  $p_T > 500$  GeV at  $|\eta| < 0.8$ . This implies that in the ATLAS experiment a signal breakdown as serious as in figure 6.7b will not occur.

The inner detector supplies the best muon momentum measurement only for muon transverse momenta below 10 GeV at  $|\eta|=2$  to 30 GeV at  $|\eta|=0$ .<sup>2</sup> The  $\eta$  and  $\phi$  measurements of

---

<sup>2</sup>These numbers were determined as follows: with a GEANT routine, the energy loss fluctuations in 12  $\lambda_I$  of iron were calculated. The RMS value of these fluctuations was added in quadrature to the momentum

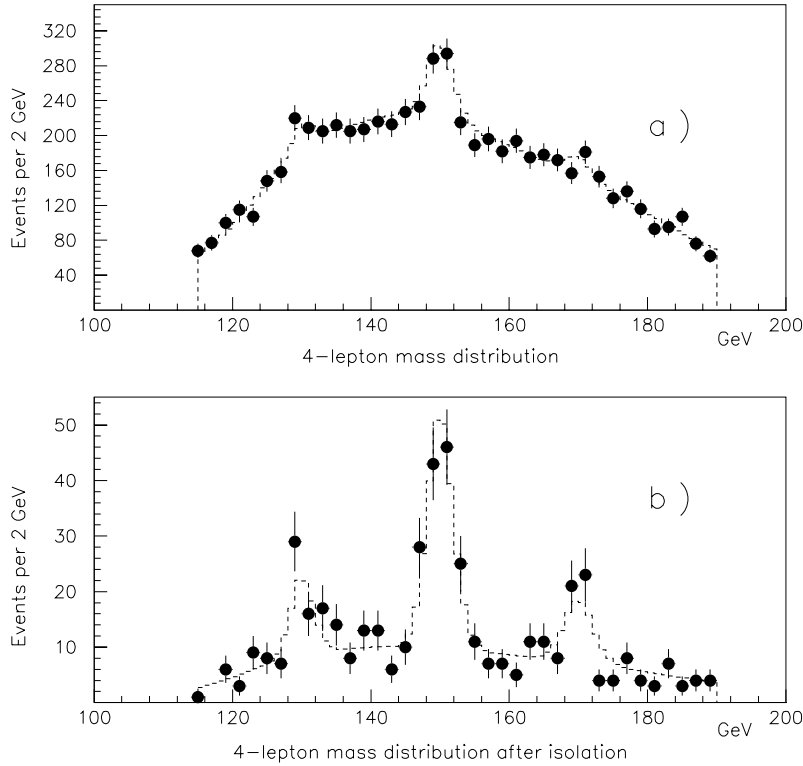


Figure 6.6: The simulated signal from the Higgs boson, here overlaid for three different masses ( $m_H = 130, 150, 170$  GeV), should be seen as a resonance in this histogram of the invariant mass of the four reconstructed leptons. Without any topology constraint, only the 150 GeV Higgs boson can be seen with sufficient significance. When isolation of the leptons is required, we lose a great deal of the  $t\bar{t}$  and  $Zb\bar{b}$  backgrounds and the boson becomes clearly visible in all three cases. Taken from the ATLAS Letter of Intent [65].

muons are superior in the inner detector below  $\sim 50$  GeV, with  $\sigma_\theta < 1$  mrad and  $\sigma_\phi \ll 1$  mrad, which is sufficiently good not to contribute significantly to the mass resolution of the Higgs boson.

Although the precise measurement of low-momentum leptons helps in the reconstruction of an intermediate-mass Higgs boson, this is not a benchmark process to define the momentum resolution, because given the resolution of the electromagnetic calorimeter and the muon spectrometer, the mass resolution is satisfactory also without this precision enhancement.

In the intermediate mass range, the electron direction and momentum are measured most accurately by the electromagnetic calorimeter, except at low lepton energy and when an early bremsstrahlung occurs. For  $H \rightarrow e^+e^-e^+e^-$ , the most important task of the inner detector is the determination of the electron charge, and the momentum to identify the electron via a match of  $E$  and  $p$ .

---

resolution of the outer muon system.

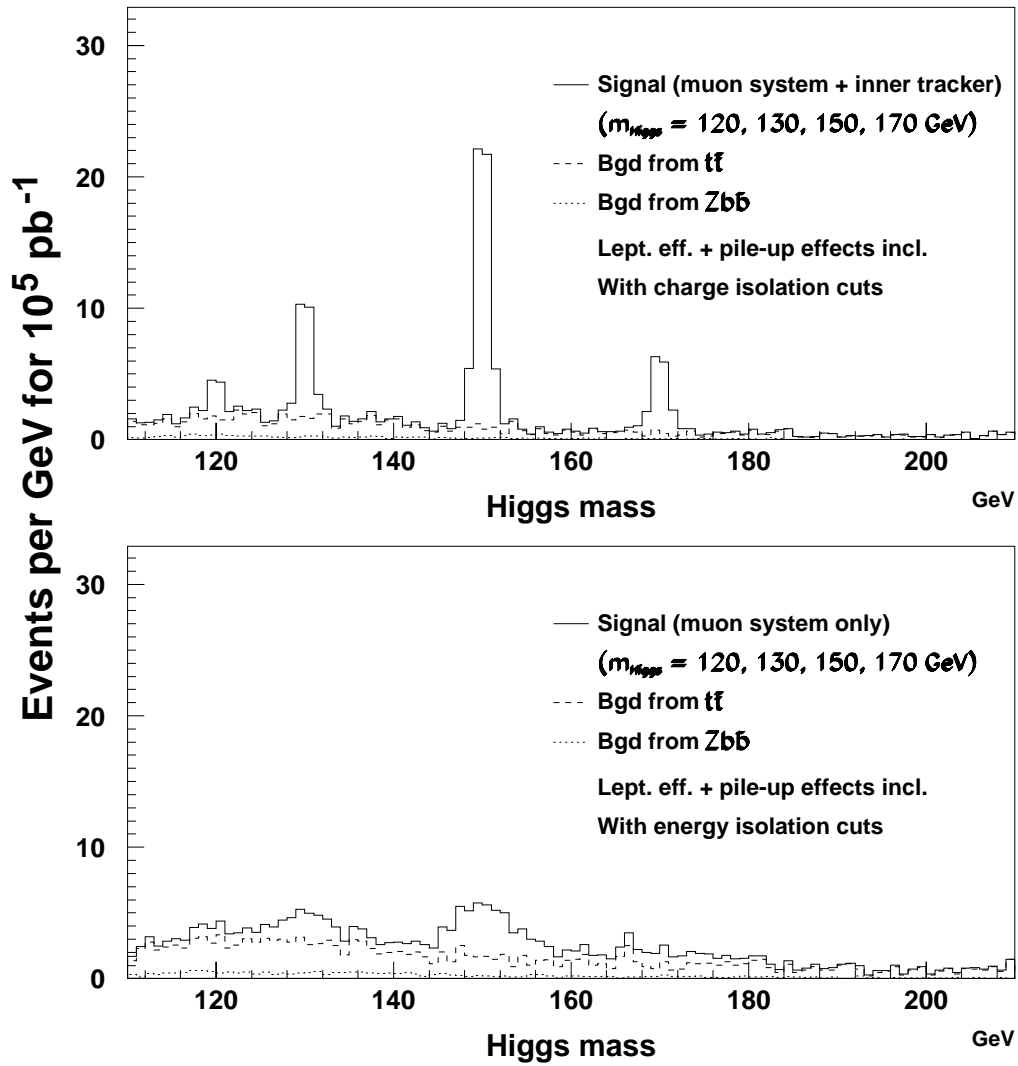


Figure 6.7: The simulated signal of a Higgs boson with mass 120, 130, 150 and 170 GeV, decaying into four muons in the CMS detector. The upper figure shows the  $Zb\bar{b}$  background (dotted line), the  $Zb\bar{b}$  and  $t\bar{t}$  background (dashed line), and the signal plus background (solid line), from a reconstruction in the inner and outer trackers. The lower figure shows the same histogram, when the Higgs mass reconstruction is attempted with only the muon system information. The figure was kindly provided by H. Plochow-Besch.

## 6.4 The role of the MSGC tracker for $H \rightarrow ZZ^* \rightarrow \ell^+ \ell^- \ell^+ \ell^-$

From the previous section we can conclude that the MSGC tracker will be used specifically for four tasks in the search for an intermediate-mass Higgs boson:

- **Momentum measurement:** the inner detector provides the best measurement of lepton momenta up to  $p_T = 30$  GeV in the barrel. In the forward region this threshold momentum goes down to 10 GeV, roughly. The momentum measurement of the inner detector can therefore be regarded mainly as providing robustness, and as a means to identify electrons by an  $E/p$  match.
- **Muon direction measurement:** the inner detector should measure  $\theta$  and  $\phi$  for muons to an accuracy of order 1 mrad.
- **Tracking efficiency:** the efficiency of muon and electron tracking will determine the Higgs event acceptance, and should be of the 90% level or better. The recovery of electrons with large bremsstrahlung loss need special attention in the analysis.
- **Lepton isolation:** the requirement of lepton isolation should effectively identify leptons from Z-decays, as opposed to leptons from quark decays. This does not translate into an inner detector requirement other than that there should be no ghost tracks.

The MSGCs are adequate detectors to fulfill the above tasks, if we achieve very good control over the alignment of the inner tracker and the detectors work up to the specifications. These two requirements determine the goals of the last preparation phase, before the detector assembly starts. Contacts with industry are being established for the mass production of MSGC substrates, and a substrate test arrangement is under design. A prototype MSGC wheel is under construction, which will be used to study the assembly, servicing, and alignment procedures, and to determine the mechanical properties. The MSGCs in this prototype wheel, and its data acquisition, will also be tested by placing the object in a test beam at CERN. A test is underway to see if the heat produced by the front end electronics will be efficiently transferred to the cooling system. The development of the Fastplex front end chip, dedicated to the MSGC readout at the LHC, is progressing steadily. So far, the progress has been very close to schedule, and installation of the MSGC tracker in the ATLAS pit is foreseen in 2001. Still, the most challenging unresolved issue is that of radiation hardness. Most groups involved in MSGC R&D are now focusing their attention on radiation hardness tests in search of a robust and practical combination of substrate and gas mixture.

The goal of the two proton-proton experiments is to discover the Standard Model Higgs boson (if it exists) within one year when running at nominal luminosity. The simulations indicate that we may reach this goal, if the cross sections are well estimated. As the Higgs discovery potential over the full mass range is very similar for the CMS and ATLAS experiments, we can expect an extremely exciting period after the turn on of the LHC machine.

# Acknowledgements

Four years ago, when I received my Master's degree, I had difficulty in finding my place in the massive field of High Energy Physics. Jos Engelen has helped me greatly with his unconditional support and good advice. In the year that followed, I worked in the instrumentation laboratory under supervision of Fred Hartjes and Fred Udo, with Michiel Geijsberts, Han Pannekoek and (later) Fons de Winter. It was a great pleasure to work in this group, and it is in this period that we laid the basis for my further research. The many discussions on instrumentation I had with Harry van der Graaf, Gras van Apeldoorn and Henk Tiecke helped me to broaden my knowledge in this field.

With the development of a Monte Carlo simulation of the MSGC, I moved into the virtual reality of computing. Kors Bos would be my third supervisor. He did not like the word supervisor, so we decided to become friends. Working with him was always fun. I still hope we will go to Geneva by bike one day. Kors, Kees Daum and Jos Engelen commented on my thesis drafts in a very constructive and complementary way.

Bob van Eijk has been very stimulating to me. It was him who convinced me to finish this thesis with a chapter on a hypothetical particle. With Hoite Tolsma I spent both many hectic days and relaxing evenings, especially in Geneva and Evian, where we tried just about every drink except water. It was a pleasure to work with Ruud Kluit, Paul Rewiersma, Henk Schuijlenburg, and have lunch with Willem van Leeuwen, René Wilhelm and Els de Wolf.

In Geneva, I made friends without whom my time abroad would have been quite terrible: Michael Yurko, Tony Wildish and especially Maya Stavrianakou. Our dinners at the Trattoria are irreplaceable. I would like to thank also my other colleagues at CERN that helped me get this work done: Daniel Froidevaux, Slava Klyukhin, Andrea Dell'Acqua, Roger Clift, and last but not least Alan Poppleton, who patiently taught me very much about track reconstruction and collider physics in general.

Joining ATLAS linked the NIKHEF MSGC group to British institutes. It was a great pleasure to work with John Thompson, Steve Snow, John Baines, Rob Edgecock and Mike Esten, although it was only shortly. Not joining CMS did not prevent our very fruitful collaboration with Bruxelles. I enjoyed working with Catherine Vander Velde very much. I would like to thank all these people, and also my colleagues that I did not mention specifically.

During my Ph. D. work, Saskia Kooij has made sure I kept my social life to level, and guided me through the more difficult periods. Her love and patience helped me more than anything to reach this goal.



# Summary

High energy physics is the scientific discipline that deals with the tiniest building blocks of matter. Its study predominantly uses two types of apparatus: the particle accelerators, that perform the function of microscopes, and the particle detectors, that look at the particle trajectories. A steady technological progress in the development of these apparatus has given us access to more and more knowledge about the building blocks of matter. It turns out that all matter is composed of (seemingly) indivisible particles called fermions. They exchange forces, and sometimes change of nature, through the exchange of specific particles called bosons. One has been able to construct a model that describes the fermions and bosons and their interactions. This model, called the Standard Model, is briefly introduced in chapter 1 of this thesis. Computations made with this model give results extraordinarily close to observations.

However, to introduce mass and solve some problems with anomalous predictions of the model, the symmetry between electromagnetism and the weak interactions must be broken. In the Standard Model this is done through the Higgs mechanism, which results in the prediction of the existence of a new particle, the Higgs boson. This particle has never been observed. To investigate the mechanism of electroweak symmetry breaking, and specifically to look for the Higgs boson, a new particle accelerator will be built, the Large Hadron Collider. This bigger-than-ever microscope will allow us to see even smaller structures than before, and also to create heavier elementary particles than we ever observed. It allows the discovery of the Higgs boson if it exists.

Building the Large Hadron Collider involves a major technological effort. Besides that, to study the collision processes at this accelerator we also need new particle detectors. The development of new particle detection techniques is an endeavour spread all over the world. At NIKHEF, research focuses on two new detectors: the Honeycomb Strip Chamber, and the Microstrip Gas Counter. This thesis is devoted to the latter detector. The device consists of two metal plates, separated by a layer of gas. When a charged particle crosses this layer of gas, it ionises gas molecules along its way. One of the metal plates is very sensitive to the liberated electrons. The other metal plate is held at a strong negative voltage, so that it pushes the liberated electrons towards the sensitive plate. The crossing of a charged particle is thus registered by the sensitive plate. In chapter 2 of this thesis, the operation of the Microstrip Gas Counter is discussed in detail. An essential feature of the detector is the fact that the sensitive plate is segmented (into the so-called microstrips), so that the location of a crossing particle can be determined. The accuracy of the location measurement, the position

resolution, is approximately  $30 \mu\text{m}$ .

The understanding of the Microstrip Gas Counter is based on extensive tests with various prototypes. The third chapter briefly describes these measurements. The research focuses partly on the characteristic properties, such as position resolution, efficiency, and signal speed. A second topic of study is, how the detector can be used in real nuclear and high energy physics experiments; various geometries are tried out, and the issue of signal processing is addressed. Thirdly, it is of great importance how well the detector performs after a long irradiation. Between different prototypes, huge differences in life time have been observed. The understanding of these differences is crucial because only a few prototypes have proved suitable for the use at an LHC experiment so far. A last topic of study is the optimisation of the gas mixture used in the Microstrip Gas Counter. In the article reprinted at the end of this chapter, various gas mixtures are compared for this purpose.

In chapter 4, a computer model of the Microstrip Gas Counter is described. It was developed to better understand the detector, and to predict the detector properties under various conditions without having to build a new experimental arrangement for each situation. To gain confidence in such a computer model, it should be subjected to many tests, where the model prediction is compared to real measurements. Comparisons to a test in a 4 GeV pion beam and to cosmic ray measurements are presented. The model matches the pion beam data very well, but there are discrepancies between the model and the cosmic ray measurements in the predicted pulse height distributions. This is probably due to the coarse parametrisation of the ionisation process in the Monte Carlo. The Monte Carlo model is used to predict the detector characteristics under various circumstances. In this thesis, the emphasis is on the position resolution of the device for different geometries. The simulation indicates that the position resolution can be improved to  $20 \mu\text{m}$  by a change in the geometry. Finally, a study of the combination of the MSGC with two preamplifiers is presented at the end of chapter 4. It shows that an integrator produces a significantly larger signal than the commonly used shaper when the shaping time must be short.

After this discussion of the Microstrip Gas Counter, we return to the Large Hadron Collider. In chapter 5, the ATLAS experiment is introduced, which is one of the two experiments that will be devoted to the search for the Higgs boson at the LHC. The design of the inner part of this experiment is discussed in great detail, because here Microstrip Gas Counters are applied. The design is determined to a large extent by the goal of efficient electron identification. For this purpose, a transition radiation detector will be incorporated in the inner detector, which constrains the design of the rest of the inner detector.

Finally, in chapter 6 the question is addressed, how to find the Higgs boson in such an experiment. After a general overview of the predicted behaviour of the Higgs boson, the method of Higgs mass determination is discussed, and results from computer simulation studies are presented for the Higgs mass range between  $m_Z$  and  $2m_Z$ . These studies show that the Higgs signal can be seen as a very significant resonance in this mass range, although the theoretical errors are large. The Microstrip Gas Counters will be actively used in the search for this Higgs boson: they will be used for the determination of the direction and momentum of some of the Higgs decay products, and they will aid in the distinction between Higgs decay products and heavy quark decay products through an isolation requirement.

# Samenvatting

De hoge energiefysica is de discipline waarin de kleinste samenstellende deeltjes van de materie worden onderzocht. In dit vakgebied staan twee soorten apparaten centraal: enerzijds de deeltjesversnellers, die de functie van microscopen vervullen, en anderzijds de deeltjesdetectoren, die als ogen op de bestudeerde processen gericht staan en ons vertellen welke deeltjes ontstaan en vergaan, en hoe. Dankzij een gestage technologische vooruitgang van deze twee hulpmiddelen zijn we steeds meer over de bouwstenen van de materie te weten gekomen. Het blijkt dat alle materie opgebouwd is uit schijnbaar ondeelbare eenheden die we fermionen noemen. Deze deeltjes zijn onmeetbaar klein maar manifesteren zich toch duidelijk. Ze wisselen krachten uit, en veranderen soms van aard, via specifieke deeltjes die we bosonen noemen. Hoewel de opbouw van de materie uit deze bouwstenen ons nog voor vele raadselen plaatst, is het mogelijk gebleken voor de deeltjes en hun krachtenspel een wiskundig model op te stellen. In hoofdstuk 1 van dit proefschrift wordt dit model, het zogeheten Standaardmodel, kort ingeleid. De berekeningen die we met dit model kunnen maken, komen in het algemeen heel dicht bij de werkelijkheid, zoals we die bestuderen met de deeltjesversnellers en de deeltjesdetectoren.

Echter, in het model komt een deeltje voor dat nooit is ontdekt, het Higgs-boson. Dit deeltje is van vitaal belang: het geeft massa aan de andere deeltjes. Om dit deeltje te vinden zal een nieuwe versneller gebouwd worden, de Large Hadron Collider (grote hadronbotser), die ongeëvenaard kleine structuren kan laten zien, en tevens zwaardere elementaire deeltjes kan maken dan we ooit hebben waargenomen. Mochten we hiermee het Higgs-boson niet vinden, dan weten we met grote zekerheid dat het niet bestaat, en dan moet het model aangepast worden. In dat geval biedt deze grote hadronbotser de mogelijkheid om de werkelijke situatie verder te onderzoeken.

De realisatie van de Large Hadron Collider zal een grote stap voorwaarts betekenen in de technologie van deeltjesversnellers. Echter, de tegenwoordig toegepaste deeltjes*detectoren* zijn voor het bekijken van de processen bij de Large Hadron Collider niet geschikt. In heel Europa is om die reden onderzoek gestart naar nieuwe methoden van deeltjesdetectie. In Nederland wordt onderzoek verricht aan de Honeycomb Strip Chamber, en aan de Microstrip Gas Counter. Aan de laatste is dit proefschrift gewijd. Het is een apparaatje bestaande uit twee metalen vlakken die gescheiden zijn door een laagje gas. Wanneer een geladen deeltje door dit laagje gas beweegt, stoot het af en toe een elektron los van een gasmolecuul. Van de metaalvlakken is er één buitengewoon gevoelig voor deze losgestoten elektronen. Het andere metaalvlak is op een sterk negatieve spanning gezet zodat de elektronen naar het

gevoelige oppervlak geduwd worden. Het gevoelige vlak registreert op deze manier indirect dat een geladen deeltje door het gaslaagje is gekomen. In hoofdstuk 2 van dit proefschrift wordt de werking van deze detector uitvoerig besproken. Een essentieel facet van de detector is dat het gevoelige metaalvlak gesegmenteerd is (opgedeeld in de zogeheten microstrips), waardoor van een passerend deeltje de plaats geregistreerd kan worden. De segmentatie bepaalt hoe nauwkeurig de positie van het deeltje bepaald kan worden. Deze nauwkeurigheid, het plaatsoplossend vermogen, is ruwweg  $1/30$  millimeter.

Het derde hoofdstuk bespreekt allerlei metingen die in laboratoria zijn uitgevoerd om zoveel mogelijk te weten te komen over de detector, zoals de vraag hoe vaak de detector een voorbijkomend deeltje waarneemt en hoe vaak hij het mist. Deze eigenschappen moeten goed in kaart gebracht worden om de toepassing van de detector in een experiment te kunnen afwegen. In het artikel dat hoofdstuk 3 afsluit, worden voor het gaslaagje verschillende gasmengsels vergeleken voor het gebruik in Large Hadron Collider-experimenten.

In hoofdstuk 4 wordt een computermodel van de Microstrip Gas Counter beschreven. Dit model werd ontwikkeld om een beter begrip van de detector te krijgen, en voorspellingen te kunnen doen over de detector in bepaalde situaties, zonder dat iedere situatie in werkelijkheid opgebouwd moest worden. Om vertrouwen te krijgen in een dergelijk model moet het uitvoerig getoetst worden aan de werkelijkheid. Deze toetsing wordt besproken in het hoofdstuk zelf en in het eerste artikel dat aan het eind is bijgevoegd. Daarnaast worden voorspellingen gedaan omtrent het plaatsoplossend vermogen bij verschillende keuzes van de geometrie van het apparaatje. Met behulp van de simulatie wordt aannemelijk gemaakt dat een verbetering van het plaatsoplossend vermogen tot circa  $1/50$  millimeter kan optreden door een iets andere keuze van de geometrie. Ook is de computersimulatie gebruikt om twee signaalversterkers te vergelijken, voor de toepassing van MSGCs in LHC-experimenten. Over dit werk wordt gerapporteerd in het tweede artikel aan het eind van hoofdstuk 4.

Na deze bespreking van de Microstrip Gas Counter komen we terug op de Large Hadron Collider. In hoofdstuk 5 is het ontwerp van het ATLAS-experiment aan de orde, een van de twee experimenten aan de Large Hadron Collider waarmee het Higgs-boson gezocht gaat worden. Het ontwerp van het binnenste gedeelte, waarin zich Microstrip Gas Counters bevinden, wordt uitvoerig toegelicht. Tenslotte wordt in hoofdstuk 6 een overzicht gegeven van studies naar het ontdekkingspotentieel van deze opstelling: hoe kunnen we met een dergelijke experimentele opstelling een Higgs-boson ontdekken? Na een algemeen overzicht van de verwachte gedragingen van het Higgs-boson wordt de taak van de binnenste detectoren samengevat, waarmee de functie van de Microstrip Gas Counters in dit experiment geïllustreerd wordt.

# Bibliography

- [1] F. Abe *et al.*, *Evidence for Top Quark Production in  $\bar{p}p$  Collisions at  $\sqrt{s} = 1.8$  TeV*, FERMILAB-PUB-94/097-E.
- [2] Particle Data Group, *Review of particle properties*, Phys. Rev. D45, S1 (1992).
- [3] The LEP collaborations, CERN-PPE/93-157.
- [4] G. Coignet, Talk given at the XVIth international symposium on lepton-photon interactions, Ithaca, New York, 1993.
- [5] F. Dawson *et al.*, *The Higgs Hunter's guide*, Addison-Wesley (1990).
- [6] G. Altarelli, *Proton-proton physics at the LHC: an overview*, CERN 90-10 (I) 153 (1990).
- [7] W. Wünsch, *TeV electron-positron Linear Collider Studies*, CERN Courier, September 1993, and private communication with the author.
- [8] The LHC study group, *The Large Hadron Collider Accelerator Project*, CERN/AC/93-03 (1993).
- [9] D. H. Perkins, *Introduction to High Energy Physics*, 3rd edition, Addison Wesley, Menlo Park 1987.
- [10] D. Froidevaux, *Experimental review of the search for the Higgs boson*, CERN 90-10 (II) 444 (1990).
- [11] J. Alcaraz *et al.*, *Higgs discovery potential of the L3 detector at LEP200*, CERN-PPE/93-28.
- [12] D. Denegri, *Standard Model physics at the LHC*, CERN 90-10 (I) 56 (1990).
- [13] E. N. Argyres *et al.*, *Compositeness*, CERN 89-10 (II) 805 (1989).
- [14] R. Bouclier *et al.*, *Development of gas micro-strip chambers for high rate radiation detection and tracking*, CERN DRDC 92-30 (P-41) (1992), and addendum, CERN DRDC 92-34 (1992).
- [15] G. Charpak *et al.*, Nucl. Instr. and Meth. 62 (1968) 262.
- [16] M.J. Neumann and T. A. Nunamaker, IEEE Trans. on Nucl. Sci. 17 (3) (1970) 43.
- [17] A. Oed, Nucl. Instr. and Meth. A263 (1988) 351.
- [18] P. Geltenbort, postscript to the proceedings of the Workshop on progress in MSPCs, Grenoble 1993.

- [19] R. Bouclier *et al.*, Nucl. Instr. and Meth. A332 (1993) 100.
- [20] RD-28 status report, CERN/DRDC/93-34 (1993).
- [21] E. J. Kobetich and R. Katz, Phys. Rev. 170 (2) (1968) 391.
- [22] A. V. Zarubin, Nucl. Instr. and Meth. A283 (1989) 409.  
R. Bouclier *et al.*, Nucl. Instr. and Meth. A283 (1989) 509.
- [23] F. Sauli, CERN 77-09 (1977).
- [24] F. M. Penning, Physica 1 (1934) 1028.
- [25] H. Fischle *et al.*, Nucl. Instr. and Meth. A301 (1991) 202.
- [26] A. Peisert and F. Sauli, CERN 84-08 (1984).
- [27] P. Rice-Evans, *Spark, Streamer, Proportional and Drift Chambers*, The Richelieu Press (1974).
- [28] K. Kleinknecht, *Detektoren für Teilchenstrahlung*, Teubner (1984).
- [29] S. A. Korff, *Electrons and nuclear counters*. Van Nostrand, New York 1946.
- [30] G. D. Alkhozov, Nucl. Instr. and Meth. A89 (1970) 155.
- [31] S. C. Curran *et al.*, Phil. Mag. 40 (1949) 929.
- [32] G. Smadja, talk given at the Fastplex meeting of 3 February 1993.
- [33] F. Angelini *et al.*, Nucl. Instr. and Meth. A335 (1993) 69.
- [34] F. Angelini *et al.*, IEEE Nucl. Sci. NS-37 (1990) 112.
- [35] F. Angelini *et al.*, CERN 90-10 (1990) 222.
- [36] F. Hartjes *et al.*, Nucl. Instr. and Meth. A310 (1991) 88.
- [37] C. Budtz-Jørgenson *et al.*, Nucl. Instr. and Meth. A310 (1991) 82.
- [38] J. Schmitz, Master's thesis, 1990.  
J. J. Florent *et al.*, Nucl. Instr. and Meth. A329 (1993) 125.  
S. Schmidt *et al.*, Nucl. Instr. and Meth. A 344 (1994) 588.
- [39] D. W. Kaandorp *et al.*, *The microstrip gas counter developed at NIKHEF-H for the SMC experiment at CERN*, NIKHEF-H technical report, December 1993.
- [40] S. Snow, *Comparison of algorithms for associating an MSGC signal to a beam crossover in ATLAS*, ATLAS INDET-NO-045.
- [41] J.A. Kadyk, Nucl. Instr. and Meth. A300 (1992) 436.
- [42] S. Brons *et al.*, Nucl. Instr. and Meth. A342 (1994) 411.
- [43] R. Bouclier *et al.*, CERN-PPE/94-63, submitted to Nucl. Instr. and Meth.

- [44] P. Savard *et al.*, *An a-Si:H gas microstrip detector*, Montreal preprint, July 1993.
- [45] S. Snow, talk given at the Workshop on progress in MSPCs, Grenoble 1993.
- [46] See for instance A. Oed *et al.*, Nucl. Instr. and Meth. A284 (1989) 223.
- [47] H. Stahl *et al.*, Nucl. Instr. and Meth. A297 (1990) 95.  
R. Bouclier *et al.*, Nucl. Instr. and Meth. A310 (1991) 74.  
R. Bouclier *et al.*, Nucl. Instr. and Meth. A315 (1992) 521.
- [48] J. H. Moromisato, Nucl. Instr. and Meth. A345 (1994) 90.
- [49] CERN courier, May 1992.
- [50] V. Eckardt, talk given at the Workshop on progress in MSPCs, Grenoble 1993.
- [51] P. Kuijer, talk given at the Workshop on progress in MSPCs, Grenoble 1993.
- [52] A. Oed, *Demande de brevet pour detecteur a gaz utilisant une anode a microbandes*, Patent no. 86 10810, France (25 July 1986).
- [53] S. Steinhäuser, talk given at the Workshop on progress in MSPCs, Grenoble 1993.
- [54] R.A.L. Microelectronics, MX5 preliminary specifications, September 1991.
- [55] R. Horisberger and D. Pitzl, Nucl. Instr. and Meth. A326 (1993) 92.
- [56] See ref. [46] and F. Udo, talk given at the RD28 meeting on 13 December 1993 at CERN, Geneva.
- [57] K. Bos, *DICE, a subroutine package for the ATLAS detector simulation*, to be published.
- [58] T. McMahon *et al.*, *Study of some factors influencing performance of gaseous micro-strip detectors*, submitted to Nucl. Instr. and Meth.
- [59] A copy of the program (in CAR format) can be retrieved by anonymous ftp to the nikhef server.
- [60] L. Katz and A. S. Penfold, Rev. Mod. Phys. 24 (1952) 28.
- [61] S.V. Starodubtsev and A. M. Romanov, *The passage of charged particles through matter*, p. 194; Tashkent 1962/Jerusalem 1965.
- [62] C. Feldman, Phys. Rev. 117, 455 (1960).
- [63] U. Fano, *Phys. Rev.* 72, 26 (1947).
- [64] J. Schmitz, Nucl. Instr. and Meth. A323 (1992) 638.
- [65] The ATLAS collaboration, *Letter of Intent for a General Purpose pp experiment at the LHC*, CERN/LHCC/92-4 (1992).
- [66] The CMS collaboration, *Letter of Intent for a General Purpose Detector at the LHC*, CERN/LHCC/92-3 (1992).
- [67] The ATLAS collaboration, *Progress Report on ATLAS Milestones*, CERN/LHCC/93-51 (1993).

- [68] The CMS collaboration, *Status Report and Milestones*, CERN/LHCC/93-48 (1993).
- [69] The ATLAS collaboration, *Progress Report on ATLAS Milestones*, CERN/LHCC/94-22 (1994).
- [70] The CMS collaboration, *Status Report and Milestones*, CERN/LHCC/94-20 (1994).
- [71] D. E. Groom, *Radiation levels in detectors at the SSC*, CERN 89-10 (1989) 103.
- [72] The ATLAS collaboration, *The ATLAS Inner Detector*, CERN/LHCC/93-24 (1993).
- [73] V. I. Klyukhin *et al.*, *Magnetic field integrals for the ATLAS tracking volume*, ATLAS INDET-NO-023.
- [74] H. Schönbacher (ed.), *Some safety aspects for LHC experiments*, LHCC/93-13, and references herein.
- [75] A. G. Clark *et al.*, *Electron identification using energy momentum matching in the ATLAS inner detector*, ATLAS INDET-NO-015.
- [76] D. Froidevaux *et al.*, *Electron identification in the ATLAS inner tracker*, ATLAS INDET-NO-017.
- [77] C. D'Ambrosio *et al.*, CERN-PPE/92-26, and CERN-PPE/92-69.
- [78] N. I. Bozhko *et al.*, Nucl. Instr. and Meth. A317 (1992) 97.
- [79] K. Bos and J. Schmitz, *Positions of the detectors in the ATLAS forward tracker*, ATLAS INDET-NO-019.
- [80] A. Poppleton *et al.*, *Momentum resolution of three tracker designs for Eagle*, Eagle INDET-NO-001.
- [81] Z. Kunszt and W. J. Stirling, *The Standard Model Higgs at LHC: branching ratios and cross-sections*, CERN 90-10 (II) 428 (1990).
- [82] L. Fayard and G. Unal, EAGLE note PHYS-NO-001, and addenda 1 and 2.
- [83] M. Della Negra *et al.*, *Search for  $H \rightarrow Z^* Z^* \rightarrow 4$  leptons at LHC*, CERN 90-10 (II) 509 (1990).
- [84] A. Nisati, *Search for  $pp \rightarrow H^0 \rightarrow Z^0 Z^0 \rightarrow \mu^+ \mu^- \mu^+ \mu^-$  at the LHC*, CERN 90-10 (II) 492 (1990).
- [85] H.-U. Bengtsson and T. Sjöstrand, Computer Physics Commun. 46 (1987) 43.
- [86] R. Kinnunen *et al.*, *Search for  $H \rightarrow ZZ^* \rightarrow 4$  leptons with the CMS detector at the LHC*, CMS TN/92-08.
- [87] R. St. Denis *et al.*, *Standalone muon performance for intermediate mass Higgs*, ATLAS PHYS-NO-011. D. Froidevaux *et al.*, *Update of results on intermediate mass Higgs*, ATLAS PHYS-NO-011 Add. 1.
- [88] J-C. Chollet *et al.*, *Electron isolation with ATLAS*, ATLAS PHYS-NO-017.
- [89] J-C. Chollet *et al.*, *Update on latest particle level simulations for  $H \rightarrow ZZ^* \rightarrow 4l$* , ATLAS PHYS-NO-019.

- [90] C. Guyot, *Intermediate mass Higgs search using impact parameter technique*, ATLAS PHYS-NO-023.
- [91] L. Fayard and L. Serin, *Implication of top decay models and b quark fragmentation on estimate of the  $t\bar{t}$  and  $Zb\bar{b}$  background to  $H \rightarrow 4$  leptons*, ATLAS PHYS-NO-024.
- [92] J. P. Guillet *et al.*, *Heavy quark production at the LHC*, CERN 90-10 (II) 116 (1990).
- [93] S. Bentvelsen, *Measurement of the proton structure function at HERA using the ZEUS detector*, thesis, University of Amsterdam 1994.
- [94] I. Gavrilenko, *Pattern recognition in TRD/Tracker (TRD/T)*, ATLAS INDET-NO-016.
- [95] C. Daum *et al.*, *Recommendation of the ATLAS magnet panel*, ATLAS GEN-NO-002.